QUANTIFICATION AND SIZING OF METAL-BASED NANOPARTICLES IN THE ENVIRONMENTAL AND BIOLOGICAL SAMPLES

Janja Vidmar

Doctoral Dissertation
Jožef Stefan International Postgraduate School
Ljubljana, Slovenia

Supervisor: Prof. Dr. Radmila Milačič, Jožef Stefan International Postgraduete School, Ljubljana, Slovenia
Co-Supervisor: Prof. Dr. Janez Ščančar, Jožef Stefan International Postgraduete School, Ljubljana, Slovenia

Evaluation Board:
Prof. Dr. Milena Horvat, Chair, Jožef Stefan International Postgraduete School, Ljubljana, Slovenia
Prof. Dr. Maja Čemažar, Member, Institute of Oncology Ljubljana, Ljubljana, Slovenia
Prof. Dr. Iztok Turel, Member, Faculty of chemistry and chemical technology, Ljubljana, Slovenia
Prof. Dr. Heidi Goenaga Infante, Member, LGC, Teddington, United Kingdom

MEDNARODNA PODIPLOMSKA ŠOLA JOŽEFA STEFANA
JOŽEF STEFAN INTERNATIONAL POSTGRADUATE SCHOOL



Janja Vidmar

QUANTIFICATION AND SIZING OF METAL-BASED NANOPARTICLES IN THE ENVIRONMENTAL AND BIOLOGICAL SAMPLES

Doctoral Dissertation

DOLOČANJE KONCENTRACIJE IN VELIKOSTI KOVINSKIH NANODELCEV V OKOLJSKIH IN BIOLOŠKIH VZORCIH

Doktorska disertacija

Supervisor: Prof. Dr. Radmila Milačič

Co-Supervisor: Prof. Dr. Janez Ščančar

Ljubljana, Slovenia, April 2017

Acknowledgments

The research for this doctoral thesis was performed at the Department of Environmental Sciences, Jožef Stefan Institute. First, I would like to thank my supervisor Prof. Dr. Radmila Milačič for her guidance, encouragement and big support during my doctoral studies. She gave me priceless advice that helped me enrich my scientific work. I also appreciate the assistance and scientific support of my co-supervisor Prof. Dr. Janez Ščančar.

Next, I want to express my gratitude to Primož Oprčkal and Assist. Prof. Dr. Ana Mladenovič from the Slovenian National Building and Civil Engineering Institute, who contributed significantly to my work related to following the behavior of iron nanoparticles after their use in nanoremediation.

A part of this work was realized thanks to Dr. Katrin Loeschner and Prof. Dr. Erik Larsen from the National Food Institute, Technical University of Denmark, and thanks to Dr. Tina Buerki from Swiss Federal Laboratories for Materials Science and Technology. They enabled me to be involved in the project investigating the translocation and accumulation of silver nanoparticles across the human placenta. I am especially grateful to Katrin who supervised my experimental work, and made my stay in Denmark very welcoming.

I would like to thank the Slovenian Research Agency for financially supporting my work through the Young Researchers programme. This work has also been supported by the EU-funded project Life+ RusaLCA, Grant Agreement LIFE12 ENV/SI/000443, the MASSTWIN project that has received funding from the European Union's Horizon 2020 research and innovation programme under grant agreement no. 692241 and by the European Communities 7th Framework Programme Funding under Grant agreement no. 603629-ENV-2013-6.2.1-Globaqua. Thanks also to the Adfutura funding that financed my research visit to Denmark.

I want to thank the members of the evaluation board: Prof. Dr. Milena Horvat, Prof. Dr. Heidi Goenaga Infante, Prof. Dr. Maja Čemažar and Prof. Dr. Iztok Turel for reviewing the manuscript and evaluating the work of my thesis.

I am also grateful to my co-workers Assist. Prof. Dr. Tea Zuliani, Dr. Kelly Peeters, Petra Novak, Ana Drinčić, Dr. Anže Martinčič and Dr. Breda Novotnik, who always helped me when I needed their advice and made my work at the Jožef Stefan Institute enjoyable. At the end I would like to give a big thanks to my family and friends who have supported me, always stood by my side and believed in me throughout all these years. Thank you for understanding me even when I did not find time for you.

Abstract

Nanoparticles (NPs), defined as natural, incidental or manufactured materials containing particles where 50 % or more of the particles in the number size distribution have one or more external dimensions in the size range 1 nm–100 nm, have been increasingly used in consumer products, health care technology and industrial applications, which has led to their release into the environmental and biological systems. Due to their specific properties, such as small size and high surface reactivity, NPs present new potential pollutants, since they are able to enter and accumulate in a living organism. So far, little is known about the occurrence, fate and potential toxicity of NPs in environmental and biological systems mostly due to the lack of sensitive, reliable and selective analytical methods. Recently, single particle inductively coupled plasma mass spectrometry (SP-ICP-MS) demonstrated the potential to become the method of choice for the characterization and quantification of metal-based NPs in complex matrices. Besides simultaneous quantification of particulate and/or dissolved forms of specific elements, it also provides quantitative information about number-based particle size distribution and mass/number concentration, at environmentally relevant concentration levels (ng/L).

In the presented doctoral dissertation, SP-ICP-MS technique was optimized and applied for sizing and quantitative determination of titanium dioxide nanoparticles (TiO_2NPs) and dissolved Ti in river water samples, achieving low limits of detection. For maintaining TiO_2NPs dispersed and stabilized in aqueous suspensions during the analytical procedure, different dispersion approaches, ultrasonication or ultrasonication in combination with dispersing agents, were examined. Results demonstrated that environmental conditions, such as the presence of natural organic matter and ionic strength, have a significant influence on the efficiency of dispersion and the stability of TiO_2NPs.

Next, SP-ICP-MS was optimized and used for sizing and quantification of zero-valent iron nanoparticles (nZVI) in order to follow their behaviour and fate after their use in nanoremediation. The influence of different iron loads and water matrices on the behaviour of nZVI, their interactions with Cd^{2+} and efficiency of Cd^{2+} removal was studied. The results showed that nanoremediation with the use of Fe loads 0.25 g/L or higher is efficient for the removal of Cd from wastewater and does not present an environmental nano threat.

Last but not least, SP-ICP-MS was used for studying translocation and accumulation of silver nanoparticles (AgNPs) with different surface coatings in human placenta. Since AgNPs are partially soluble, one objective of the study was to examine potential Ag precipitation and distinguish between the translocation and uptake of ionic and particulate Ag. The results suggest that particles detected on the fetal side could be the results of the AgNPs dissolution on the maternal side, translocation of Ag ions across the placenta and their precipitation on the fetal side. For detection of AgNPs in placental tissue by SP-ICP-MS, two sample preparation techniques were applied for releasing NPs from the tissue. We showed that the method using enzymatic tissue treatment followed by single particle ICP-MS is efficient for quantitative determination of mass concentration as well as size distribution of AgNPs in human placental tissues.

Povzetek

Nanodelci (NDs), definirani kot naravna, naključna ali proizvedena snov, ki vsebuje delce, kjer ima najmanj 50 % delcev glede na njihovo številčno velikostno porazdelitev eno ali več zunanjih dimenzij med 1 in 100 nm, se vse pogosteje uporabljajo v različnih medicinskih in industrijskih aplikacijah, zaradi česar se sproščajo v okolje ali pridejo v stik z živimi organizmi. Zaradi svojih specifičnih lastnosti, kot sta majhnost in velika reaktivnost, NDs predstavljajo novo potencialno onesnažilo, saj lahko vstopijo v žive organizme in se tam kopičijo. Raziskav na področju pojavnosti, usode in potencialne strupenosti NDs v okoljskih in bioloških sistemih je malo, saj zanje primanjkuje občutljivih, zanesljivih in selektivnih analiznih metod. Nov pristop, ki ima velik potencial pri detekciji in karakterizaciji kovinskih NDs v kompleksnih matricah z masno spektrometrijo z induktivno sklopljeno plazmo, je tehnika »single particle« (SP-ICP-MS). Ta metoda omogoča sočasno merjenje elementa v ionski obliki ter obliki nanodelcev, določanje velikostne porazdelitve na osnovi števila delcev in masne oziroma številčne koncentracije (meja zaznave je na koncentracijskem nivoju nekaj ng/L).

V predstavljenem doktorskem delu smo metodo SP-ICP-MS optimizirali in uporabili za določitev velikostne porazdelitve in masne koncentracije nanodelcev titanovega dioksida (TiO_2NDs) ter za določitev koncentracije topnega titana v vzorcu rečne vode. Za zagotavljanje stabilnosti disperzije TiO_2NDs v času analiznega postopka smo uporabili ultrazvok ali ultrazvok v kombinaciji z različnimi disperzijskimi sredstvi. Rezultati so pokazali, da imajo lastnosti matrice, kot so prisotnost naravne organske snovi ali ionske moči, velik vpliv na učinkovitost disperzije in stabilnost TiO_2NDs.

Optimizirano metodo SP-ICP-MS smo uporabili tudi za določitev velikostne porazdelitve in koncentracije nanodelcev ničvalentnega železa (nZVI), kar nam je omogočilo sledenje obnašanju nZVI v odpadni vodi po njihovi uporabi v nanoremediaciji. Proučevali smo vpliv različnih koncentracij dodanega železa in vodne matrice na usedanje nZVI, njihove interakcije s Cd^{2+} in učinkovitost odstranjevanja Cd^{2+} iz odpadne vode. Rezultati so pokazali, da je nanoremediacija z uporabo najmanj 0,25 g/L nZVI učinkovita za odstranitev Cd iz odpadnih vod, nanodelci, ki se hitro usedejo, pa ne predstavljajo nevarnosti za okolje.

Metodo SP-ICP-MS smo uporabili tudi za proučevanje prenosa in akumulacije srebrovih nanodelcev (AgNDs) z različnimi površinskimi lastnostmi v človeški placenti. Ker so AgNDs delno topni, je bil eden od ciljev raziskave preučiti morebitno obarjanje srebra in ugotoviti razlike med prenosom in akumulacijo ionskega srebra ter srebra v obliki nanodelcev. Rezultati kažejo, da so lahko AgNDs, ki smo jih pomerili na otrokovi strani placente, posledica raztapljanja AgNDs na materni strani placente, prenosa srebrovih ionov čez placento in njihovega obarjanja. Za določitev koncentracije in velikosti AgNDs v tkivu placente s pomočjo SP-ICP-MS smo uporabili in primerjali dve različni metodi za ekstrakcijo AgNDs iz tkiva. Pokazali smo, da je metoda encimske obdelave tkiva, ki ji sledi analiza s SP-ICP-MS, učinkovita za kvantitativno določitev masne koncentracije ter velikostne porazdelitve AgNDs v človeški placenti.

Contents

List of Figures **xv**

List of Tables **xix**

Abbreviations **xxi**

Symbols **xxiii**

1 Introduction **1**
1.1 Definition of Nanoparticles ... 1
1.2 Classes of Nanoparticles and Their Use ... 1
1.2.1 Natural NPs ... 1
1.2.2 Engineered NPs ... 2
1.2.2.1 Titanium dioxide nanoparticles ... 2
1.2.2.2 Zero-valent iron nanoparticles ... 2
1.2.2.2.1 Nanoremediation ... 2
1.2.2.3 Silver nanoparticles ... 3
1.3 Release, Behavior and Fate of ENPs in Environmental and Biological Systems . 4
1.3.1 Surface modification ... 6
1.3.2 Aggregation/agglomeration ... 6
1.3.3 Dissolution ... 7
1.4 Toxicity of Nanoparticles ... 7
1.4.1 Biological uptake of nanoparticles ... 7
1.4.2 Toxic effects of nanoparticles ... 8
1.4.2.1 Toxicity of TiO_2NPs ... 8
1.4.2.2 Toxicity of FeNPs ... 8
1.4.2.3 Toxicity of AgNPs ... 8
1.5 Methods for Quantification and Characterization of Metal-Based Nanoparticles in Environmental and Biological Samples ... 9
1.5.1 Sample preparation ... 10
1.5.1.1 Digestion ... 10
1.5.1.2 Filtration and centrifugation ... 11
1.5.1.3 Stabilization ... 11
1.5.2 Electron microscopy ... 12
1.5.3 Light scattering techniques ... 13
1.5.4 Atomic spectrometry techniques ... 13
1.5.4.1 ICP-MS ... 14
1.5.4.2 Single particle ICP-MS ... 14
1.5.4.2.1 Fundamentals ... 15
1.5.4.2.2 Determination of particle size ... 16
1.5.4.2.3 Determination of particle concentration ... 17

1.5.4.2.4 Determination of transport efficiency 17
1.5.4.2.5 Sample dilution 18
1.5.4.2.6 Dwell time 18
1.5.4.2.7 Instrumentation and data processing 19
1.5.4.2.8 SP-ICP-MS spectral interferences 19
1.5.4.2.9 Limitations of SP-ICP-MS 20
1.5.5 Separation techniques 20
1.5.5.1 Size-exclusion chromatography 20
1.5.5.2 Hydrodynamic chromatography 21
1.5.5.3 Field flow fractionation 21
1.5.5.4 Capillary electrophoresis 21

2 Aims and Hypothesis 23

3 Materials and Methods 25
3.1 Reagents and Materials 25
3.2 Instrumentation 27
3.3 Methods 28
3.3.1 Sample collection and sample preparation 28
3.3.2 Microwave-assisted digestion of TiO_2NPs 30
3.3.3 Enzymatic treatment of placental tissues containing AgNPs 31
3.3.4 Alkaline treatment of placental tissues containing AgNPs 31
3.3.5 Determination of total Ti concentrations by ICP-MS 31
3.3.6 Determination of total Ag concentrations in perfusates and placental tissues by ICP-MS 32
3.3.7 DLS measurements of AgNPs 33
3.3.8 SP-ICP-MS analyses 33
3.3.8.1 SP-ICP-MS analysis of TiO_2NPs 33
3.3.8.2 SP-ICP-MS analysis of nZVI 35
3.3.8.3 SP-ICP-MS analysis of AgNPs 36

4 Results and Discussion 39
4.1 Optimization of the Procedure for Efficient Dispersion of Titanium Dioxide Nanoparticles in Aqueous Samples 39
4.1.1 Determination of total Ti concentrations in TiO_2NPs by ICP-MS 39
4.1.2 Determination of total Ti concentrations in aqueous solutions of TiO_2NPs by ICP-MS 40
4.1.3 Stabilization of TiO_2NPs in aqueous solutions 41
4.1.4 Stability of TiO_2NPs in environmental water samples 44
4.2 Sizing and Simultaneous Quantification of Nanoscale Titanium Dioxide and a Dissolved Titanium Form by Single Particle Inductively Coupled Plasma Mass Spectrometry 46
4.2.1 Size and size distribution of TiO_2NPs determined by TEM and DLS 46
4.2.2 Determination of TiO_2NPs size and size distribution by SP-ICP-MS 47
4.2.2.1 Nanoparticle diameter limit of detection 49
4.2.3 Quantitative determination of Ti number concentration in anatase and rutile 50
4.2.3.1 Nanoparticle concentration limit of detection 50
4.2.4 Influence of dwell time on the determination of the number concentration and size distribution of TiO_2NPs 51
4.2.5 Simultaneous quantification of TiO_2NPs and dissolved Ti 52

4.2.6 Quantification and sizing of TiO_2NPs in river water samples 54
4.3 The Behavior of Zero-Valent Iron Nanoparticles and Their Interactions with Cd^{2+} in Wastewaters Investigated by Single Particle ICP-MS 57
4.3.1 Characterization of nZVI nanoparticles.....57
4.3.2 Optimization of Fe measurement by triple quadrupole ICP-MS.....58
4.3.3 Problems related to SP-ICP-MS sizing under changing chemical composition of nZVI.....60
4.3.4 The influence of sample matrix on the nZVI behavior during nanoremediation.....61
4.3.5 The influence of Fe load on the nZVI behavior during nanoremediation of effluent wastewater.....63
4.3.6 Investigation of Cd^{2+} interactions with nZVI and Cd^{2+} removal from contaminated waters 65
4.4 Single-Particle ICP-MS Characterization of Silver Nanoparticles Translocation in the *ex vivo* Human Placental Perfusion Model to Predict Potential Fetal Exposure 68
4.4.1 Characterization of AgNPs.....68
4.4.2 Stability of AgNPs in perfusion medium 69
4.4.3 AgCl precipitation in perfusion medium.....70
4.4.4 Translocation of AgNPs across the human placental barrier 71
4.4.5 Comparison of Ag translocation determined by SP-ICP-MS or conventional ICP-MS 75
4.4.6 Accumulation of AgNPs in the placental tissue 76
4.4.7 Comparison of translocation data with other studies.....78
4.5 Use of Alkaline or Enzymatic Sample Pre-treatment Prior to Characterization of Silver Nanoparticles in Human Tissue by Single Particle ICP-MS.....79
4.5.1 Investigation of potential matrix effects on calibration 79
4.5.2 Comparison of spike recoveries and AgNP size distributions after enzymatic and alkaline treatment of placenta tissues 81
4.5.3 Quantification and characterization of AgNPs accumulated in human placenta in the *ex vivo* human placental perfusion model 84

5 Conclusions **87**

References **89**

Bibliography **105**

Biography **108**

List of Figures

Figure 1.1: Pathways by which engineered NPs enter the environment and illustration of the dynamic transformations of pristine NPs in contact with components from environmental and biological systems (adopted from [26–28]).....5
Figure 1.2: Schematic presentation for the introduction of suspension of NPs and ions into ICP-MS system, their volatilization, atomization and ionization in the plasma and data processing by SP-ICP-MS (adopted from [150]). 15
Figure 4.1: The efficiency of a two-step microwave-assisted digestion of nanoscale anatase (A) and rutile (B) using a mixture of 4 mL nitric acid, 2 mL hydrofluoric acid and 1 mL hydrochloric acid (first step) and various amounts of 4 % boric acid (second step). Results represent the average ± STD of three replicates.....40
Figure 4.2: The efficiency of dispersion of nanoscale rutile in MilliQ water, using ultrasonication and different dispersing agents. Each bar represents one replicate, while error bars represent the STD of Ti measurement by ICP-MS. 42
Figure 4.3: Zeta potentials of nanoscale rutile in MilliQ water dispersed by ultrasonication (US) and the use of different dispersing agents as a function of pH. 43
Figure 4.4: Zeta potentials of river water (A) and wastewater (B), spiked with nanoscale anatase and rutile. Samples were dispersed by ultrasonication (US) and by the use of US in combination with different dispersing agents. Results represent the mean value of ten replicates with the STD of the measurements. 45
Figure 4.5: TEM images of TiO_2NPs in rutile and anatase crystalline phases, which were taken at magnifications of 25k (left-hand images) and 100k (right-hand images). 46
Figure 4.6: DLS hydrodynamic size measurements (intensity-based distributions) of TiO_2NPs in rutile and anatase crystalline phases. Results represent the average of three consecutive measurements corresponding to one stock suspension prepared by ultrasonication. 47
Figure 4.7: Data processing for the determination of the size distribution of TiO2NPs using SP-ICP-MS. Time scans for dissolved Ti (0.5 ng Ti/mL) (D-1), TiO_2NPs in rutile (0.2 ng Ti/mL) (R-1) and anatase (0.6 ng Ti/mL) (A-1); Corresponding signal distribution histograms for dissolved Ti (D-2), TiO_2NPs in rutile (R-2) and anatase (A-2); Calibration curve (dissolved Ti standards) created for particle size calculation (D-3); Calibration curve created for the calculation of the mass of an individual particle (D-4); Size distribution histograms for TiO_2NPs in rutile (R-3) and anatase (A-3). SP-ICP-MS measurements were performed at 10 ms dwell time (the schematic presentation is adapted from ref. [150], while the data are from the present work).....48
Figure 4.8: Ratio between the determined and expected Ti mass concentrations as a function of Ti mass concentration for anatase and rutile TiO_2NPs, measured by SP-ICP-MS at 10 ms dwell time. Results represent the mean value of three replicates with the STD of the measurements.....50
Figure 4.9: Ratio between the determined and expected Ti mass concentrations as a function of dwell time for two Ti mass concentrations (0.003 and 0.006 ng Ti/mL for anatase and 0.03 and 0.06 ng Ti/mL for rutile) of TiO_2NPs measured by SP-ICP-MS.

Results represent the mean value of three replicates with the STD of the measurements. 51
Figure 4.10: Time scans (A-1, B-1) and signal distribution histogram (A-2, B-2) for the mixture of 40 nm AgNPs and dissolved Ag and the mixture of TiO_2NPs and dissolved Ti, respectively. Measurements were performed by SP-ICP-MS at 3 ms dwell time for the AgNPs and 10 ms for the TiO_2NPs. Signals from the dissolved form of the element are fitted to a Poisson distribution, while signals from the particulate form of the element are fitted to a Gaussian distribution. 53
Figure 4.11: Time scans of river water sample (A), sample spiked with rutile (0.0256 ng Ti/mL) (B) and sample spiked with anatase (0.00113 ng Ti/mL) (C). SP-ICP-MS measurements were performed at 10 ms dwell time. 55
Figure 4.12: (A) FESEM picture, (B) SAED pattern, (C) TEM picture of fresh nZVI and powder X-ray diffraction pattern of (D1) fresh nZVI in MilliQ water and (D2) nZVI after 23 days of settling in the effluent wastewater. 57
Figure 4.13: ^{56}Fe signal intensity measured in MilliQ water (MQ), MQ spiked with 1 µg/L Fe (MQ + Fe), 50 µg/L Ca solution (Ca) and 50 µg/L Ca solution spiked with 1 µg/L Fe (Ca + Fe) applying different measurement modes. The signal-to-background (S/B) ratio of ^{56}Fe in MQ or 50 µg/L Ca solution is also presented. 59
Figure 4.14: Repeatability of the size distributions of nZVI dispersed in MilliQ water, determined in H_2 reaction mode by SP-ICP-MS (bin size 5 nm). Numbers in the legend show median diameters for the individual size distribution. 60
Figure 4.15: The influence of settling time on the nZVI mass concentration (A, fraction size > LOD_{size} and B, fraction size ≤ LOD_{size}), number concentration (C) and their size (D) in the water samples investigated. nZVI concentrations at different settling times were normalized to the initial nZVI concentration determined at time 0 h. Error bars represent STD between two measurements of the same sample. 62
Figure 4.16: The influence of settling time on the nZVI mass concentration (A, fraction size > LOD_{size} and B, fraction size ≤ LOD_{size}) and nZVI size (C) in effluent wastewater treated with different Fe loads. nZVI concentrations at different settling times were normalized to the initial nZVI concentration determined at time 0 h. Error bars represent STD between two measurements of the same sample. 64
Figure 4.17: Time scans for ^{111}Cd measured in single particle mode at settling time 0 h (A) and 18 h (B) in synthetic wastewater with the applied threshold between the background and particles signal. 65
Figure 4.18: The influence of settling time on the concentration of dissolved Cd^{2+} and Cd^{2+} attached to nZVI in MilliQ water (A), synthetic wastewater (B), and effluent wastewater (C) spiked with 100 µg Cd/L and treated with 0.25 g/L of nZVI. 66
Figure 4.19: The influence of settling time on the concentration of dissolved Cd^{2+} (A) and Cd^{2+} attached to nZVI (B) in effluent wastewater treated with different Fe loads. 67
Figure 4.20: TEM images of AgPEG and AgCOONa NPs. 68
Figure 4.21: DLS hydrodynamic size measurements (intensity-based distributions) of PM alone and AgPEG (left) and AgCOONa NPs (right), dispersed in UPW or PM (1 mg/mL). 69
Figure 4.22: Size distributions of AgCOONa (left) and AgPEG NPs (right), freshly prepared in UPW and PM, determined by SP-ICP-MS. 70
Figure 4.23: DLS hydrodynamic size measurements (intensity-based distributions) of PM and different concentrations of ionic Ag in PM (100 µg/mL, 10 µg/mL and 1 µg/mL). Samples were analyzed immediately after their preparation. 71
Figure 4.24: Perfusion profiles and transfer rates of Ag mass fraction >25nm (continuous line) and ≤ 25 nm (dashed line) during *ex vivo* human placental perfusion with AgPEG NPs, AgCOONa NPs and dissolved Ag, measured on the maternal (red colour) and fetal

side (green colour) over a time period of 6 h. Data represent the mean ± STD of the independent experiments (N=2 for AgPEG NPs, N=3 for AgCOONa NP) and the mean ± STD from analytical repetitions of one experiment (N=1 for dissolved Ag).....72
Figure 4.25: Effects of Ag NPs on BeWo cell viability. Cell viability of BeWo cells was assessed by MTS assay 6 and 24h after treatment with the indicated concentrations of NPs. $CdSO_4$ was used as a positive control. Optical density was measured at 490 nm and values are blank corrected as well as normalized to the untreated samples. Data represent mean ± SEM of 3 individual experiments.....72
Figure 4.26: Size distributions of NPs formed on the maternal side (red colour) and fetal side (green colour) in the perfusion experiments with AgPEG NPs, AgCOONa NPs and dissolved Ag.....74
Figure 4.27: Comparison of perfusion profiles and transfer rates of Ag during *ex vivo* human placental perfusion with AgPEG NPs and AgCOONa NPs, determined by SP-ICP-MS (dashed lines) and conventional ICP-MS (continuous lines). Presented are Ag concentrations measured on the maternal (red colour) and fetal side (green colour) of the placenta over a time period of 6 h. Data represent the mean ± STD of the independent experiments (N=2 (SP-ICP-MS) or N=3 (ICP-MS) for AgPEG NPs, N=3 (SP-ICP-MS) and N=2 (ICP-MS) for AgCOONa NPs).....76
Figure 4.28: Mass concentration of Ag fraction > and ≤ 25 nm, determined by SP-ICP-MS in enzymatically treated tissue samples, from perfusion with AgPEG NPs, AgCOONa NPs and $AgNO_3$. Ag mass concentrations in placenta collected after 6 h of perfusion are normalized to the applied Ag concentration measured in M0 samples by conventional ICP-MS. Data represent the mean ± STD of the independent experiments (N=2 for AgPEG NPs, N=2 for AgCOONa NPs, N=1 for $AgNO_3$).....77
Figure 4.29: Comparison of size distributions of AgPEG and AgCOONa NPs, determined by SP-ICP-MS in the samples on maternal, fetal side and in placenta tissue after 6 h of perfusion.....78
Figure 4.30: Particle size distribution (bin size 2 nm) obtained by spICPMS for AgPEG40 NPs suspended in UPW and AgPEG40 NPs spiked to 1 % TMAH or enzyme solution.....80
Figure 4.31: Particle size distribution (bin size 2 nm) obtained by spICPMS for AgPEG NPs in placental tissue after enzymatic (left; red histogram) or alkaline treatment (right; green histogram). The particle size distribution for AgPEG NPs in UPW is presented for comparison (blue histograms).....81
Figure 4.32: Particle size distribution (bin size 2 nm) obtained by spICPMS for AgCOONa NPs in placental tissue after enzymatic (left; red histogram) or alkaline treatment (right; green histogram). The particle size distribution for AgPEG NPs in UPW is presented for comparison (blue histograms).....82
Figure 4.33: Particle size distribution (bin size 2 nm) obtained by spICPMS for AgPEG NPs and AgCOONa NPs in spiked placental tissue (green histogram) and placental tissue in which AgNPs accumulated after 6 h of perfusion (red histogram). All placental tissues were enzymatically treated.....84

List of Tables

Table 1.1: Classification of commonly used engineered NPs and their applications (adopted from [3, 6, 23]). 4
Table 1.2: Analytical techniques suitable for analysis of NPs in complex matrices (adopted from [28, 102, 121, 126])....12
Table 3.1: ICP-MS operating parameters for determination of total Ti concentrations. ..32
Table 3.2: ICP-MS operating parameters for the determination of total Ag mass concentration in the perfusates and tissues.....33
Table 3.3: ICP-MS operating parameters for quantification and sizing of TiO_2NPs and AgNPs by SP-ICP-MS. 34
Table 3.4: ICP-MS instrumental parameters for single particle analysis of nZVI.....35
Table 3.5: ICP-MS settings for single particle analysis of AgNPs. 37
Table 4.1: Recoveries between the determined and expected Ti concentrations in nanoscale anatase and rutile samples after two step microwave assisted digestion. A mixture of 4 mL HNO_3, 2 mL HF and 1 mL HCl in first step and 6 mL of 4 % boric acid in second step were added to (A) 10 mg of sample and (B) 10 mg of sample + 20 mL of water. Concentration of Ti was determined by ICP-MS immediately after the digestion. 41
Table 4.2: Selected parameters for river and wastewater samples. 44
Table 4.3: Determination of Ti concentration in river and wastewater samples and the recoveries between the determined and expected Ti concentrations in water samples spiked with TiO_2NPs (anatase and rutile) after two step microwave assisted digestion. Results represent the mean value of three replicates ± STD of measurements. 44
Table 4.4: Recoveries between determined and expected mass concentrations for the simultaneous determination of the Ti mass concentration in TiO_2NPs and dissolved Ti by SP-ICP-MS. Results represent the mean value of three replicates with the STD of the measurements. 54
Table 4.5: Simultaneous determination of the mass concentration of dissolved Ti and TiNPs in a river water sample by SP-ICP-MS and recoveries between the determined and expected mass concentrations in a sample spiked with TiO_2NPs (anatase and rutile). Results represent the mean value of three replicates with the STD of the measurements. 56
Table 4.6: Sensitivity, limits of detection (LOD) and accuracy check for the determination of Fe by QQQ ICP-MS using different collision–reaction cell conditions. For the accuracy check, SPS-SW1 surface and SPS-WW1 waste water quality control materials were used. Spike recovery test was also performed in 50 µg/L Ca solution and effluent wastewater. 60
Table 4.7: Summary of AgNP characteristics. Results for Ag mass concentration (N=3), dissolved Ag fraction (N=2) and zeta potential (N=5) represent mean ± STD.....68
Table 4.8: Mass concentrations of AgNPs > 25 nm and ≤ 25 nm and median NPs diameter, determined by SP-ICP-MS, for suspensions of AgPEG and AgCOONa NPs in UPW and PM. Results present mean values ± STD from two replicates.. 70

Table 4.9: Comparison of the transport efficiencies (calculated with particle frequency and particle size method by diluting AuNPs and ionic Au standards in relevant matrices, respectively) and ICP-MS responses for ionic Ag and ionic Au standards with related R^2 values prepared in relevant matrices. Results, which represent the values measured on the same day, were comparable to a second measurement on another day. 79
Table 4.10: Ag mass concentration of NPs and background and median size for AgPEG40 NPs prepared in UPW and matrices relevant to each treatment type at a mass concentration of 20 ng/L (N=2). Transport efficiency (with the use of the "particle size method") and ICP-MS response were determined in UPW. 80
Table 4.11: Ag mass recovery, mass fraction of AgNPs > 25 nm and median particle size for AgPEG and AgCOONa in UPW (N=4) and in placental tissue after enzymatic and alkaline treatment (N=2) (mean ± STD).. 82
Table 4.12: Ag mass concentration, median particle size and the number of particles, detected by SP-ICP-MS analysis, for the enzymatically or alkaline treated control tissue samples, 1 % TMAH and enzymatic solution, spiked with 1 mg/L of ionic Ag (20,000 times diluted before analysis to 50 ng/L). Results represent the average value with the STD between two replicates. 83
Table 4.13: Comparison of Ag concentrations (in nanograms of Ag per gram of placental tissue) in placental tissues collected after 6 h of perfusion, obtained by SP-ICP-MS after enzymatic treatment and by conventional ICP-MS after digestion with acids. The given values represent the mean ± STD of two determinations for each sample. Presented are also p-values (t-test, $p < 0.01$) for comparison of Ag concentrations between two treatments.. 85

Abbreviations

AFM	atomic force microscopy
AgPEG40 NPs	AgPEG NPs with 40 nm size
ANOVA	analysis of variance
ATP	adenosine triphosphate
bcc	body centred cubic cell
CE	capillary electrophoresis
CE	cellulose
CRM	certified reference material
Darvan C	ammonium polymethacrylate
DLS	dynamic light scattering
DNA	deoxyribonucleic acid
DTU	Technical University of Denmark
EDX	energy-dispersive X-ray
EMPA	Swiss Federal Laboratories for Materials Science and Technology
ENP	engineered nanoparticle
ESEM	environmental scanning electron microscopy
ET-AAS	electrothermal atomic absorption
EU	European Union
FESEM	field emission scanning electron microscopy
FFF	field-flow fractionation
FW	framework
HDC	hydrodynamic chromatography
HepG2	human hepatoma cells
ICP-MS	inductively coupled plasma mass spectrometry
ICP-OES	inductively coupled plasma optical emission spectrometry
IEP	isoelectric point
ISO	International Organization for Standardization
KED	kinetic energy discrimination
LA	laser ablation
LOD	limits of detection
LOD_{NP}	limit of detection for NPs mass concentration
LOD_{size}	size detection limit
LOQ	limit of quantification
M199	tissue culture medium
Macerozyme R-10	a mixture of pectinase, cellulase and hemicellulase
MilliQ	ultrapure water
NIST	National Institute of Standards and Technology
NM	nanomaterial
NOM	natural organic matter
NP	nanoparticle

NTA	nanoparticle tracking analysis
OECD	Organization for Economic Co-operation and Development
PAH	polycyclic aromatic hydrocarbons
PCC	particle collision coulometry
PDI	polydispersity index
PEI 600	polyethyleneimine
PFA	perfluoroalkoxy
PM	perfusion medium
PVP	polyvinylpyrrolidone
QQQ ICP-MS	triple quadrupole ICP-MS
R	sensitivity
RF	radio frequency
RIKILIT	research institute at the Wageningen University & Research Centre in the Netherlands
RM	reference material
ROS	reactive oxygen species
RSTD	relative standard deviation
SBWTP	small biological wastewater treatment plant
SCENIHR	Scientific Committee on Emerging and Newly Identified Health Risks
SDS	sodium dodecyl sulphate
SEC	size-exclusion chromatography
SP-ICP-MS	single particle ICP-MS
SPS-SW1	surface water reference materials
SPS-WW1	wastewater reference materials
STD	standard deviation
STM	scanning tunnel microscopy
TEM	transmission electron microscopy
TMAH	tetramethylammonium hydroxide
TOC	total organic carbon
TRA	time-resolved-analysis
Triton X-100	non-ionic surfactant
UPW	ultrapure water
US	ultrasonication
UV/Vis	ultraviolet/visible
WHO	World Health Organization
XAS	X-ray absorption spectroscopy
XPS	X-ray photoelectron spectroscopy
XRD	X-ray powder diffraction
σ_{MQ}	standard deviation of the blank

Symbols

AgCl	.....	silver chloride
AgCOONa NPs	.....	AgNPs thiolated with sodium 11-mercaptoundecanoate ($(CH_2)_{10}$ SH-COONa)
AgNPs	.....	silver nanoparticles
AgPEG NPs	.....	AgNPs thiolated with polyethylene glycol with a molecular weight of 550 g/mol (PEG_{550})
Al_2O_3NPs	.....	aluminium oxide nanoparticles
Ar	.....	argon
AuNPs	.....	gold nanoparticles
C	.....	mass concentration of dissolved standard
Cd^{2+}	.....	cadmium ion
CeO_2NPs	.....	cerium dioxide nanoparticles
C_p	.....	number concentration of particles
d	.....	particle diameter
f_a	.....	mass fraction of metal in the nanoparticle
Fe°	.....	zero-valent iron
Fe^{2+}, Fe^{3+}	.....	iron ions
Fe_2O_3NPs	.....	iron oxides nanoparticles
H^+	.....	hydrogen ion
H_2	.....	molecular hydrogen
H_2SO_4	.....	sulfuric acid
H_3BO_3	.....	boric acid
H_3PO_4	.....	phosphoric acid
HCl	.....	hydrochloric acid
He	.....	helium
HF	.....	hydrofluoric acid
HNO_3	.....	nitric acid
I_{bkg}	.....	average signal intensity of the background
I_p	.....	signal intensity of a particle
$K_2S_2O_7$	.....	potassium disulphate
$KHSO_4$	.....	potassium bisulphate
m	.....	slope of the mass flux calibration curve
m_p	.....	mass of a particle
Na_2CO_3	.....	sodium carbonate
$(NH_4)_2S_2O_8$	.....	ammonium peroxo disulphate
$(NH_4)_2SO_4$	.....	ammonium sulphate
n_p	.....	number of events
nZVI	.....	zero-valent iron nanoparticles
OH^-	.....	hydroxide
PtNPs	.....	platinum nanoparticles
q_{liq}	.....	sample introduction flow rate

SiO_2NPs	.....	silica nanoparticles
TiO_2NPs	.....	titanium dioxide nanoparticles
t_d	.....	acquisition time
W	.....	mass flux
ZnONPs	.....	zinc oxide nanoparticles
σ	.....	standard deviation of the continuous background
α-Fe_2O_3	.....	hematite
α-FeOOH	.....	goethite
η_i	.....	ionisation efficiency
η_{neb}	.....	transport (nebulization) efficiency
ρ	.....	density

Chapter 1

Introduction

1.1 Definition of Nanoparticles

The recent advances in nanotechnology and the corresponding increase in production and use of nanomaterials (NMs) in a variety of products have resulted in an extensive release of NMs into the environment, which consequently has significant impact on ecosystems. Scientific Committee on Emerging and Newly Identified Health Risks (SCENIHR) defines nanomaterial as a material with one or more dimensions under 100 nm. Within this group, nanoparticles (NPs) are defined as materials with three dimensions between 1 and 100 nm [1]. More recently, a definition of a nanomaterial recommended by the European Commission [2] states that "nanomaterial means a natural, incidental or manufactured material containing particles, in an unbound state or as an aggregate or as an agglomerate and where, for 50 % or more of the particles in the number size distribution, one or more external dimensions is in the size range 1 nm–100 nm". NPs unique size-dependent physicochemical, mechanical, catalytic, optical and electrical properties are often the reason for their increased use in consumer products. Their small size leads into a large surface area, which increases their chemical reactivity, so they could act as carriers for other contaminants, whereas a small size enables NPs to cross cell membranes. However, these same unique properties have prompted concern that NPs could be toxic to organisms by interacting with living systems and potentially disrupting vital processes [3].

1.2 Classes of Nanoparticles and Their Use

NPs can occur naturally in the environment and are assumed to be produced from different geological and biological processes, e.g. volcanic eruptions and forest fires [4]. Engineered NPs (ENPs), on the other hand, are the result of anthropogenic sources and originate from industrial and combustion processes and as a result of emerging nanotechnology. ENPs are usually monodispersed and homogenous regularly shaped particulates, synthesized by controlled chemical and physical processes and composed of a much wider variety of materials stabilized with surface coatings, while naturally occurring NMs are typically polydispersed, heterogeneous with irregular shape and complex structures [5]. Even though the natural NPs are present in the environment for billions of years they often lose their nano-sized properties by dissolution or aggregation, hence ENPs prevail in the environment due to their stabilization by capping or fixing agents [4, 6].

1.2.1 Natural NPs

Naturally occurring NPs in water, air and soil have existed from the beginning of Earth's history. Based on their chemical composition natural NPs can be separated into organic

(carbon-containing) and inorganic NPs. Organic nano-sized compounds include biological molecules, e.g. protein, nucleic acids, adenosine triphosphate (ATP), viruses, which are released into the environment directly from the organisms. Degradation of biological matters also produces NPs, e.g. humic and fulvic acids [6]. On the other hand, natural inorganic NPs include hydrous iron and manganese oxides in waters and clays, organic matter, iron oxides and other minerals in soils. The latter play an important role in the transportation of contaminants, sorbed to or incorporated into colloids [4].

1.2.2 Engineered NPs

ENPs are the main focus of the current research on NPs in the environment and in biological systems. The ENPs can be classified, regarding their chemical composition, in three major groups (Table 1.1):

- inorganic materials (such as metal NPs and quantum dots),
- organic NMs (such as carbon-based materials) and
- mixed organic-inorganic NMs (e.g. gold NPs functionalized with cyclodextrines).

One of the most widely used class of ENPs are metal-based NPs which consist of metal oxides with a variety of applications, including NPs based on cerium dioxide NPs (CeO_2), titanium dioxide (TiO_2), zinc oxide (ZnO), iron oxides (Fe_2O_3), aluminium oxide (Al_2O_3) and silica (SiO_2). The second class of nanomaterials, composed of metal-containing materials, are zero-valent NPs, such as zero-valent iron nanoparticles (nZVI), silver NPs (AgNPs) and gold NPs (AuNPs).

Beside metal-based NPs, ENPs include also carbon NPs (e.g. fullerene compounds, nanotubes, nanowires), nanopolymers, called dendrimers, and semi-conductor materials known as quantum dots [6]. The most commonly used ENPs, i.e., TiO_2NPs, nZVI and AgNPs that can potential end up in the environment or come into contact with living organisms, are further presented in detail.

1.2.2.1 Titanium dioxide nanoparticles

TiO_2NPs are the second most common metal-based NPs [7] and are used in a wide range of applications. As a white pigment, they are added to foodstuffs, paints and coatings and are, due to their UV light resistant properties, used in photocatalytic sensors, pharmaceuticals and cosmetics, e.g., toothpaste and sunscreens [8]. TiO_2NPs are generally synthesized in different crystalline phases (e.g. anatase, rutile) which possess unique properties. Anatase phase is used in antimicrobial applications for air and water purification and in sunscreens due to the highest photocatalytic activity, while rutile is a common white pigment additive in cosmetics, pharmaceuticals, paintings and food [9].

1.2.2.2 Zero-valent iron nanoparticles

The most common application of zero-valent iron nanoparticles (nZVI) is their use in nanoremediation of waters, sediments and soils where sorptive and reductive properties of iron and its mineral products remove or stabilise inorganic, organic and radioactive contaminants [10].

1.2.2.2.1 Nanoremediation As a result of industrial and urban activities, elevated concentrations of toxic elements are released to the surface and ground waters, affecting the health of living organisms. One of the common pollutants released into the environment due to the combustion of fossil fuels, metal production, application of phosphate fertilizers, electroplating, and the manufacturing of batteries, pigments, and screens, is cadmium (Cd) [11]. Cd^{2+} is extremely toxic and classified as a human carcinogen [12], causing damage to the lungs, kidneys, liver, and reproductive organs [13]. The World Health Organization

(WHO) has set a maximum guideline concentration of 3 µg L^{-1} for Cd^{2+} in drinking water [14].

Supplying of clean and affordable water for growing human population is becoming a major global challenge. To assure the water of adequate quality for humans and its sustainable use, it is necessary to clean and reuse contaminated waters. Among innovative technologies, nanoremediation with the use of nZVI has been investigated as one of the most efficient tools for the treatment of contaminated ground water, wastewater, soil and sediment [15]. nZVI can efficiently remove pollutants due to their small particle size, large surface area, and high density of reactive and adsorptive sites available for adsorption of contaminants [16]. During the nanoremediation process, oxidation of nZVI (from Fe° to Fe^{2+} and Fe^{3+}) and formation of Fe oxides and hydroxides occur. As a result, elements are removed due to their reduction and/or adsorption and co-precipitation with the Fe corrosion products [17].

After the treatment of wastewater with nZVI, NPs which are involved in biological, physical and chemical processes undergo several transformations. The behavior of nZVI depends on their properties, iron load and sample matrix (pH, ionic strength, organic matter and biochemical oxygen demand) [18]. After their oxidation, nZVI lose their nano characteristics and tend to rapidly aggregate and settle down [19]. However, some of NPs can still remain dispersed in the water, representing a potential nano threat. Despite extensive use of nZVI in the wastewater remediation, their fate and impact on the ecosystems remain poorly understood [20, 21]. In order to use nanoremediation in a responsible and environmentally acceptable way, the concentration, size and aggregation of nZVI after nanoremediation have to be followed.

1.2.2.3 Silver nanoparticles

Silver nanoparticles (AgNPs) are due to their antibacterial properties one of the most widely used engineered NPs, found in many commercial and medical products (e.g. food packaging, textile, laundry detergents, prosthetic devices, dietary supplements, cosmetics etc.) [22].

Table 1.1: Classification of commonly used engineered NPs and their applications (adopted from [3, 6, 23]).

CLASS OF ENPs	APPLICATIONS
Metals	
Ag	antimicrobials (wound dressings, socks, and other textiles, air filters, toothpastes, baby-products, vacuum cleaners, and washing machines), paint, coatings, medical uses, food packaging
Al	metallic and optical coatings, plating, cosmetic filter
Au	nanomedicine (vectors in tumour therapy), electronics (catalyst, flexible conducting inks or films)
Ca	health supplements
Cu	microelectronics
Fe	remediation of water, sediments, and soils
Mg	health supplements
Pt	catalysis
Se	health supplements
Sn	paints
Metal oxides	
TiO_2	cosmetics, sunscreen lotions, solar cells, paints and coatings, bioremediation, removal of various organics, air purification, semiconductors
ZnO	cosmetics, paint pigments, coatings, flame retardants, dental cements
CeO_2	fuel catalyst, gas sensors, solar cells, oxygen pumps, metallurgical and glass/ceramic applications, sintering additives, UV absorbent, alloy coating
Al_2O_3	usually substrate-bound, paint
Fe_2O_3	environmental remediation, biomedical applications, semiconductors, sensors for microbial detection
SiO_2	paints, coating, building composites
Carbon	
Nanotubes	metals sorption from contaminated sites, water purification systems, electronics and computers, plastics, catalysts, battery, fuel cell electrodes, supercapacitors, orthopedic implants, conductive coatings, adhesives and composites, sensors, components in the electronics, aircrafts, aerospace, automotive industries, sporting goods
Fullerenes	cosmetics, sorption of organic compounds (e.g. naphthalene), removal of organometallic compounds, nanomedicine (selective reactivity for antiviral activity)
Nanowires	for early detection of cancerous tumour
Polymers	
Dendrimers	manufacture of macrocapsules, nanolatex, coloured glasses, chemical sensors, modified electrodes, DNA transfecting agents, therapeutic agents, drug delivery and DNA chips, tumour treatment (used as a powerful anticancer drug)
Quantum dots	
CdSe/CdS/ZnS	medicine (medical imaging and targeted therapeutics), solar cells, photovoltaic cells, security inks, photonics and telecommunications

1.3 Release, Behavior and Fate of ENPs in Environmental and Biological Systems

Release of NPs into the environment may originate from point sources such as production facilities, landfills or wastewater treatment plants or from nonpoint sources such as wear from materials containing NPs or from sources of natural NPs (Figure 1.1). Besides natural and anthropogenic origin of NPs, ENPs can be released into the environment intentionally as well as unintentionally, such as atmospheric emissions and solid or liquid waste streams during production or from spillages associated with the transportation of manufactured NPs from production facilities to other manufacturing sites. Intentional release of NPs includes their use to remediate contaminated soils and groundwater [24]. Several routine human activities, e.g. urban air pollution, also significantly release the NPs as aerosols in the atmosphere. There they act as precursors for the formation of larger particles, which are known to strongly influence global climate, atmospheric chemistry, the visibility and regional and global transport of pollutants [25].

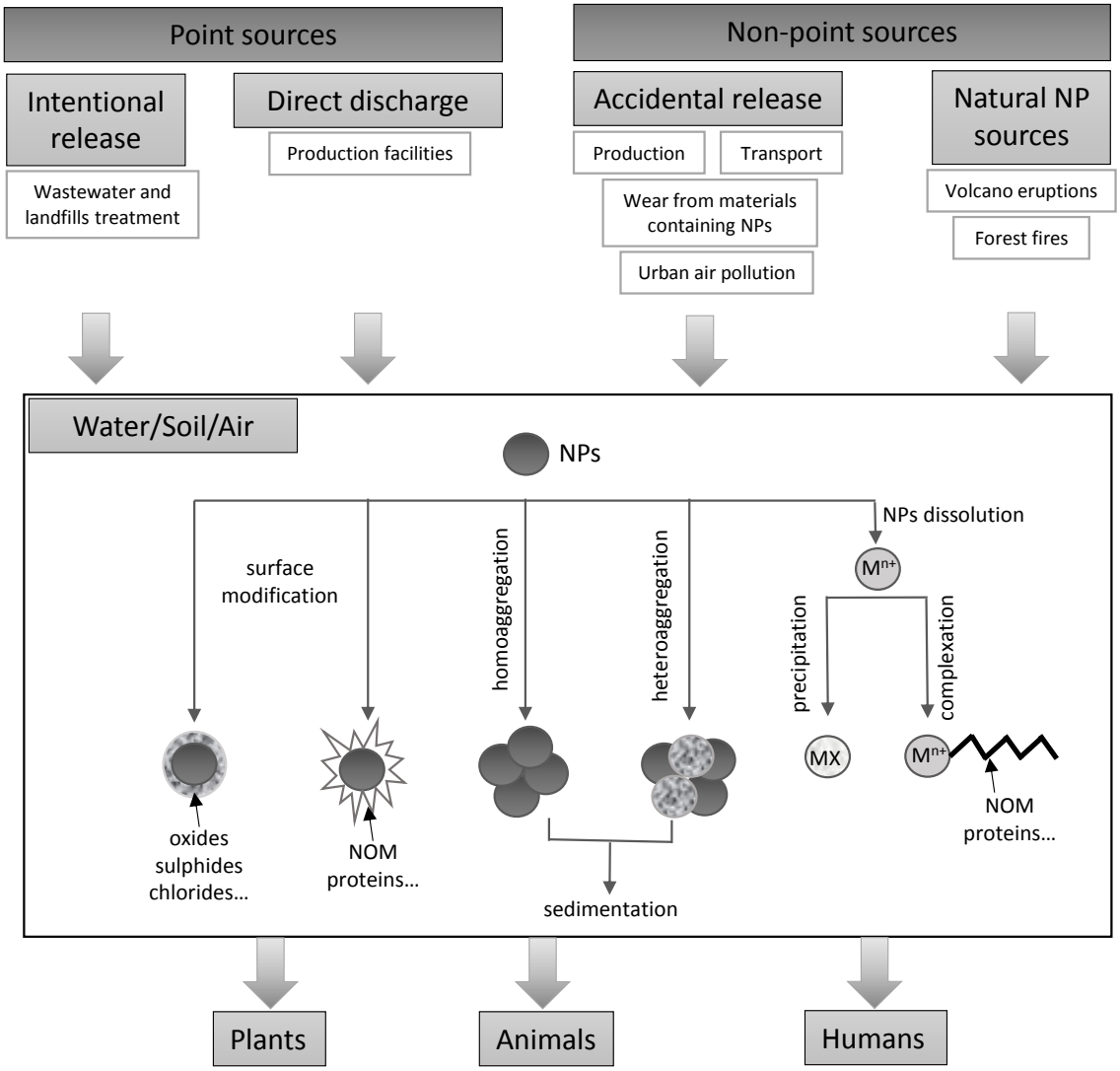


Figure 1.1: Pathways by which engineered NPs enter the environment and illustration of the dynamic transformations of pristine NPs in contact with components from environmental and biological systems (adopted from [26–28]).

Particles, released into the environment whether via sewage treatment plants, direct discharges, or accidental spillages, can contaminate soil, migrate into surface and ground waters, and interact with biota. Humans can be directly influenced by NPs through exposure to air, soil or water or indirectly by consuming plants or animals which have accumulated NP [27]. Although NPs are widely used, not much is known about their behaviour and fate in the environmental and biological systems. Once released into the environment, the mobility, bioavailability and toxicity of NPs in any ecosystem are affected by surrounding environmental conditions as well as by chemical and physical properties of NPs (e.g. chemical composition, particle mass and number concentration, size distribution (i.e., polydispersity of particles and the nature of their aggregates), specific surface area, surface charge or zeta potential, stability and solubility) [29]. NPs are not necessarily released as single NPs but can be embedded in a matrix, therefore release of NPs will occur through release of matrix-bound NPs. Released NPs can also be chemically or biologically modified or degraded under different environmental conditions such as light, the presence of oxidants or microorganisms.

1.3.1 Surface modification

One of the most common transformations of NPs released in the environmental or biological system is the modification of their surface properties. The surface properties of NPs govern their stability and mobility as colloidal suspensions or their aggregation into larger particles and deposition in environmental and biological systems. Surface properties that strongly depend on the composition of different surface coatings as well as on the zeta potential, which is the function of NPs surface charge, pH and ionic strength of the matrix, determine the conditions under which NPs remain in dispersed state [30, 31]. Metallic ENPs are usually coated with inorganic or organic compounds [6], such as citrate, cysteine, carbonate or surfactants, such as sodium dodecyl sulphate, to maintain the stability of the colloidal suspension [32].

Charge is another important property that influences stability or reactivity of NPs. NPs can become charged either by functionalization with various types of groups, such as COOH, NH_2, and SH_2 or by the change of pH. In acidic conditions the excess of H^+ ions normally results in a positively charged particle surface whereas the excess of OH^- yields a negatively charged surface [33]. For instance, NPs with negative zeta potential will repel each other, enhancing their stability in the solution [34]. With manipulating the zeta potential during sample processing we can therefore maintain conditions under which single NPs or aggregates exist. Moreover, increasing ionic strength reduces the size of the electrostatic double layer and repulsive force [33].

Dispersed NPs maintain their reactivity and catalytic behaviour and because of their large surface area they can easily interact with various components, e.g. metals, natural organic matter (NOM), proteins etc., affecting NP behaviour. Beside humic and fulvic acids, NOM also include rigid biopolymers, such as polysaccharides and peptidoglycans, and flexible biopolymers. These organic compounds can be sorbed onto the surfaces of ENPs by various types of interactions (electrostatic, hydrogen bonding and hydrophobic). In the presence of high-molecular mass NOM compounds, ENPs tend to aggregate, whereas, low-molecular mass NOM compounds increase the mobility of ENPs in the colloidal solution [6, 29, 35, 36]. Furthermore, the presence of NOM contributes to the NPs instability at high ionic strength in divalent metallic cation solutions, most likely due to intermolecular bridging with the organic matter [36].

Oxidation, sulfidation or degradation of particle coating by sunlight is another surface modification [33].

1.3.2 Aggregation/agglomeration

In the environment NPs can interact among themselves, forming homo-aggregates/agglomerates, and with other natural NPs or larger particles, forming hetero-aggregates/agglomerates (Figure 1.1). While agglomeration is based on weakly bound particles through e.g. weak Van der Wall's forces, aggregation presents strongly bound or fused particles [2]. Macromolecules or other particles such as clays or biocolloids in heteroaggregates can coat NPs, leading to steric effects [33]. Agglomeration and/or aggregation can generally lead to the formation of aggregates/agglomerates that are large enough to be settled down by gravitational force. This leads to the loss of their reactivity [6] and increase of their concentration in the sediment [37]. Aggregation and settling of NPs that can bind metals enables their transfer from the water column to the sediments, which can be exploited in purification of the water, contaminated with metallic pollutants.

Sedimentation of NPs can also be affected by different environmental conditions such as pH, ionic strength and NOM content. NOM generally stabilize NPs against aggregation and sedimentation, whereas water samples with high ionic strength show faster

sedimentation due to the increased aggregation [37]. In addition, particle size has an impact on agglomeration as well, where smaller particles agglomerate at slower rates [34].

1.3.3 Dissolution

Another possible modification of NPs is their dissolution which depends mainly on their chemical composition and size. Carbon NPs for instance are considered to be insoluble in water, while metal oxide NPs show greater solubility. It is assumed that smaller size of NPs, hence greater surface area, leads to increased dissolution. Moreover, dissolution rate depends on sample matrix like pH and NOM content [37]. Dissolved metals formed from dissolution of readily soluble NPs (e.g. AgNPs) can bind with anions (e.g. chlorides, sulphides) or other components (e.g. NOM, proteins) present in the matrix, forming precipitates or complexes, respectively [36].

1.4 Toxicity of Nanoparticles

Although exposure of humans and other living beings to NPs is significant and increasing, there is still little known about the toxicological properties of NPs and their impact on human health. Toxicity of NPs in biological systems is largely caused by the particle small size, shape, high reactivity, composition and surface properties, with smaller particles being more toxic.

1.4.1 Biological uptake of nanoparticles

The probable mechanisms of uptake and accumulation of ENPs by living organisms are not well known so far [6]. The routes of exposure of NPs to different organisms depend on their habitat. Terrestrial plants due to their large size and high leaf area frequently interact with ENPs directly with the soil, water, and atmospheric environmental compartments. Airborne ENPs get attached to the leaves and reach into the leaf tissue through cuts or wounds present on the leaf surface. Root parts of the plant also interact with water or soil-borne ENPs [6] that are intentionally applied for remediation purposes or are present in wastewater sludge used to enrich agriculture fields or are introduced into groundwater by leaching from landfills [38]. For fish in water or worms in soil, NPs can enter into the animal through gills or mouth, from where they are transported to the gut [39]. A human can be exposed to NPs through inhalation, ingestion, skin penetration or injections. They may come into contact with e.g. AgNPs either accidentally (e.g. through exposure from drinking contaminated water, inhalation or direct skin or organ contact) or intentionally (in the case of potential nanomedical applications) [40]. Once in the blood stream, NPs can be transported around the body through interactions with biological components such as proteins and cells from where they can be distributed into various organs and tissues, including brain, heart, liver, kidneys and the nervous system [40]. This raises concerns about NP accumulation, long-term retention in an organism and subsequent adverse health effects.

NPs can enter cells by diffusing through cell membranes, through endocytosis and adhesion (i.e. attachment to the plasma membrane). Animal cell walls are semi permeable, allowing the passage of small molecules while limiting the larger ones. Thus, only ENPs and their aggregates with a size smaller than that of the largest pore are expected to pass through the cell wall and reach the plasma membrane. It has been suggested that the interaction of ENPs with cells might induce the formation of new and bigger pores and therefore increase the entry of ENPs through the cell wall [29]. However, as opposed to

animals, most cell walls of plants, algae, and fungi act as a barrier for the entry of ENPs [6].

1.4.2 Toxic effects of nanoparticles

As soon as the ENPs enter the cell, they can bind with different types of organelles and interfere with the metabolic processes. The small particle size, a large surface area and the ability to generate reactive oxygen species (ROS) play a major role in toxicity of NPs. ROS in high levels cause oxidative stress and damage cells [39]. For instance, breaks of DNA strand, cross-linking, and adducts of the bases or sugars as well as structural damage to mitochondria caused by ROS formation can even the result in cell death [42]. Moreover, NPs might provoke alterations of the membrane structure and porosity, which results in the increase of its permeability [6]. Other possible toxicity mechanisms of NPs include destabilization of proteins, interruption of energy transduction and release of toxic components such as heavy metals or ions from NP solubilisation [4, 6].

There have been several reports on toxicity of mostly natural occurring NPs on human health. Several respiratory and cardiovascular diseases in humans are caused by nano-based black carbon that migrates deep into the lungs and carries very toxic, often carcinogenic compounds such as polycyclic aromatic hydrocarbons (PAH) [44–46].

1.4.2.1 Toxicity of TiO_2NPs

Adverse effects of NPs on algae, plants, animals and fungi, influencing photosynthetic or respiratory processes, have been found [4, 47]. For instance, a number of studies have been published concerning the potential ecotoxicological risks of TiO_2NPs to aquatic organisms, such as green algae [48], *Daphnia magna* [49, 50], *Artemia salina* [51] and marine phytoplankton [52]. Their toxic effects especially towards algae, higher plants, aquatic and terrestrial invertebrates and freshwater fish [9] induce gill injury, oxidative stress, and other physiological effects [53] or even enhance the uptake and toxicity of other pollutants [54]. Their toxic effects in biological systems largely depend on concentration, surface properties and size [55], as well as on the crystallinity of TiO_2NPs [56, 57]. It has been demonstrated that only TiO_2NPs in the anatase crystalline phase induce the generation of reactive oxygen species [56], while the mixture of anatase and rutile causes mild DNA damage in human intestinal Caco-2 cells [57].

1.4.2.2 Toxicity of FeNPs

FeNPs are toxic as they are extremely strong reducing agents, forming highly reactive free radicals that can cause cell death and severe damage to tissues. Their toxic effects to humans (lung [58] and nerve cells [59]) and aquatic organisms (groundwater microbial communities [60], medaka fish [61], aqueous cultures of *Escherichia coli* [62] and the *Daphnia magna* communities [63]) have been reported. The impact of nZVI on the organisms again depends on their dose, physico-chemical properties and stability [64].

1.4.2.3 Toxicity of AgNPs

There is increasing evidence for potential human toxicity of AgNPs and possible mechanisms of AgNP toxicity include their adverse effects on cell membranes, mitochondria and genetic material, causing induction of ROS, oxidative stress, genotoxicity and apoptosis [22, 65, 66].

Particularly vulnerable to harmful compounds even at concentrations that are non-toxic for adults is the growing fetus. Although the placenta provides a protective barrier for the entry of harmful substances, previous studies have demonstrated that some NPs

can pass the placental barrier and induce pregnancy or fetal complications in pregnant rodents [67–70]. For AgNPs, no developmental toxicity has been observed after repeated-dose oral administration in rats [71–73]. In contrast, exposure to AgNPs induced teratogenic effects in mice [74] and aquatic species [75, 76]. However, results from animal experiments cannot directly be extrapolated to humans due to substantial differences in placental development, structure and function among species [77, 78]. The most promising and clinically relevant model for studying accumulation and transport of substances across the human placenta is the *ex vivo* human placental perfusion system developed by Panigel et al. [79]. Although this model is increasingly used to study the transfer of different NPs [80, 81], no study with AgNPs has been performed so far. The only available data on potential transplacental transfer of AgNPs are from rodent studies, where increased Ag concentrations were detected in fetal organs [73, 82–84].

However, it is not yet clearly established if Ag transfer occurs in a particulate or ionic form and how different AgNP properties and functionalization affect placental barrier crossing. In general, NP toxicity, cellular uptake or transfer across biological barriers depends not only on particle concentrations, but also on their physicochemical properties [85], surface modification, agglomeration [86] and dissolution [87]. Dissolution of AgNPs, also in complex biological systems, has been widely reported in the literature [88] but there is a lack of consensus if AgNP-mediated toxicity is driven by the particles *per se*, the released Ag, or their combination [89]. Some evidence that the release of Ag ions from NPs is responsible for their toxic effects toward organisms has been provided by several studies showing that AgNPs did not have bactericidal and cytotoxic effects when no dissolution of the NPs occurred [88, 90] or that dissolved Ag had similar neurotoxic effects as AgNPs [91].

1.5 Methods for Quantification and Characterization of Metal-Based Nanoparticles in Environmental and Biological Samples

Despite the broad range of NMs applications, there is lack of data on their occurrence, transformations and fate in environmental compartments and biota. This insufficient information is related mostly to the unavailability of appropriate analytical methods for the reliable determination of NPs in complex matrices. Significant limitations to the development of such methods present the lack of adequate reference standards for NPs [92] and their low concentration in environmental and biological systems (in ng/L to pg/L range) that are lower than the detection limits for most of the existing methods. In addition, environmental and biological samples also carry natural and unintentionally produced NPs which have to be distinguished from measured NPs [6, 93]. Another reason for the lack of analytical methods is related to the unique physical and chemical nature of NPs, where quantitative (mass and number concentration) as well as qualitative information (chemical and physical characterization) is required. Moreover, when NPs dissolve, the release of ionic components must be considered as well. The need for all this information lies in the fact that these properties of NPs are closely related to their behaviour, occurrence and fate in environmental and biological systems [28].

Therefore, it is required to develop new or to improve and validate the already existing methods for achieving a better sensitivity and higher selectivity in order to measure NPs in complex matrices and at relevant analyte concentrations. For detection, quantification and characterization of NPs in those media, a combination of analyses that requires methods for characterizing and/or detecting NPs, and methods for determining their chemical composition is needed [94].

Analytical techniques and methods that proved to be suitable to manage some of the challenges mentioned are listed in Table 1.2: Analytical techniques suitable for analysis of NPs in complex matrices (adopted from [28, 102, 121, 126]). Reported or commonly accepted size and concentration limits of detection (LOD) as well as sample preparations have been included for comparison. The techniques for detection, characterization and/or quantification of NPs have been grouped in five sections covering electron microscopy, light scattering and atomic spectrometry techniques, separation and other techniques [28].

1.5.1 Sample preparation

Most environmental and biological samples containing NPs require preparation prior to most of the analytical techniques. Sample preparation depends on the type of analysis we would like to perform. For instance, for characterization or the detection of NPs the conservation of the original state of the sample is important. The steps for sample preparation should be therefore minimized as much as possible since the original properties of NPs might be changed during the preparation procedure.

1.5.1.1 Digestion

Methods for the determination of NPs chemical composition are based mainly on wet digestion with a strong acid followed by inductively coupled plasma – optical emission or mass spectrometry (ICP-OES or ICP-MS) [93]. For instance, total Ti concentration in nanoscale TiO_2 either suspended in aqueous solutions or in solid matrices has been in general determined after different digestion procedures. TiO_2 samples were decomposed by hot-plate acid digestion with HNO_3 [95, 96], $(NH_4)_2SO_4/H_2SO_4$, HF/H_2SO_4, H_3PO_4 [97], microwave-assisted digestion with $HCl/HNO_3/HF$ [97] or HF/HNO_3 [98] and alkaline fusion with ammonium persulfate [99], $KHSO_4$, $K_2S_2O_7$ or Na_2CO_3 [100, 101]. The drawback of these procedures was incomplete decomposition of TiO_2NPs, resulting in poor recoveries, except in the case of fusion method with ammonium persulfate where the reported recoveries were higher than 95 % [99].

Detection of NPs that are not released in the environment as single particles, but are embedded in a solid matrix or accumulated in biological tissues, require the dissolution of NPs, the degradation of the sample matrix or both [28]. Stable structures, such as inorganic NPs in biological samples can be isolated using sonication of the sample for breaking up tissues or cells followed by chemical or enzymatic digestion of the biological content, vortexing and centrifugation [102]. NPs in biological tissues need to be released from the matrix, preferably without altering their properties. NPs in tissues are generally quantified based on the mass concentrations of the analyte measured after acid digestion of the samples, which leads to dissolution of most NPs. Instead, sample preparation techniques that digest or solubilize the sample matrix without altering the NPs are required. Alkaline solubilization, most commonly used with tetramethylammonium hydroxide (TMAH), was found to be effective for releasing NPs from the tissues of *Daphnia magna* and *Lumbriculus variegatus* (AgNPs, AuNPs) [103], rats (AgNPs, AuNPs) [104, 105], game meat (Pb) [106], ground beef (AgNPs, AuNPs) [103], human synovial fluid (Cr, Co) [107], and from human hepatoma (HepG2) cells (AgNPs) [108] and primary human endothelial cells (AuNPs) [109]. In a similar way, enzymatic treatment with the use of proteases has been applied for extracting NPs from the tissues of rats (AgNPs, AuNPs) [105, 110], earthworms (AgNPs) [111] and chicken meat (AgNPs) [112–115]. Macerozyme R-10, a mixture of pectinase, cellulase and hemicellulase, has been applied for NPs in plants, e.g. shoots of tomato plants (AuNPs) [116], *Lepidium sativum* and *Sinapis alba* (PtNPs) [117], shoots of cucumber, tomato, soybean and pumpkin plants (CeO_2NPs) [118] and roots and shoots of *Arabidopsis thaliana* plants (AgNPs) [119].

However, these techniques may not be useful for less stable, e.g. organic NPs, where different phase-transfer agents can be applied for transferring NPs from the aqueous to the organic phase avoiding their dissolution in the organic phase [120].

1.5.1.2 Filtration and centrifugation

Centrifugation and filtration techniques are well-established tools for size fractionation of NPs and for separation of ENPs from natural colloids. Serial filtration with the use of filters with different pore sizes is usually followed by quantification and characterization of each fraction. Ultrafiltration or dialysis are usually applied for the isolation of ions from NPs. However, these techniques have some limitations. Interactions of NPs and corresponding dissolved species with the membrane surface of the filters (e.g. deposition, clogging) or with the components present in the samples that are too big to pass the filters can affect the filtration recovery, while centrifugation can induce unwanted aggregation of NPs [121].

1.5.1.3 Stabilization

Special care must be devoted to prevent alteration of NPs' physicochemical state during sampling, sample handling and storage as well as during the analytical procedure, which can lead to significant sources of errors due to the unstable nature of NPs. Their tendency to aggregate or become coated with NOM, for example, could significantly alter the dispersion state of NPs, hence quantitative and qualitative results [27]. To avoid underestimation of NPs concentrations in environmental waters, stability of NPs in dispersion throughout the analytical procedure needs to be ensured. In order to prevent agglomeration and settlement of e.g. TiO_2NPs, various sample preparation techniques were used. A procedure based on quantitative phase transfer of hydrophobically modified TiO_2NPs from an aqueous sample to an organic solvent was reported [122], stabilization of TiO_2NPs in solution was achieved by varying pH, concentration of humic acids and alginate [123] and magnetic stirring or ultrasonication under different conditions in the solution (pH, ionic strength, organic colloids) [124] was also applied. Moreover, for efficient dispersion of TiO_2NPs in aqueous samples different dispersing agents were tested [125] considering also the zeta potential as a physico-chemical parameter that influences ion adsorption and electrostatic interactions between charged TiO_2NPs [31]. However, in the above sample preparation techniques, no attempt was made to check whether the dispersed TiO_2NPs enabled their quantitative determination.

Sample collection and preservation of NPs until their analysis are very important as well. Samples of colloids from surface waters, for instance, must be collected in bottles that have been selected for minimum adsorption and contamination, e.g., plastics for inorganic colloids or metal analysis and glass for analysis of organic trace constituents [6].

Table 1.2: Analytical techniques suitable for analysis of NPs in complex matrices (adopted from [28, 102, 121, 126]).

	Technique	Size LOD	Concentration LOD	Analytical information	Sample preparation
Electron microscopy	Transmission electron microscopy (TEM)	<1 nm	µg/L	Size (average and distribution), shape, aggregation, chemical and crystal structure	Drop deposition followed by solvent evaporation, adsorption deposition and ultracentrifugation harvesting, cryofixation, embedding particles in a water-soluble resin
	Field emission scanning electron microscopy (FESEM)	1 nm	µg/L	Size (average and distribution), shape, aggregation, structure	
	Scanning tunnel microscopy (STM)		/	Aggregation, shape, size (average and distribution), structure	
	Atomic force microscopy (AFM)	<1nm	µg/L	Size (average and distribution), shape, aggregation, structure	/
	Environmental scanning electron microscopy (ESEM)	30 nm	10^{12}/L µg/L	Size (average and distribution), shape, elemental composition	/
Atomic spectrometry	Inductively coupled plasma mass spectrometry (ICP-MS)	/	ng/L	Bulk element composition, total mass concentration	Minimal pretreatment for liquid samples (e.g. filtration), acid digestion, alkaline or enzymatic treatment of solid samples
	Single particle ICP-MS (SP-ICP-MS)	10-20 nm	10^6 /L ng/L	Detection of dissolved/NP element, element mass per NP, size (average and distribution), number and mass concentration	
	X-ray absorption spectroscopy (XAS)	<1nm	mg/kg	Identification/quantitative distribution of chemical species, chemical composition, oxidation state	
Separation techniques	Size-exclusion chromatography (SEC)	<1 nm	1 µg/L *	Size (average and distribution), mass concentration, detection of dissolved/NP element	Dilution or preconcentration of the liquid samples with an emphasis on the appropriate mobile phase, alkaline or enzymatic treatment of solid samples
	Hydrodynamic chromatography (HDC)	5 nm	1 µg/L *	Size (average and distribution), mass concentration, detection of dissolved/NP element	
	Capillary electrophoresis (CE)	5 nm	0.2 µg/L *	Size (average and distribution), mass concentration, detection of dissolved/NP element, surface charge, electrophoretic mobility	
	Field-flow fractionation (FFF)	1-5 nm	1-10 µg/L *	Size (average and distribution), mass concentration, detection of complexed/NP element	
Light scattering	Dynamic light scattering (DLS)	3 nm	mg/L	Hydrodynamic diameter, size distribution	/
	Nanoparticle tracking analysis (NTA)	20 nm	10^9 /L	Size (average and distribution), number concentration, charge	/
Other techniques	Particle collision coulometry (PCC)	5 nm	10^{10}/L	Detection of NPs, size (average and distribution), number and mass concentration	/
	Zeta potential			Surface charge, aggregation	/
	Laser ablation (LA)	100 nm	mg/L	Quantitative imaging of NPs in solid samples	Cryofixation, fixation with a paraformaldehyde, dried-droplets deposition

*Concentration LOD for separation techniques coupled to ICP-MS.

1.5.2 Electron microscopy

Electron microscopy (EM) is one of the most commonly used techniques for visualization of inorganic ENPs, giving information about their size, shape and aggregation state [27]. In particular, transmission electron microscopy (TEM), scanning electron microscopy (SEM) and atomic force microscopy (AFM) have been very effective at the characterization

of specific NPs in samples ranging from simple solutions to plants and animals. Transmission electron microscopy (TEM) beside particle sizing and morphology also enables the determination of the chemical and crystal structure of NPs. Microscopy techniques are often used as a complementary methods to verify the quality of the particle sizing data obtained from other, e.g. separation techniques [127].

However, EM often cannot image the surface groups of functionalized NPs (inorganic NPs with an organic coating) since they do not deflect an electron beam sufficiently. Sample preparation, which involves transformation of the sample from its dispersed hydrated state to a dried high vacuum state (e.g. drop deposition followed by solvent evaporation, adsorption deposition and ultracentrifugation harvesting) [27], can be time-consuming and might also alter the physicochemical state of the NPs [102]. While no liquid samples can be introduced to the sample chamber of TEM due to the requirement of high vacuum, atomic force microscopy (AFM) and environmental scanning electron microscopy (ESEM) enable imaging under ambient conditions. However, alterations of the samples can still occur by applying the sample to the holder [121, 128]. Moreover, although EM provides true particle size dimensions, it cannot be considered as a quantitative technique due to the small amounts of samples that can be analyzed, influencing the statistical significance of the results [121].

1.5.3 Light scattering techniques

Among light scattering techniques the most commonly used is dynamic light scattering (DLS), also referred to as photon correlation spectroscopy. DLS is the standard method for rapidly determining the particle diameter, size distribution of NPs and their aggregation state in suspensions. The pace of the movement of particles (Brownian motion) in solution is inversely proportional to the hydrodynamic diameter. When the particles are lightened with a laser beam, they scatter time-dependent fluctuations in light intensity, which can be directly correlated to diffusion coefficients of the particles doing the scattering. DLS is an accurate, fast, simple to perform and non-destructive technique but the results may be influenced by the presence of interfering particles with heterogeneous size distributions, as in the case of most environmental and biological samples. Namely, DLS is solely quantitative and unless the sample content is known or pure, size fractions cannot be related to particles of a specific composition. Another limitation of DLS is its inability to detect the presence of smaller particles among bigger ones [3, 28, 102, 121].

1.5.4 Atomic spectrometry techniques

Atomic spectrometry techniques, such as electrothermal atomic absorption (ET-AAS), inductively coupled plasma optical emission spectrometry (ICP-OES) and inductively coupled plasma mass spectrometry (ICP-MS), can be used for identification and quantification of inorganic ENPs. While limits of detection (LOD) for ICP-OES are in the range of µg/L, ET-AAS and ICP-MS are more sensitive techniques with LOD down to ng/L. These techniques generally require the introduction of liquid samples, where suspensions of NPs can be directly analyzed. Solid samples, on the other hand, must either undergo sample pretreatment for the digestion of the matrix or can be analyzed directly by applying laser ablation (LA). Atomic spectrometry techniques can only provide a total amount of the particular metal and do not allow to differentiate between single particles and agglomerates or ionic species. Also, they do not give any information about NPs characteristics (e.g. size, aggregation), unless coupled to continuous separation techniques (e.g. chromatography) [128].

1.5.4.1 ICP-MS

ICP-MS as a highly sensitive and selective analytical tool, providing fast multielemental analysis, wide dynamic range and low LOD, has been recognized as a valuable tool in the detection and quantification of metal-based NPs. ICP-MS generates a mass spectrum of ions represented as mass-to-charge (m/z) ratio, by first ionizing the sample in the plasma, separating the ions of differing masses with mass analyzer, and recording their relative abundance by measuring intensities of the ion flux with a detector system [129].

Liquid samples of NPs are introduced into the ICP as airborne particles suspensions using pneumatic nebulizers to introduce solution samples into the ICP as fine aerosols. Big droplets are removed in spray chamber before being introduced into plasma.

The plasma used is made by partially ionizing argon gas. The generator establishes oscillating electric and magnetic fields at the end of the torch. When a spark is applied to the argon flowing through the ICP torch, electrons are stripped off of the argon atoms, forming argon ions. These ions are caught in the oscillating fields and collide with other argon atoms, forming an argon discharge or plasma [130]. The sample aerosol is in plasma that can reach a very high temperature (up to 10,000 K) completely desolvated and the elements in the aerosol are converted first into gaseous atoms and then ionized towards the end of the plasma.

Ions are then brought into the mass spectrometer via the interface cones allowing transmitting the ions from the argon sample stream at atmospheric pressure into the low pressure region of the mass spectrometer. The ions from the ICP source are then focused by the electrostatic lenses in the mass spectrometer.

Different mass analyzers, such as ion trap, time-of-flight or quadrupole, which cover different mass-to-charge ranges and differ in mass accuracy and resolution, exist [121]. Quadrupole, which uses a combination of direct and alternating current to separate ions based on the m/z ratio, is the most commonly used in ICP-MS. The quadrupole comprises of two pairs of cylindrical rods, arranged in a square, where both currents give a hyperbolic electrical field and allow only a narrow range of masses to be transmitted, while the rest are lost from the beam. By altering the currents and keeping the ratio between them constant, it is possible to control which masses are passed to the detector.

Electron multiplier transforms a single ion into a measurable single pulse, by amplifying the signal with a set of cascade dynodes. In case of high ion counts the detector becomes saturated and fails to regress some of the ions, leading into the non-linear response. Therefore, at low ion rates, counting in pulse mode is applied, while at high counts, analogue mode is used where the current is measured rather than each single pulse [130]. The detector provides low background and wide dynamic linear range up to 9 orders of magnitude, which allows detection of both major constituents and trace components at the same sample dilution [131, 132].

1.5.4.2 Single particle ICP-MS

An emerging and promising approach for detecting, quantifying and characterizing metal-based NPs is single particle ICP-MS (SP-ICP-MS), first developed by Degueldre and Favarger [133]. SP-ICP-MS technique provides:

- Characterization information about the mass of element per particle, which can be converted into particle size as long as information about the composition, shape and density of the particles is known or assumed.
- Quantitative information about particle number concentrations, as well as mass concentrations of the dissolved and/or particulate forms.

The major advantages of SP-ICP-MS over other characterization and detection techniques are its superior sensitivity (down to the ng/L) and element specificity that may overcome

complex matrices and extremely low NPs concentrations in environmental samples. It is also able to distinguish between the presence of particulate and/or dissolved forms of specific elements [134]. Another significant advantage of SP-ICP-MS is its ability to analyze particles in complex matrices without significant sample preparation. While other analytical techniques may introduce artifacts during sample preparation and analysis (e.g. aggregation, dissolution), SP-ICP-MS is able to characterize and quantify the NP analyte in its native media, where only dilution is required. This allows direct examination of transformation processes, and other physicochemical properties (e.g. size, shape, and elemental distribution of the particles) [135]. In addition, since determination of the size distribution in SP-ICP-MS is based on the particle number, this technique is suitable for the implementation of the European Commission definition of nanomaterial [2].

The use of SP-ICP-MS has so far been demonstrated to be suitable for detection of a wide range of metal-based NPs, most commonly Au NPs [103, 105, 136–143] and Ag NPs [103, 112, 115, 137, 138, 142, 144–155], as well as other types of NPs, i.e., TiO_2 NPs [133, 137, 142, 148, 155–157], Al_2O_3 NPs [133], FeOOH NPs [133], Fe_2O_3 NPs [158], Cr_2O_3 NPs [158], ZnO NPs [149, 159, 160], CeO_2 NPs [148, 160], ZrO_2 NPs [161], ThO_2 NPs [162], colloidal As [163], SiO_2 NPs [137] and CuO NPs [164].

1.5.4.2.1 Fundamentals In SP-ICPMS, after introducing a sufficiently diluted suspension of NPs in ICP-MS, an aerosol of polydisperse droplets is produced and NPs are volatilized, atomized and subsequently ionized in a plasma. While soluble forms of an element are distributed homogenously within a solution, producing a constant flux of ions, hence steady signal during the reading period, the element in the suspension of NPs is not distributed homogenously, since it is present just in the discrete particles. Therefore, the pack of ions generated from each single particle can be detected by using fast data acquisition (i.e. short dwell times) (Figure 1.2). Working at short reading times (from few µs to few ms), each NP is measured as single pulse. ICP-MS signals are recorded during several minutes, obtaining time scans, consisting of a number of events, recorded as pulses above a steady baseline, as shown in Figure 1.2. While the intensity of each event is due to the ions detected from each particle, the baseline is due to the instrumental background at the mass recorded or to the presence of dissolved forms of the element measured. Raw time scans can be processed by plotting the event intensity vs. the event intensity frequency, obtaining histograms as shown in Figure 1.2, where the first distribution is due to the background and/or the presence of dissolved forms of the element measured and the second to the particles themselves [168].

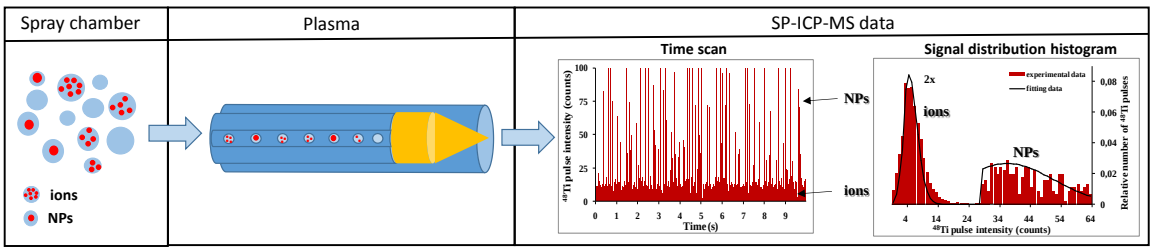


Figure 1.2: Schematic presentation for the introduction of suspension of NPs and ions into ICP-MS system, their volatilization, atomization and ionization in the plasma and data processing by SP-ICP-MS (adopted from [150]).

The basic assumption behind SP-ICP-MS is that each recorded event represents a single particle. Therefore, the number of events counted (n_p) during an acquisition time (t_d) is directly related to the number concentration of particles (C_p):

$$n_p = \eta_{neb} \times q_{liq} \times t_d \times C_p \tag{1}$$

where η_{neb} is the transport (nebulization) efficiency and q_{liq} the sample introduction flow rate. On the other hand, the intensity of each event (I_p) is proportional to the number of atoms of the element monitored in each detected particle, and hence to the mass of element per particle (m_p). If the analyzed particle consists of more than one element, the mass fraction (f_a) is used to convert the signal from the singular element to an overall mass of particle [135]. The relationship between the measured intensity of each particle event and the mass per particle can be calculated by Eq. (2):

$$\mathrm{m_p} = \frac{(\mathrm{I_P} - \mathrm{I_{bkg}})}{\mathrm{f_a} * \mathrm{m}} \tag{2}$$

where m is the sensitivity and I_{bkg} is the average signal intensity in blank samples, both determined from the mass flux calibration curve (Eq. (3)), prepared by plotting the mass concentration of dissolved standard (C) versus the most common signal intensity in a signal distribution histogram.

$$\mathrm{W} = \eta_{\mathrm{neb}} \times \mathrm{q_{liq}} \times \mathrm{t_d} \times \mathrm{C} \tag{3}$$

The m_p can then be related to the size of the particle if the composition, shape and density of the particle are known. A diameter (d) for a solid, homogeneous and spherical particle can be calculated as follows:

$$\mathrm{d} = \sqrt[3]{\frac{6 \times \mathrm{m_p}}{\rho \times \pi}} \tag{4}$$

where ρ is the density of the element in the particle.
Details of approaches used for data processing and interpretation of SP-ICP-MS analysis can be found in the literature [130, 134, 149].

1.5.4.2.2 Determination of particle size The intensity of the pulse generated by a single NP and detected by ICP-MS can be related to the NP size only if the composition, shape and density of the NP are known. Ideally, when standards of reference NPs of the same elemental composition as sample analyzed with known mass per NP or known size are available, Eqs. (2) and (4) can be used to construct the corresponding calibrations to obtain information about the mass per particle and the size of NP in the samples, respectively [151]. However, since reference materials with a well-characterized size do not exist for each type of NPs, sizing has to be performed following the procedure developed by Pace et al. [150] with the use of dissolved standards of the element measured. The determination of the mass of analyte per NP can be done by correlating ICP-MS response from NPs entering the plasma to mass of metal in dissolved standards (Eqs. 2 and 3), assuming that the element from the dissolved standard solution and from a NP behave comparably in the ICP [168]. Finally, each particle mass is then converted into a particle diameter using Eq. (4), which allows the determination of particle size distribution.

Before sizing, the events associated to NPs have to be distinguished from the baseline produced by the background. The most important contribution to the background intensity arises from the dissolved component of the element in the solution, isobaric and/or polyatomic interferences (if these are not adequately eliminated) and the instrument background. Different criteria are used for discrimination of particulate signal from the continuous background. While signal deconvolution method has been developed to discriminate smaller NPs [142], the most basic and commonly used approach is an iterative algorithm [144, 165], usually applying 3σ or 5σ threshold criteria, where σ is the standard deviation of the continuous background. First, the full data set is averaged, and pulses above 3σ or 5σ are separated. This process is subsequently repeated, until the baseline concentration remains at a constant value. Then, once the baseline is established, pulses above 3σ or 5σ are gathered and defined as NPs [165].

In a similar way, size detection limits are usually calculated by using a 3σ criterion. By using this criterion and the instrument sensitivity, Lee et al. estimated size detection limits for SP-ICP-MS for NPs composed of 40 different elements [167]. While size detection limits between 10 and 20 nm can be achieved for metal NPs, the sizes for metal oxide NPs increase, depending on their stoichiometry and composition. Detection limits can be improved by using instruments with better ion transmission, hence higher detection efficiency and lower background signals, by using dwell times in the microsecond range and collision/reaction cells for isotopes subjected to polyatomic background interferences [128].

On the other hand, the upper size limit for particle characterization in SP-ICP-MS is limited by the selective removal of large particles in the spray chamber, their incomplete vaporization in the plasma [168] and saturation of the detector when a high amount of counts are detected due to the ionization of the big particle [158].

1.5.4.2.3 Determination of particle concentration Quantitative determination of the particle number concentrations is based on the linear relationship between the number of events and the number concentration (Eq. (1)). The number of NP/mL in a sample can be determined by dividing the measured number of detected particle events per second by the transport efficiency and by the sample flow rate to the nebulizer [135]. Number concentration detection limits depend on the nebulization efficiency, sample flow rate and on the time spent counting particles, i.e. the acquisition time [168]. In practice, the number concentration detection limits in the range of 10^6/L are reported with current ICP-MS instruments and acquisition times around one minute.

In a frequency distribution histogram (Figure 1.2b), specific information about the occurrence of dissolved and NP forms of the element measured can be obtained. If both distributions are fully resolved, the first one represents the dissolved form of the analyte, whereas the second one resembles the size distribution of the NPs. However, the distributions cannot be resolved in case of high concentration of dissolved forms or the small size of the NPs [168]. Mass concentration of NPs can be determined in single particle mode by summing up the pulse intensity of the events recorded or by integrating the corresponding histograms (sum of the pulse intensities multiplied by the number of pulses). The signal is then converted into mass concentration with the use of corresponding calibration with dissolved standard. If such integration is performed for the different distributions obtained in the histograms, the content of the element as NPs and as dissolved forms can be obtained in terms of mass concentration if both distributions are fully resolved [168].

1.5.4.2.4 Determination of transport efficiency For the accurate conversion from the signal intensities to particle sizes, the transport efficiency of the ICP-MS must be established. The transport efficiency is defined as the ratio of the amount of analyte

entering the plasma to the amount of analyte aspirated. The need for the transport efficiency lies in the difference between the mass transport of a single nanoparticle through the nebulizer/ spray chamber system as compared to that of dissolved ions in solution. To convert pulse intensity to particle mass using a dissolved metal calibration curve, the transport efficiency is needed to relate the concentration of the metal standard to a total mass flux (Eq. (2)) [150].

Several ways for determining the transport efficiency have been reported [150], where a "particle frequency" and "particle size" method are the most commonly applied.

- For the determination of the transport efficiency based on the "particle frequency" method, a suspension of reference NPs with a known average particle diameter and known mass concentration is required. The transport efficiency is calculated as the percentage of all NPs detected by SP-ICP-MS versus the theoretical (calculated) particle number in the introduced sample volume [150].
- The transport efficiency according to the "particle size" method is determined in the following way: First, a calibration curve that relates signal intensity (peak maximum of the intensity distribution) to particle mass needs to be created using the reference NPs with a known particle size. Second, a corresponding calibration curve has to be constructed by determining the average signal intensity for ionic standards. The concentration is then converted to mass by multiplication with a sample flow rate and dwell time. The transport efficiency is determined by dividing the slope from the calibration curve made from the ionic standards by the slope from the calibration curve created from the NPs [150].

Reported values in the literature typically range from 1 to 10 % but can be much higher for high-efficiency nebulizer systems. Since these values depend not only on the components of the sample introduction system (i.e., nebulizer, spray chamber) but also on various operational parameters, such as gas flow, uptake rates and sample viscosity, the transport efficiency can vary. Therefore, the transport efficiency needs to be measured on a regular (daily) basis for accurate sizing and counting results [150].

1.5.4.2.5 Sample dilution Optimizing the dilution factor is a critical step in SP-ICP-MS analysis, when using a time resolution in the millisecond range (3–10 ms), especially when analyzing unknown samples. Increasing the dilution factor reduces the probability of more than one particle being measured within a reading time and being counted as one particle (i.e., multiple-particle event). High dilution factors also improve the size detection limit, by decreasing the background signal and signal variation of dissolved species, which may overwhelm the signal of smaller particles and make their detection impossible [164]. Moreover, the dilution of sample helps also in overcoming matrix effects and enables sizing of NPs in complex matrices [165]. However, when the dilution factor is too high, extended measurement times are required to obtain sufficient particle events, which increase the chance of false positive signals, measurement time and costs of analysis [164]. Therefore, an optimal dilution factor has to be selected as a balance between the low background signal intensity and a sufficiently high amount of detected particle events.

1.5.4.2.6 Dwell time For the accurate detection of NPs by SP-ICP-MS, the dwell time should be carefully selected. It should be long enough to collect the entire signal from one NP and to ensure that the measurement of one NP is not divided between two consecutive dwell times. The partial measurement of a NP would lead to an underestimation of the particle size and an overestimation of the particle number concentration. A sufficiently long dwell time is also important for ensuring an accurate discrimination of the NP signal from the background signal [143]. On the other hand, the dwell time should be short enough to avoid the measurement of two NPs in a single integration period, which would lead to

an overestimation of the size of the NPs, and an underestimation of the particle number concentration [139, 151, 152].

1.5.4.2.7 Instrumentation and data processing SP-ICP-MS was primarily used on quadrupole instruments, which are usually limited by longer reading times in millisecond range (between 3 to 10 ms dwell time per isotope) [168], enabling of recording the particle events as pulses. Recently, fast scanning quadrupole instruments have become commercially available, which provide continuous measurements at dwell times in the microsecond range (100–10 µs) without any settling time. They can record particle events as resolved transient signals and monitor up to two isotopes/elements in the same particle [169]. Moreover, an ICP time-of-flight MS with a temporal resolution of 30 µs was developed recently, which enables simultaneous detection of multiple isotopes [170]. This allows determination of the elemental composition of single NPs as well as the discrimination of ENPs from natural NPs [160].

The data measured by SP-ICP-MS can be processed in different ways. The raw data are usually exported to spreadsheets, the most commonly used being the one from RIKILIT [171], which enables calculation of particle sizes and concentrations from data acquired at milliseconds dwell times. On the other hand, manufacturers of ICP-MS instruments are incorporating different softwares for acquisition and processing of single particle data [172].

1.5.4.2.8 SP-ICP-MS spectral interferences The ICP-MS measurements of some isotopes are hampered by spectral interferences caused by isobaric isotopes or polyatomic species originating from argon and/or sample matrix [173]. Moreover, in analysis of NPs, potential additional interferences can come from chemical synthesis processes of NPs, colloidal stabilizers or from elements in NP composition [158]. For instance, ^{48}Ti isotope can suffer from polyatomic interferences from sulphur and nitrogen compounds (e.g. $^{32}S^{16}O^{+}$, $^{34}S^{14}N^{+}$) arising from ammonium persulfate which can be used for the digestion of TiO_2NPs, or from isobaric interference of ^{48}Ca, which is an element commonly present in high concentrations in environmental waters [41]. Another element that suffers from spectral interferences is Fe, which has on m/z 56 polyatomic interferences that originate from plasma ($^{40}Ar^{16}O^{+}$) or sample matrix ($^{40}Ca^{16}O^{+}$) [174–176].

In order to diminish the influence of isobaric interferences on the measurements, the detection of another, non-interfered isotope of the analyte can be used. However, this leads to a drop in sensitivity and to the increase of the size detection limit in SP-ICP-MS analysis. The second approach, i.e. the use of mathematical correction based on the measurement of signals from non-interfered isotopes of the interfering element, is not even feasible when quadrupole is used for SP-ICP-MS. Namely, scanning over two isotopes using short dwell times with significant settling times is not possible [158]. The spectral interferences on ICP-MS can be generally more effectively diminished by the application of collision or reaction cell technology. In a few SP-ICP-MS studies, collision [158] or reaction [177–179] cell gases applying single quadrupole MS analyzer have been shown to be effective in diminishing the interference ions and reducing the background noise and limit of detection. Moreover, the triple quadrupole ICP-MS applying reaction cell technology in MS/MS mode was successfully used in several applications [173], but has been rarely applied in SP-ICP-MS analysis [180].

A common interference in SP-ICP-MS is the presence of dissolved analyte content which can originate from either the matrix or from the partial dissolution of the NPs. The continuous background signal produced by dissolved analyte in SP-ICP-MS can mask the signal peaks from small NPs, which therefore cannot be resolved from the background. One of the effective and practical solutions to this interference is the dilution of the NPs suspension, which does not affect the signal originating from NPs but it effectively

diminishes the background signal. However, the total acquisition time then has to be increased in order to maintain the statistical relevance of the data [158]. Another solution for reducing the dissolved background is the use of shorter dwell times (100 µs or shorter) which increase the ratio of NP analyte signal to the background signal [135]. Alternatively, the signal from dissolved analyte can be reduced or possibly eliminated by coupling ion exchange chromatography to SP-ICP-MS in order to remove the dissolved analyte [181].

1.5.4.2.9 Limitations of SP-ICP-MS Despite many advantages of SP-ICP-MS, some limitations of this technique still prevent it to become widely applicable for detecting ENPs in environmental and biological samples. This is related mostly to instrumental limitations of SP-ICP-MS and consequently to the fact that NPs consisting of only one metal with relatively big sizes (> 20 nm) can be determined. Detection of NPs, especially of metal oxides, in the low nanometer range is often impossible since low intensity signals are hindered by the instrumental/dissolved background. However, it is expected that the ongoing development of ICP-MS instrumentation will improve size detection limits and implement multielement capabilities for heterogeneous NPs [129, 168]. Moreover, an excessive sample dilution of the NPs suspensions may create greater uncertainty in NP counting due to subsequent manipulation and changes to the sample chemistry affecting transformation of NPs (dissolution, agglomeration, etc.) [138]. Also, for accurate determination of NP size by SP-ICP-MS, the shape and chemical composition of the analyzed NPs need to be known.

Before SP-ICP-MS could be considered a mature methodology, additional work is needed to standardize it, including the assessment of the reliability and variability of size and concentration determinations. To achieve this, standard reference materials of NPs with very carefully determined NP properties are needed.

In any case, the number of environmental and biological applications of SP-ICP-MS is steadily increasing, mainly because ICP-MS-based methods are the only currently known methods that are both selective and sensitive enough to analyze inorganic ENMs in complex samples [182]. However, in most cases solving analytical problems related to ENPs in environmental and biological samples must still involve a combination of SP-ICP-MS with other techniques.

1.5.5 Separation techniques

Isolation of NPs from matrix and determination of their size and size distribution can be accomplished also by different separation techniques, such as size-exclusion chromatography (SEC), hydrodynamic chromatography (HDC), field flow fractionation (FFF) and capillary electrophoresis (CE). Since these methods are non-destructive, they allow further analysis when combined with other techniques (e.g. ICP–MS) [26]. By attaching traditional analytical tools (e.g. ICP–MS) as detectors to size separation techniques, it is not only possible to quantify different NPs in environmental or biological samples, but also to characterize their size and size distribution.

1.5.5.1 Size-exclusion chromatography

SEC is a chromatographic method in which molecules in the solution are separated by their size and, in some cases, molecular weight. The particles with diameters that are larger than the size of pores elute faster than the particles smaller than column pores. Peak elution times of the analytes can thus be quantitatively correlated to the hydrodynamic volume or molecular mass of a compound by using calibration standards with a well-known size or molecular mass. SEC can be applied for characterization and separation of differently shaped NPs with good separation efficiency and also for isolating NPs from water. So far,

SEC has been used for measurements of CdSe NPs [183] and AuNPs [184, 185]. However, the major disadvantage of SEC includes limited size separation range of the columns and the unspecific adsorption of different metal NPs onto porous chromatographic supports, which leads to poor column recoveries.

1.5.5.2 Hydrodynamic chromatography

HDC is like SEC a size-based separation method where the column is packed with nonporous microparticles, achieving separation by flow velocity and the velocity gradient across them. In narrow channels with a laminar flow, larger molecules or particles are transported faster than smaller ones since they cannot fully access slow-flow regions near the channel walls. Some possible advantages of the HDC system are fast analysis, high efficiency, reduced solvent consumption, reduced risk of solid-phase interactions and easy temperature control [127]. HDC coupled to ICP-MS has been used for simultaneous determination of TiO_2NPs, SiO_2NPs, Al_2O_3NPs, Fe_2O_3NPs [126] and AgNPs [185] in environmental samples. Benefits of HDC coupled to ICP-MS are extended sizing range (5 to 300 nm) and limited sample pre-treatment required with the multi-element selectivity of ICP-MS. Overall, this methodology can be suitable for the routine size and elemental characterisation of inorganic ENPs in environmental and biological studies. However, the noise level of the detection is high and unstable during the experiments and the column is more likely to get clogged [127].

1.5.5.3 Field flow fractionation

Another promising technique for size separation of NPs is FFF, where separation is based on the diffusion coefficient. The particles are separated based on how they are affected by an applied field which controls the particle transport velocity by positioning them in different average laminar flow vectors in a thin channel. Different force fields (liquid flows, centrifugal forces, temperature gradients or gravity fields) are applied perpendicularly to the separation channel. The most common is a hydrodynamic flow which is applied perpendicularly to the direction of the mobile-phase flow, which carries the analyte. While bigger particles move with the perpendicular force to the side of the channel, the smaller one diffuses more easily back to the centre of the channel. Since the mobile-phase flow is higher at the centre of the channel, smaller analytes elute earlier than larger ones [102, 121]. The different retention times for various peaks usually indicate the size of the aggregates since the retention times can be related to the diffusion coefficient of the aggregates [26, 128].

When FFF is coupled to an elemental specific detector, such as ICP-MS, particle composition as a function of hydrodynamic size can be determined [187]. In combination with ICP-MS, several applications using FFF demonstrated its potential for the characterization of ENPs [115, 187–198] in different environmental and biological samples. However, FFF analysis can be complex and time consuming with increasing possibility of particles aggregation in the channel and their interactions with the membrane. In some cases, preconcentration of the samples is needed, while in case of too high particle concentration, overload of the channel can occur, resulting in peak broadening and loss of resolution [126].

1.5.5.4 Capillary electrophoresis

Electrophoretic separation of NPs is mainly based on particle size and shape, while the electrophoresis of functionalized NPs is influenced by quantity, chemical groups and ionization of these functional groups. Electrophoresis is used for measuring zeta potential

which is a measure of the overall charge of particles dispersed in a specific medium and gives an indication of the potential stability of a colloidal system [121].

The analytes in CE separate as they migrate through the capillary due to their electrophoretic mobility and are separated based on correlation between electrophoretic mobility and NP diameter (in the range 5 – 1000 nm). CE is particularly well suited for size separation of a mixture of water-soluble and charged ENPs, since electrophoretic mobility is a function of the zeta potential of the NP. The limitation of commercially available CE systems is the lack of sensitivity of on-line detectors (typical CE detectors are based on UV/Vis absorption, fluorescence spectroscopy, conductivity or MS), therefore on-line preconcentration technique should be applied for sensitive detection of NPs. The other disadvantage of CE is also its lower reproducibility when compared to other chromatographic methods [26, 102].

Chapter 2

Aims and Hypothesis

Due to the extensive use of NPs in various applications it is inevitable that they will be released into the environment and come into contact with biological systems. In order to predict the potential toxic effects, fate and occurrence of NPs in the environmental and biological systems, the concentration and size of metal-based NPs, as well as their aggregation/dissolution and interactions with other compounds are the key parameters to be determined. It is therefore necessary to optimize a sensitive, reliable and selective SP-ICP-MS method for the detection and characterization of the most commonly used metal-based NPs (TiO_2NPs, AgNPs, nZVI) in complex matrices. Special care should be devoted to the sample preparation and stabilization of NPs throughout the analytical procedure, as well as to the quantitative extraction of NPs from biological matrices without changing their original properties. Analytical procedures for the analysis of metal-based NPs in different environmental and biological samples should be optimized for each NPs type.

Aims of the present doctoral dissertation were:

- To investigate the conditions which would ensure the stability of TiO_2NPs throughout the analytical procedures with the use of various approaches for stabilization of TiO_2NPs in solution (mechanical shaking, ultrasonication, the use of different dispersing agents) and to study the influence of sample matrix (i.e., river water and wastewater) on the dispersion efficiency.
- To optimize SP-ICP-MS method for determination of size and concentration of TiO_2NPs (anatase and rutile) and dissolved Ti, as well as to apply the procedure for analysis of TiO_2NPs in environmental water samples.
- To optimize the instrumental parameters for sensitive and interference-free measurement of nZVI by SP-ICP-MS applying triple quadrupole ICP-MS equipped with reaction cell technology in MS/MS mode and to follow the settlement and aggregation of nZVI after the wastewater treatment under the optimized measurement parameters by SP-ICP-MS, considering the changing composition of nZVI over time. The next aim was to investigate the influence of sample matrix, iron load and settling time on nZVI behaviour. The objective was also to study the interactions of nZVI with Cd^{2+} in different contaminated waters by measuring Cd in SP-ICP-MS mode and to evaluate the efficiency of Cd^{2+} removal from different water matrices by nZVI.
- To investigate the translocation of AgNP across the human placental barrier in dependence of different surface functionalization (sodium carboxylate (COONa) versus polyethylene glycol (PEG)). Since AgNPs are partially soluble, one of the aims was also to distinguish between the transfers of ionic or particulate Ag by SP-

ICP-MS and possible precipitation of AgCl NPs, which may occur in the presence of chloride ions.

- To compare the two potentially suitable sample preparation methods, alkaline treatment with the use of the strong base TMAH and enzymatic treatment with the use of the stable and highly active enzyme Proteinase K, for releasing two types of AgNPs from human placenta. The objective was also to apply the most appropriate treatment process for quantification and characterization of AgNPs accumulated in human placenta in the *ex vivo* human placental perfusion model.

Chapter 3

Materials and Methods

3.1 Reagents and Materials

MilliQ water (18.2 MΩ cm) (Millipore, Bedford, MA, USA) was used for sample preparations and sample dilutions.

Standard TiO_2NPs dispersions were prepared using anatase TiO_2 nanopowder (< 25 nm particle size, spherical shape) (#637254) and rutile TiO_2 nanopowder (< 100 nm particle size, rod shape with a diameter of about 10 nm and length of 40 nm) (#637262), both obtained from Sigma-Aldrich (St. Louis, USA). The declared specific surface area of anatase and rutile was 45-55 m^2/g and 130-190 m^2/g, respectively. The declared density at 25 °C was for anatase and rutile 3.9 g/mL and 4.17 g/mL, respectively. According to the manufacturer, rutile nanopowder may contain up to 5 wt. % silicon dioxide (SiO_2) as a surface coating.

For the determination of total Ti concentrations by ICP-MS, dissolved Ti standard solutions (Merck Millipore) of 1000 ± 4 mg/L were prepared in 0.1 % nitric acid and used for preparation of the calibration curves, while Rh standard solution (25 µg/L) prepared from stock standard (Merck) of 1000 ± 10 mg L^{-1} was used as an internal standard.

Nitric acid (65 % HNO_3), hydrochloric acid (30 % HCl), hydrofluoric acid (40 % HF), boric acid (H_3BO_3) and ammonium peroxo disulfate ($(NH_4)_2S_2O_8$) supplied from Merck Millipore were used for the microwave-assisted digestion of the TiO_2NPs samples.

In order to test the stability of TiO_2NPs suspension, different dispersing agents were used: PEI 600 (polyethyleneimine) (Alfa Aesar, Germany), Darvan C (ammonium polymethacrylate) (Vanderbilt Minerals, USA) and Triton X-100 (98-100 %) (Merck Millipore).

Standard dispersions of AgNPs with 20 and 40 nm diameters, purchased from Sigma-Aldrich and a reference AuNP suspension (RM 8012) obtained from NIST (Gaithersburg, MD, USA) were used for the determination of the transport efficiency. The AgNPs suspensions were supplied at a nominal concentration of 20 ± 1 µg Ag/L and were stabilized in an aqueous sodium citrate buffer, while the AuNP suspensions were supplied at a nominal concentration of 48.17 ± 0.33 µg Au/L. The declared nominal sizes, determined by TEM, were 20 ± 4 nm and 40 ± 4 nm for the AgNPs and 27.6 ± 2.1 nm for the AuNPs. The AgNP and AuNP suspensions were made by diluting the stock solution with water to final concentrations ranging from 0.010 ng/mL to 2 ng/mL. The dissolved Ti and Ag stock standard solutions of 1000 ± 4 mg/L and Au standard of 1000 ± 2 mg/L ([$H(AuCl_4)$ $3xH_2O$ in 12.7 % *HCl*] *Titrisol*®Merck), all obtained from Merck, were used for the preparation of the calibration curves. They were prepared in 0.1 % nitric acid in the concentration range from 0.010 ng/mL to 10 ng/mL.

Nanoremediation processes were performed with a commercially available nZVI Nanofer25 slurry in the form of a stable water-based dispersion containing 20 wt. % of bare FeNPs, supplied by NANO IRON, s.r.o. (Rajhrad, Czech Republic).

The transport efficiency of the liquid samples through the sample introduction system was determined by measuring blank (MilliQ water) and two concentration levels (0.5 and 1.0 µg/L) of dissolved Au solution and a reference AuNP suspension (RM 8012) with a known average particle diameter (27.6 ± 2.1 nm) and known Au mass concentration (48.17 ± 0.33 µg/g). Stock standard solutions of ionic Fe and Cd (1000 ± 4 mg/L in 2-3 % HNO_3, Merck) were used to prepare calibration curves. For sizing and quantification of nZVI and for quantification of Cd^{2+} adsorbed on nZVI particles, a blank (MilliQ water) and Fe standards (0.5 to 2.0 µg/L) or Cd standards (0.5 and 1.0 µg/L) were applied, respectively. To study the influence of Ca on Fe determination by QQQ ICP-MS, 50 µg/L Ca solution was prepared from stock standard (1000 ± 4 mg/L in 2-3 % HNO_3, Merck). Surface (SPS-SW1) and wastewater (SPS-WW1) reference materials with certified Fe concentration 20 ± 1 µg/L and 1000 ± 5 µg/L, respectively, both supplied by Spectrapure Standards As (Oslo, Norway), were used to check the accuracy of Fe determination.

Synthetic wastewater was prepared similarly as recommended by the OECD guideline. 160 mg of peptone (peptonwater, buffered according to ISO 6579, for microbiology), 30 mg of urea (for biochemistry), 7 mg of NaCl (s.p., 99.99 %), 4 mg of $CaCl_2{\cdot}2H_2O$ (p.a.), 2 mg of $Mg_2SO_4{\cdot}7H_20$ (p.a.), all supplied by Merck, and 28 mg of K_2HPO_4 (99 %), obtained from Honeywell (Riedel-de Haën, Germany), were dissolved in 1 L of MilliQ water.

AgNPs thiolated with two different surface modifications: polyethylene glycol with a molecular weight of 550 g/mol (PEG_{550}) (AgPEG NPs) or sodium 11-mercaptoundecanoate ($(CH_2)_{10}$ SH-COONa) (AgCOONa NPs) were provided within the EU FP7 Nanosolutions project (http://www.nanosolutions.eu). For sample preparation and dilution of AgNPs suspension, ultrapure water (UPW; resistivity 18.2 mΩ/cm) was obtained from a Millipore Element apparatus (Millipore, Milford, MA, USA) and used throughout the work. Nitric acid (67-69 %) and hydrochloric acid (34-37 %) of PlasmaPURE quality and single element PlasmaCAL standard of Ag, Au and In (as internal standard) at 1000 µg/mL were obtained from SCP Science (Baie D'Urfé, QC, Canada). For digestions of tissues, nitric acid (65 %) and hydrochloric acid (30 %) supplied by Merck Millipore (Milford, MA, USA) were used. Calibration standard solutions for quantification of Ag in the tissues by conventional ICP-MS were prepared from an Ag stock solution obtained from Merck (Darmstadt, Germany). Triton X-100, used for rinsing the ICP-MS system between each sample, was obtained from Merck (Darmstadt, Germany). As positive control for following the accuracy of SP-ICP-MS measurements over time, 30 nm AgPVP NPs with PVP surface functionalization were obtained from NanoComposix (San Diego, CA, *USA*). According to the provided data sheet, the particle diameter was 30 ± 3 nm (as determined by TEM) and the Ag mass concentration 20 mg/L (as determined by ICP-MS). As positive control for enzymatically and alkaline treated spiked tissue samples, 40 nm NanoXact Silver Nanospheres with PEG surface functionalization were purchased from Nanocomposix (San Diego, CA, *USA*). According to the provided data sheet, the particle diameter was 40 ± 4 nm (as determined by TEM) and the Ag mass concentration 20 mg/L (as determined by ICP-MS). These NPs will be referred to as "AgPEG40 NPs" in the text.

A certified reference material (CRM) for tuna fish (ERM-CE464), obtained by Fluka Chemie GmbH (Buchs, Switzerland), was used for testing the accuracy of the ICP-MS analysis of acid-digested tissues. For the enzymatic digestion of tissue, the commercial protease Proteinase K from Engyodontium album, ReagentPlus sodium dodecyl sulfate (SDS) with ≥ 98.5 % purity, ammonium bicarbonate with 99 % purity and sodium azide with ≥ 98 % purity, all purchased from Sigma-Aldrich (St. Louis, MO, USA), were used. Proteinase K is a serine protease with a molecular mass of 28930 g/mol, a broad pH range

of 7.5-12 and a temperature optimum of 37 °C regarding the enzyme activity. For the alkaline solublization, TMAH (25 % v/v) obtained from Alfa Aesar (Ward Hill, MA, USA) was used.

The perfusion medium (PM) was M199 tissue culture medium (Sigma, St. Louis, MO, USA) diluted 1:2 with Earl's buffer and supplemented with 1 g/L glucose (Sigma, St. Louis, MO, USA), 10 g/L bovine serum albumin (AppliChem GmbH, Darmstadt, Germany), 10 g/L dextran 40 (Sigma, St. Louis, MO, USA), 2500 IU/L sodium heparin (B. Braun Medical AG, Melsungen, Germany), 250 mg/L amoxicillin (GlaxoSmithKline AG, Brentford, UK) and 2.2 g/L sodium bicarbonate (Merck, Darmstadt, Germany).

3.2 Instrumentation

An Agilent 7700x ICP-MS instrument from Agilent Technologies (Tokyo, Japan) equipped with quadrupole mass analyzer was used for the determination of total Ti concentrations after microwave-assisted digestion and for SP-ICP-MS measurements of TiO_2NPs suspensions.

For stabilization of TiO_2NPs during the analytical procedure, different modes of shaking and ultrasonication were applied. Samples were shaken with the use of orbital shaker Vibromix 40 (Tehtnica, Slovenia) operated at 300 rpm and vortex Vibromix 10 (Tehtnica). Ultrasonication was performed using an ultrasonic bath Clifton, SW3H type, Nickel-Electro Ltd. (Weston-super-Mare, United Kingdom), operated at a frequency of 37 kHz, and ultrasonic homogenizer, 4710 series, Cole-Parmer Instrument Co. (Chicago, IL, USA) equipped with 6 mm diameter microprobe. It operated at 10 % power output at frequency of 20 kHz and 50 % pulsed operation mode for 3 minutes. Samples were kept on ice bath during sonication. Ultrasonic homogenizer was applied also for the stabilization of TiO_2NPs during SP-ICP-MS.

A CEM MARS 5 (CEM Corporation, USA) Microwave Acceleration Reaction System equipped with temperature and pressure feedback controls operating at 1600 W was used for digestion of samples.

The zeta potentials of TiO_2NPs in MiliQ water, environmental water samples or aqueous solutions with different dispersing agents were measured as a function of pH by using ZETA PALS Zeta Potential Analyzer (Brookhaven Instruments Corporation, USA). The pH was adjusted by HCl or NaOH and measured by the pH meter (SevenMulti, Mettler Toledo, Switzerland).

The morphology of the TiO_2NPs powders was characterized using a transmission electron microscope (TEM) with an accelerating voltage of 200 kV (Jeol 2100, Tokyo, Japan). Prior to the TEM analysis, the investigated powders were dispersed in EtOH, deposited on a Cu TEM grid and dried in air.

The size distribution of the TiO_2NPs was determined by the DLS technique using Brookhaven NanoBrook OMNI Particle Size Analyzer (Brookhaven Instrument Corporation, NY, USA). Prior to the DLS measurements, suspensions containing 0.2 mg/mL of rutile or 2 mg/mL of anatase were prepared in MilliQ water by the use of ultrasonication. The DLS characteristics of the measured samples were determined by averaging the results of three consecutive measurements (each in 10 runs) obtained for the one diluted working suspension.

SP-ICP-MS measurements of nZVI were performed on an 8800 QQQ ICP-MS instrument from Agilent Technologies (CA, USA), equipped with ASX-500 Series Autosampler. For the pretreatment of the nZVI suspensions prior to the SP-ICP-MS analysis, samples were shaken on the horizontal shaker from Edmund Bühler GmbH, Germany. Concentrations of Na^+, K^+, Ca^{2+} and Mg^{2+} in MilliQ water, synthetic and

effluent wastewater were determined by flame atomic absorption spectrometry, using SpectrAA 110 Atomic absorption spectrometer (Varian, California, USA). Total organic carbon (TOC) content in aqueous samples was measured by a high-temperature catalytic oxidation and infrared detection, using TOC/TN analyzer (Teledyne, Tekmar, CA, USA). pH and conductivity measurements were performed by a WTW pH 3110 (Weilheim, Germany) meter and a Yokogawa SC8221-E (Tokyo, Japan) conductivity meter, respectively.

The AgNPs suspensions were characterized by DLS and laser Doppler velocimetry for determining the hydrodynamic diameter and zeta potential of the NPs (Zetasizer, Malvern Instruments, UK). The measurements were carried out using a dust-free disposable cuvette (DTS0012, Malvern Instruments, UK) for the DLS measurement and a disposable zeta cell (DTS1070, Malvern Instruments, UK) for the zeta potential measurement. The particle size and shape of AgNPs were imaged by transmission electron microscopy (TEM) using a Tecnai G2 T20 instrument (FEI, Eindhoven, The Netherlands) operated at 200 kV accelerating voltage. Ag ions were separated from AgNPs through a 10 kDa filter with the use of a micro centrifuge (Eppendorf MiniSpin, Eppendorf AG, Hamburg, Germany). After the addition of TMAH, tissue homogenate samples were placed into a Branson sonication bath (VWR International, Leicester, UK) at a frequency of 42 kHz and an input power of 185 W. For mixing the homogenized placenta samples with the enzyme solution and for homogenizing the spiked samples, a MS2 minishaker (IKA Works, Inc., Wilmington, NC, USA) was used. The pH value was measured with a PHM 240 pH/ION meter (Radiometer, Copenhagen, Denmark). For enzymatic digestion of the samples, plastic tubes with a round bottom (Karter Scientific Labware Manufacturing, Lake Charles, LA, USA) and a water bath with a HetoHMT 200 RS thermostat and a Telesystem HP15 magnetic stirrer (Holm & Halby, Allerød, Denmark) were used. For digesting the perfusates, a heating oven (Binder GmbH, Tuttlingen, Germany) was used. Tissue samples were digested with acid with the use of a microwave system (turboWave 1500, MWS GmbH, Heerbrugg, Switzerland). The thawed tissue was homogenized using a TissueRuptor (Qiagen, Hombrechtikon, Switzerland).

A Thermo scientific iCAP Q ICP-MS instrument (Thermo Fisher Scientific GmbH, Bremen, Germany) was used for a single particle measurement of the samples from all the perfusion experiments except for the samples from the perfusion experiment 3.4, where Agilent 8800 Triple Quadrupole ICP-MS instrument (Agilent Technologies, California, USA) was applied. Agilent Triple Quadrupole ICP-MS was used also for measuring total Ag concentration of digested and filtrated AgNPs suspensions, as well as digested placenta tissue samples.

A Mettler AE 163 (Mettler Toledo, Zürich, Switzerland) analytical balance was used for all weighting.

3.3 Methods

3.3.1 Sample collection and sample preparation

The stability and dispersion efficiency of TiO_2NPs in two different aqueous matrices were examined in river water and wastewater, spiked with nanoscale anatase and rutile. The Sava River water was collected at Litija (Slovenia) during the first sampling campaign of the EU 7th FW funded GLOBAQUA project [199] in September 2014. Wastewater sample was taken at the effluent of Wastewater Treatment Plant Domžale-Kamnik (Slovenia) in November, 2014. Samples were stored into 1 L polyethylene bottles, immediately transported to the laboratory and kept frozen at – 20 ^{o}C until the analysis.

For sizing and quantification of the TiO_2NPs in environmental waters, the water sample collected from the Sava River was used. Since the river water contained a large amount of suspended particulate matter (62 mg/L), it was filtered through 0.45 µm syringe CE filters (Minisart, Sartorius Stedim Biotech GmbH, Goettingen, Germany) before the analysis in order to prevent the introduction of particulate matter into the ICP-MS system. Known amounts of anatase or rutile were then added to sample aliquots and the sample preparation for the SP-ICP-MS measurements was applied, as described below. In order to check whether TiO_2NPs are retained on the filters, filtration of nanoscale rutile and anatase suspensions was performed through 0.45 µm filters. It was found out that TiO_2NPs were not adsorbed on the filters.

Prior to the SP-ICP-MS analysis, approximately 10 mg of anatase or rutile were dispersed in 50 mL of water and sonicated for 3 min using an ultrasonic homogenizer with a probe. The suspensions were then immediately diluted in several subsequent dilution steps to obtain the final suspensions with a Ti concentration ranging from 0.001 to 1 ng/mL. All the experiments were performed in at least two replicates. This procedure was previously proven to be efficient for dispersing TiO_2NPs in water samples [200]. We have shown that TiO_2NPs can be effectively dispersed in water by combining ultrasonication and different dispersing agents (PEI 600, Darvan C). However, for SP-ICP-MS measurements, dispersions of TiO_2NPs were prepared only in water, since other dispersing agents have different transport efficiencies than aqueous NPs dispersions. Since the microprobe's material of ultrasonic device is made from titanium, its potential contribution to the blank value was tested. 50 mL of MilliQ water was ultrasonicated for three minutes, and TiO_2NPs and dissolved Ti were determined under the same conditions as the investigated samples (same dilution steps and instrumental parameters). The concentrations of the TiO_2NPs and the dissolved Ti determined in the blank were below the LODs, showing that the microprobe does not contribute to the extraneous contamination.

Effluent water sample for nanoremediation experiment with nZVI was collected at the outflow of a small biological wastewater treatment plant (SBWTP) (further called effluent wastewater) with a capacity of 100 population units, located at the village of Hruševo, Slovenia. The water sample was collected into a plastic container and the samples were immediately delivered to the laboratory, where nanoremediation experiments were carried out.

In order to study the influence of increasing Fe loads and different settling times on the behavior of nZVI, 2 L of the effluent wastewater samples were collected into 2 L plastic bottles and treated with different Fe loads (0.1, 0.25, 0.5 and 1.0 g/L). Samples were mixed with a blender at 700 rpm for 4 h and left to settle after different time intervals (0, 0.5, 1, 3, 10, 120 and 168 h). 50 mL of the sample aliquots were taken and decanted into plastic bottles for SP-ICP-MS analysis. To investigate the interactions of nZVI with Cd^{2+} and to evaluate the efficiency of Cd^{2+} removal from different contaminated waters, samples of MilliQ water, synthetic and effluent wastewater were collected into 1 L plastic bottles, spiked with 100 µg/L of Cd^{2+} and treated with 0.25 g/L of nZVI. Bottles were capped and shaken on horizontal shaker at 150 rpm for 4 h. 5 mL sample aliquots were collected after different settling times (0, 0.25, 0.5, 1, 3, 4 and 18 h). Analysis of Fe and Cd in SP-ICP-MS mode were performed under optimized measurement conditions. All experiments were carried out at room temperature (RT) (22 ± 1 °C).

For studying translocation and accumulation of AgNPs in human placenta, placentas were obtained from uncomplicated term pregnancies after caesarean section at the Cantonal Hospital or Klinik Stephanshorn in St. Gallen. Written informed consent was obtained prior to delivery. The project was approved by the local ethics committee and performed in accordance with the principles of the Declaration of Helsinki. The placenta

perfusion experiments were performed on a human *ex vivo* placenta perfusion model at the Swiss Federal Laboratories for Materials Science and Technology (Empa) as described previously [201–203]. Placental perfusion was started by adding 12.48 µg/mL (Ag mass concentration; corresponding to 40 µg/ml AgPEG NPs) of AgPEG (N=3) or 39.26 µg/mL (corresponding to 75 µg/ml AgCOONa NPs) of AgCOONa NPs (N=3) into the maternal circulation. Maternal and fetal perfusates were sampled in duplicate (experimental subsamples) after 0, 1, 3 and 6 h of perfusion. In order to assess possible precipitation of AgCl and formation of particles, perfusion with 1 µg/ml of ionic Ag (N=1) was performed. This concentration was selected as the maximum amount of ionic Ag present in the stock solution of AgNPs. Control perfusion with empty PM (N=1) was also conducted to examine the background levels of Ag. All perfusate samples were immediately delivered to the Technical University of Denmark (DTU) at 4 °C and analyzed by SP-ICP-MS within 3 days. Prior to the SP-ICP-MS analysis, from each experimental subsample of perfusate two (analytical) subsamples were made and were appropriately diluted with UPW in order to detect a sufficient number of particles during each measurement time (at least 400) and to avoid multiple particle events (detecting two or more particles each dwell time). The results for the translocation experiments are expressed as Ag mass concentration in perfusates normalized to the Ag mass concentration (> 25 nm and ≤ 25 nm), measured in the sample on the maternal side at time 0 h (M0) by SP-ICP-MS. This was considered as the starting concentration that was dosed in the perfusion.

In order to investigate the degree of AgNPs accumulation, placental tissue samples from the villous chorion were collected before (0 h) and after each perfusion experiment (after 6 h), frozen and stored for maximum 2 months at -20 °C. The thawed tissue was homogenized by mixing 2 g of tissue in 2 mL of perfusion buffer for 30s (dilution factor of 0.5). Sodium azide at a concentration of 200 mg/L was added to the homogenates to avoid bacterial growth. Homogenates were shipped from Switzerland to Denmark at 4 °C and further stored at -20 °C. To allow double determinations, each homogenate sample was before enzymatic treatment divided into two subsamples. Ag mass concentrations determined in placental tissues, collected before the start of perfusion, were subtracted from the Ag values determined in tissues after 6 h of perfusion. Results are expressed as Ag mass concentrations in the tissues that were normalized to the applied Ag dose, measured in M0 samples by conventional ICP-MS.

3.3.2 Microwave-assisted digestion of TiO_2NPs

Decomposition of TiO_2NPs samples was performed following a two-step microwave-assisted digestion procedure, previously developed in our group for the digestion of sediments [204] with some modifications. 10.0 ± 0.5 mg of anatase or rutile was weighted into 100 mL high-pressure Teflon vessel. Into a vessel 4 mL of HNO_3, 2 mL of HF and 1 mL of HCl were added. The sample was subjected to a closed vessel microwave digestion at a maximal power of 1200 W: ramp to temperature 200 ˚C in 30 min, pressure 50 bar, hold at 200 ˚C for 60 min, cooling 30 min. After that the Teflon vessel was vented and vessel cap removed. 6 mL of H_3BO_3 (4 % aqueous solution) was added to dissolve fluorides and to complex the residual HF. In the second step of the microwave digestion the following programme was applied: ramp to temperature 200 ˚C in 15 min, pressure 50 bar, hold at 200 ˚C for 30 min, cooling 30 min. After digestion, a clear solution was obtained. The content was quantitatively transferred to 100 mL graduated glass or perfluoroalkoxy (PFA) Teflon flask and filled to mark with water. The same procedure, with the exception that no TiO_2NPs sample was added, was applied to determine the blank. Total Ti concentration in the digested sample was determined by ICP-MS. All the experiments were performed in at

least three replicates. Similar procedure for decomposing TiO_2NPs in cosmetic and food products was also used by Cámara et al. [205].

3.3.3 Enzymatic treatment of placental tissues containing AgNPs

A protocol originally developed for AgNPs in lean chicken meat was applied [114]. For the enzyme solution, 3 g/L of Proteinase K and 0.5 % SDS were diluted in the enzyme buffer, consisting of 50 mM ammonium bicarbonate buffer and 200 mg/L sodium azide at pH 7.4. A mass of 0.2 g of tissue homogenate (corresponds to 0.1 g of wet tissue) was weighed into plastic tubes with a round bottom. After the addition of 2.0 mL of the enzyme solution (60 µg of enzyme per mg of wet tissue) and 300 µL of UPW, samples were shortly vortexed until no sample was sticking to the tubes walls. Samples were placed in the water bath at 37 °C and magnetically stirred for 1 hour until they were completely digested. At the end of enzymatic treatment, the samples were placed in ice water to slow down the enzymatic digestion process. All samples were prepared in duplicates.

Prior to SP-ICP-MS measurements, samples were appropriately diluted with UPW. The dilution factor was adjusted until at least 400 particles were detected during one acquisition, to reduce the relative standard deviation (RSTD) of the Poisson distribution to 5 %. At the same time, the number of readings/data points with particle events was limited to 20 % to keep the contribution of multiple particle events to the size distribution below 10 % according to Poisson statistics. All samples were prepared in duplicates.

Since the placental tissue sample, collected before the start of one of the perfusions with AgPEG NPs, shows unexpectedly high Ag mass concentrations and big particle size (probably due to the possible contamination of the sample during sampling, transporting or sample preparation prior to the SP-ICP-MS analysis), the results from this experiment were excluded from the calculations of the mean values for AgPEG NPs.

3.3.4 Alkaline treatment of placental tissues containing AgNPs

A previously developed protocol for AuNPs in rat spleen [105] was modified to be applicable for the treatment of a larger mass of wet tissue (previously 0.020 g) by increasing the TMAH concentration from 5 % to 20 %. Briefly, a mass of 0.2 g of tissue homogenate (corresponding to 0.1 g of wet tissue) was weighted and mixed with 0.3 mL of UPW and 2 mL of TMAH (25 % v/v) to achieve a final concentration of 20 % TMAH. After placing the samples in the sonication bath for 1 hour at RT, they were mixed on the rotator (Ferris wheel) at RT for 23 hours. Prior to SP-ICP-MS measurements, the samples were diluted with UPW 20 times to achieve a TMAH concentration of 1 % (v/v). For further dilutions, a TMAH concentration of 1 % (v/v) was maintained. All samples were prepared in duplicates.

3.3.5 Determination of total Ti concentrations by ICP-MS

Total Ti concentrations after microwave-assisted digestion were determined with the use of ICP-MS (Agilent 7700x from Agilent Technologies). Experimental working conditions for ICP-MS were optimized for plasma robustness and adequate sensitivity and are summarized in Table 3.1.

Table 3.1: ICP-MS operating parameters for determination of total Ti concentrations.

Parameter	**Type/Value**
Sample introduction	
Nebuliser	Teflon MiraMist
Spray chamber	Scott
Skimmer and sampler cone	Ni
Sample depth	7.5 mm
Nebulizer pump	0.1 rps
Plasma conditions	
Forward power	1550 W
Plasma gas flow	15.0 L/min
Carrier gas flow (Ar)	0.98 L/min
Dilution gas flow (Ar)	0.3 L/min
Collision gas flow (He)	4.3 mL/min
Auxiliary gas flow	0.9 L/min
Data acquisition parameters	
Data acquisition mode	Spectrum
Integration time per isotope	500 ms
Isotopes monitored	^{48}Ti, ^{49}Ti
Isotopes of internal standards	^{103}Rh

3.3.6 Determination of total Ag concentrations in perfusates and placental tissues by ICP-MS

The total Ag mass concentrations in the acid digested perfusates and tissues were determined also by conventional ICP-MS analysis. 0.2 mL of perfusates was digested by the addition of 4 mL of HNO_3 (65 %) and 4 mL of HCl (30 %) and by overnight heating at 60 °C in a heating oven. The digests were filled up to 10 mL with UPW. All digestions were performed in duplicate. For testing the accuracy of the digestion procedure and ICP-MS measurements of Ag in perfusates, Ag concentration was determined in PM, spiked with 50 µg of dissolved Ag. Spiked samples were digested in the exact same way as the perfusates and 100.5 ± 0.4 % (N=3) agreement with the expected concentration was achieved.

Placental tissues were digested by adding 2 mL of HNO_3 (65 %) to approximately 0.7 g of tissue, followed by microwave-assisted digestion (12 min heating up to 250 °C, 8 min at 250 °C, cooling down to RT). The digests were filled up to 10 mL with UPW, and to 1 mL aliquot 4 mL of HNO_3 (65 %) and 4 mL of HCl (30 %) were added. The so-prepared samples were left overnight at the RT and filled up to 10 mL with UPW the next day. All digestions were performed in duplicate. For evaluation of the accuracy of the analytical method (digestion procedure + ICP-MS analysis), 250 mg of CRM for tuna fish (ERM-CE464) was spiked with 150 µL of 100 µg/mL ionic Ag solution to a concentration of 60 µg/g. Spiked samples were digested in exactly the same way as the tissues. For spiked CRM, recoveries of 24.9 % ± 9.7 % (N=3) were achieved. Ag concentrations determined in the digested tissue samples were corrected with the average recovery of the spiked CRM samples.

Prior to the quantification of the Ag mass concentration by ICP-MS against an external calibration curve using In as an internal standard, the digests were 5 times diluted with UPW. Calibration standard solutions of Ag were prepared from Ag stock solution and

diluted in 5.2 % HNO_3 and 2.4 % HCl. Experimental conditions for the 7900 ICP-MS instrument are summarised in Table 3.2.

Table 3.2: ICP-MS operating parameters for the determination of total Ag mass concentration in the perfusates and tissues.

Parameter	**Type/Value**
Plasma power	1,550 W
Plasma gas flow rate	15 L/min
Carrier gas flow rate	1.05 L/min
Sample uptake flow rate	0.1 rounds/sec
Isotopes monitored	^{107}Ag, ^{115}In
Integration time per isotope	300 ms
Nebulizer type	MicroMist
Spray chamber type	Scott chamber, Peltier-cooled

3.3.7 DLS measurements of AgNPs

Determination of hydrodynamic size and size distribution of AgNPs in UPW (resistivity 18.2 mΩ/cm), obtained from a Millipore Element apparatus (Millipore, Milford, MA, USA) and PM was performed by DLS (Zetasizer, Malvern Instruments, UK). The measurements were carried out using a dust-free disposable cuvette (DTS0012, Malvern Instruments, UK). The measurement position was fixed at the centre of the cuvette (4.65 mm from the cuvette wall). The detection angle was 173° and the measurement was performed at a temperature of 25 °C, which was achieved following equilibration for 1-2 minutes. Five consecutive measurements were performed using a minimum of 11 runs of 10 s each. The DLS characteristics of the measured samples, given as Z-average (Z_{ave}) and polydispersity index (PDI), were determined by averaging the results of the five repeated measurements (N=5) obtained for the one diluted working suspension.

3.3.8 SP-ICP-MS analyses

3.3.8.1 SP-ICP-MS analysis of TiO_2NPs

For the SP-ICP-MS measurements the data acquisition for the instrument was set to time-resolved-analysis (TRA) mode in order to collect the intensity for a single particle as it is vaporized and ionized in the plasma. The operating parameters which were optimized for plasma robustness and sufficient sensitivity are summarized in Table 3.3.

Table 3.3: ICP-MS operating parameters for quantification and sizing of TiO_2NPs and AgNPs by SP-ICP-MS.

Parameter	**Type/Value**	**Ti**	**Ag**
Sample introduction			
Nebuliser	MicroMist		
Spray chamber	Scott		
Skimmer and sampler cone	Ni		
Sample depth	8 mm		
Nebulizer pump	0.3 rps		
Plasma conditions			
Forward power	1550 W		
Plasma gas flow	15.0 L/min		
Carrier gas flow (Ar)		0.98 L/min	1.05 L/min
Dilution gas flow (Ar)		0.3 L/min	
Makeup gas flow (Ar)			0.1 L/min
Collision gas flow (He)		4.3 mL/min	
Auxiliary gas flow	0.9 L/min		
Data acquisition parameters			
Data acquisition mode	TRA		
Integration time per isotope		3 ms, 5 ms, 10 ms	3 ms
Total acquisition time		30 s, 50 s, 100 s	30 s
Isotopes monitored		^{48}Ti, ^{47}Ti	^{107}Ag

The measurement duration for each run of TiO_2NPs and AgNPs was 100 s, 50 s or 30 s with a short integration dwell time of 10 ms, 5 ms or 3 ms per reading, respectively. The peristaltic pump was set to 0.3 rps for all the experiments, which corresponded to a sample flow rate of 0.996 ± 0.020 mL/min. The average flow rate was determined daily by weighing the amount of UPW aspirated for 1 min. Ti and Ag in standard aqueous solutions were analysed at their most abundant isotopes ^{48}Ti (73.72 %) and ^{107}Ag (51.84 %), respectively. To overcome any possible polyatomic interferences from sulphur and nitrogen [41], the ^{48}Ti isotope was monitored in helium collision mode (4.3 mL/min He gas flow). To demonstrate that the He mode contributes to a lower baseline, a comparison was made between the measurements of the ^{48}Ti isotope in the No gas mode (i.e. measuring without the use of any collision/reaction gas) and the He mode. As expected, a lower sensitivity of the measurement was obtained in the He mode (18.4 counts per µg Ti/L) than in the No gas mode (681 counts per µg Ti/L). However, due to the efficient removal of the polyatomic interferences, a lower baseline was obtained in the He mode, resulting in lower LODs for the dissolved and nanoscale Ti. Therefore, the He mode was chosen for all the experiments in the present study.

Since the ^{48}Ti isotope suffers from isobaric interferences of ^{48}Ca, an element commonly present in high concentrations in environmental waters, the less sensitive ^{47}Ti (7.3 %) isotope was monitored in the river samples. The intensity data (counts per dwell-time interval as a function of time) were recorded using the ICP-MS Mass Hunter software, and exported to an Excel spreadsheet (Microsoft) for further data processing.

The particle size method for the determination of η_{neb} described by Pace et al. was applied [150]. η_{neb} was measured daily with the use of monodispersed AgNPs with known particle sizes and dissolved Ag standards and was found to be 4.7 ± 0.2 %. To check the accuracy of the transport efficiency determined by the AgNPs, the same procedure was also performed with the use of AuNPs. Good agreement between the transport efficiencies determined by the AgNPs (5.3 %) and the AuNPs (5.5 %) was obtained.

3.3.8.2 SP-ICP-MS analysis of nZVI

SP-ICP-MS was used for sizing and quantification of nZVI as well as to differentiate between Cd^{2+} attached to nZVI and dissolved Cd. By measuring Cd in TRA mode at short dwell time, the dissolved Cd in wastewater provided a continuous signal, while Cd^{2+} attached to NPs appeared as the pulses above the continuous background. SP-ICP-MS analyses were performed in MS/MS mode on the 8800 QQQ ICP-MS under the instrumental conditions, presented in Table 3.4.

Table 3.4: ICP-MS instrumental parameters for single particle analysis of nZVI.

Parameter	**Value/Type**	
Sample introduction		
Nebuliser	MicroMist	
Spray chamber	Scott	
Skimmer and sampler cone	Ni	
Sample depth	8 mm	
Sample uptake flow rate	0.300 - 0.330 mL/min [a]	
Plasma conditions		
Forward power	1550 W	
Plasma gas flow	15.0 L/min	
Carrier gas flow (Ar)	1.09 L/min	
Auxiliary gas flow	0.90 L/min	
Cell parameters		
Cell gas flow rate	5.0 mL/min H_2	/
Octopole bias (V)	-18.0	-8.0
Octopole RF (V)	200	130
KED (V)	-8.0	5.0
Data acquisition parameters		
Data acquisition mode	Time resolved analysis	
Integration time per isotope	3 ms	
Total acquisition time	60 s - 180 s	60 s
Isotopes monitored	^{56}Fe	^{111}Cd

[a]Determined on daily basis (corresponding peristaltic pump speed was 0.1 rps)

The operating parameters were optimized for plasma robustness and sufficient sensitivity of monitored isotopes. Fe was measured at m/z 56, at the most abundant Fe isotope (91.75 %). To overcome possible polyatomic interferences on m/z 56 ($^{40}Ar^{16}O^+$, $^{40}Ca^{16}O^+$), H_2 which interacted with the interfering ions, was introduced as a reaction gas (5.0 mL/min). For Cd measurements, ^{111}Cd isotope (12.80 %), which is interference free, was chosen. ^{56}Fe and ^{111}Cd isotopes were detected in TRA mode using 3 ms dwell time for a total measurement time of 60 – 180 s which corresponds to the 20,000 – 60,000 data points per isotope. Since quadrupole is not capable of detecting more than one isotope simultaneously at the required high data collection rates (milliseconds dwell time), Cd isotope was monitored in a separate run. Moreover, simultaneous monitoring of Cd and Fe was also not possible due to the significantly different concentrations of both elements in the samples analysed. Prior to SP-ICP-MS analysis suspensions were shaken on a horizontal shaker at 300 rpm for 3 minutes to ensure homogenous dispersions of NPs. Samples were not filtered since we have demonstrated that the filtration (0.45 μm) retained about 70 % of nZVI. Suspensions of nZVI were appropriately diluted with MilliQ water in order to detect a sufficient number of particles during each measurement time (at least 500) and to avoid multiple particle events (detecting two or more particles each dwell time). To prevent the adsorption of nZVI on the ICP-MS tubing and to eliminate the memory effect, rinsing

with 1 % (v/v) HNO_3 was applied for 60 s, followed by rinsing with MilliQ water for 90 s at a flow rate of approximately 0.3 mL/min. Before the sample analysis, MilliQ water was analyzed to check whether the carryover effect was removed.

The transport efficiency of the liquid samples through the sample introduction system was determined according to the "particle size" method, described by Pace et al. [150]. It was found to be 6.44 ± 0.57 %. Accurate sample flow rate (0.1 rps) was daily determined by weighing water aspirated into the plasma for 2 min. Data processing for SP-ICP-MS was performed according to the methodology described by Pace et al. [150] using a spread sheet routine in Microsoft Excel (Microsoft, WA, USA). Quantification of particulate Fe and Cd^{2+} adsorbed on nZVI, performed by summing up the pulse intensity of the recorded particles [168], was based on the relevant calibration curves constructed from blank (MilliQ water) and standard solution of dissolved Fe and Cd, respectively. The same calibration curve for Fe was used also for the quantification of nZVI size.

One of the difficulties in the SP-ICP-MS analysis is discrimination between the background signal (i.e. instrumental noise, dissolved analyte) and particulate signal. In our study, the threshold for all the samples was set to a value which gives a particle size distribution with a minimum particle diameter corresponding to the determined size detection limit (LOD_{size}). The LOD_{size} was established according to Eq. (5) by converting the counts that correspond to 3 times the standard deviation of the blank (σ_{MQ}) (MilliQ water, N=4), into the diameter, where particle density (ρ), mass fraction of Fe in nZVI (f_a) and the Fe sensitivity (R in cps/µg) were taken into account [166].

$$\mathrm{LOD_{size}} = \left(\frac{6 \times 3\sigma_{\mathrm{MQ}}}{\mathrm{R} \times \mathrm{f_a} \times \rho \times \pi} \right)^{1/3} \quad (5)$$

This approach ensured that a defined size fraction of nZVI (i.e., above LOD_{size}) was considered in the data analysis, making a direct comparison of particle mass concentration between differently diluted samples and different sample matrices possible [105]. The limit of detection for NPs mass concentration (LOD_{NP}) was determined by the measurement of at least 6 blank samples (MilliQ water) before and between actual samples as the average ± 3 times the STD of the blank signal and transformed to the particle mass concentration. When measuring Cd in single particle mode, particle events were distinguished from the background by applying an iterative algorithm where intensity, higher than 4 times the STD of the whole data set, was regarded as particle signal.

In order to test if any Fe or Cd in the particulate or dissolved form is naturally present in MilliQ water, synthetic or effluent wastewater, the relevant matrices were diluted in the same way as the real samples and measured by SP-ICP-MS. Only in the effluent wastewater a low amount of Fe (i.e. 160 µg/L), compared to the concentration of nZVI added into wastewater during nanoremediation, was detected. This value was subtracted from the Fe concentrations determined in effluent wastewater that was treated with nZVI.

3.3.8.3 SP-ICP-MS analysis of AgNPs

Data processing was performed according to the methodology described by Pace et al. [150], using a spread sheet routine. Accurate sample flow rate (0.1 rps) was determined daily by weighing. Quantification of particle size (particle diameter) was based on a calibration curve constructed from a blank (UPW) and four concentration levels of certified standard solutions of Ag ranging from 0.2 to 2.0 ng/mL. The isotope ^{107}Ag was detected using 3 ms dwell time for a total measurement time of 180-600 s (equivalent to 60,000-

200,000 data points). The ICP-MS signal intensity for each standard solution was acquired by averaging the signal intensity recorded during this measurement time.

Instrument tuning was performed prior to analysis by using a tuning solution according to the manufacturer's recommendation. Settings for Thermo scientific iCAP Q and Agilent 8800 Triple Quadrupole ICP-MS instruments are given in Table 3.5.

Table 3.5: ICP-MS settings for single particle analysis of AgNPs.

Parameter/ICP-MS type	**Thermo Fischer iCAP Q**	**Agilent 8800 Triple Quadrupole**
Plasma power	1,550 W	
Plasma gas flow rate	15 L/min	
Carrier gas flow rate	1.03 mL/min	1.05 mL/min
Sample uptake flow rate	0.30 – 0.33 mL/min[a]	
Isotopes monitored	^{107}Ag	
Integration time per isotope	3 ms	
Analysis time	180-600 s	
Nebulizer type	MicroFlow PFA	MicroMist
Spray chamber type	Quartz cyclonic type, Peltier- cooled	PFA Scott chamber, Peltier-cooled

[a]Determined on a daily basis (corresponding peristaltic pump speed was 0.1 rounds/sec).

In order to follow the precision and accuracy of SP-ICP-MS measurements, median particle diameter and particle mass concentration of AgPVP NPs standard prepared at 20 ng/L concentration were determined and compared with the values provided by supplier each time the samples from perfusion experiments were measured. The PVP-stabilized AgNPs were used as standard particles with a size that was as low as possible to still be well detectable by SP-ICP-MS (i.e. 30 nm). Determination of AgPVP median particle size by SP-ICP-MS was repeatable and reproducible (ANOVA, $p < 0.01$) and agreed well with the size provided by the supplier (average determined size was 25.9 nm).

The recorded signal intensity data were plotted (in cps) versus the number of "events" to create a signal distribution histogram using Microsoft Excel (Microsoft, WA, USA). Low, stable and relatively noise-free signal intensities were considered to be caused by instrument background and for slightly higher intensity values, caused by dissolved Ag. The threshold between signals from instrumental noise/dissolved Ag and particulate Ag was set to a value which gives a particle size distribution with a minimum particle diameter of 25 nm. This value corresponds to the lowest detectable diameter, determined in the samples from the maternal side. Although the lowest detectable diameter determined in the samples from the fetal side was lower (14 nm), the higher value was chosen. The approach of setting a fixed detection limit for particle size ensured that a defined size fraction of AgNPs (i.e., above 25 nm) was considered in the data analysis, making a direct comparison of particle mass and number concentration between differently diluted samples possible. The same size threshold (i.e. 25 nm) was applied also for distinguishing particle events from the instrumental background and ionic Ag signal for the AgPEG40 control particles. When measuring the AgPVP standard, particle events and the background were distinguished by applying an iterative algorithm where the measured intensity, higher than 6 times the STD of the whole data set, was regarded as particle signal.

The transport efficiency was determined according to the "particle frequency" and "particle size" method [150]. For determination of the transport efficiency based on the "particle frequency" method, a reference AuNP suspension with a known average particle diameter of 27.6 nm (based on measurements by transmission electron microscopy provided by NIST) and a gold mass concentration of 48.17 ± 0.33 µg/g (information value provided

by NIST), diluted 10^7 times with UPW was analyzed. The transport efficiency was calculated as the percentage of all AuNPs detected by SP-ICP-MS versus the theoretical (calculated) particle number in the introduced sample volume [105]. The transport efficiency according to the "particle size" method was determined in the following way: First, a calibration curve that related ^{197}Au signal intensity (peak maximum of the intensity distribution) to particle mass was created using the reference AuNPs (particle mass 0.212 fg) in UPW. Second, a corresponding calibration curve was constructed by determining the average ^{197}Au signal intensity for ionic Au standards at 0, 0.2, 0.5 and 1.0 µg/L. The Au concentration was converted to Au mass by multiplication with the sample flow rate and dwell time. The transport efficiency was determined by dividing the slope from the calibration curve made from the ionic Au standards by the slope from the calibration curve created from the AuNPs.

To prevent AgNPs from sticking on the ICP-MS tubes and to avoid the memory effect during the ICP-MS measurement, the following washing procedure was applied between each sample: the ICP-MS system was first rinsed with a mixture of 1 % (v/v) HCl (34-37 %), 1 % (v/v) HNO_3 (67-69 %), and 0.1 % (m/v) Triton X-100 for 1 min at 1.5 mL/min, followed by rinsing with UPW for 30 s at 0.3 rpm. Following the analysis of each sample, UPW was analyzed to ensure that no carryover from the previous measurement was detected.

Results based on repeated measurements are given as mean ± 1 STD. The number of repetitions N is stated in parentheses. Data (i.e. comparison of PSD over different perfusion times, repeatability and reproducibility for sizing and quantification of AgNPs) were statistically analyzed by using one-way Analysis of variance (ANOVA) in Microsoft Office Excel 2010 (Microsoft, Redmond, WA, USA). A p-value ≤ 0.01 was considered statistically significant.

Chapter 4

Results and Discussion

4.1 Optimization of the Procedure for Efficient Dispersion of Titanium Dioxide Nanoparticles in Aqueous Samples

4.1.1 Determination of total Ti concentrations in TiO_2NPs by ICP-MS

Determination of total Ti concentrations in TiO_2NPs is used not only for its quantification, but also for the evaluation of efficiency of TiO_2NPs dispersion by the use of different approaches for stabilization of NPs in suspensions. For this purpose, effective sample digestion of refractory TiO_2NPs is necessary prior to the determination of total Ti concentration by ICP-MS. In order to decompose TiO_2NPs rapid digestion procedure by the use of ammonium persulfate as a fusing reagent with reported good recoveries [98] was first applied. Ti concentration in the sample digest was immediately determined by ICP-MS. To avoid possible polyatomic interferences from sulphur and nitrogen compounds arising from ammonium persulfate (e.g. $^{32}S^{16}O^+$, $^{34}S^{14}N^+$) [41], the ^{49}Ti isotope (5.46 %) was monitored instead of the ^{48}Ti isotope (73.98 %) in helium collision mode (4.3 mL/min He gas flow). The recoveries between the determined and added Ti concentration in TiO_2NPs were less than 60 % with poor repeatability (50 %) of the analytical procedure and were most probably related to inefficient digestion of the samples, non-quantitative transfer of suspensions after the digestion and difficulties in effective cleaning of the beakers in which the digestion was performed.

To achieve quantitative recoveries with acceptable repeatability, microwave-assisted digestion was then applied. Since no certified reference material for TiO_2NPs exists, the method for microwave-assisted digestion was validated by spike recovery test using commercially available nanoscale rutile and anatase. The slightly modified procedure previously developed in our group [204], as described in paragraph 3.3.2., was used to digest anatase and rutile samples. In the optimization of the two-step digestion process, a mixture of HNO_3, HF and HCl was first added, followed by the addition of various amounts of 4 % H_3BO_3 (6, 9 or 12.5 mL). The addition of H_3BO_3 is mandatory to complex the residual HF in order to prevent the reaction of HF with the quartz part of the ICP-MS. Digested samples were transferred into 100 mL glass bottles and stored at 4 °C. The total Ti concentration was determined after 1, 2, 10 and 30 days by ICP-MS (monitoring ^{48}Ti isotope). Prior to Ti determination by ICP-MS, samples were appropriately diluted with water. The results expressed as recoveries between the determined and added Ti concentrations are presented in Figure 4.1.

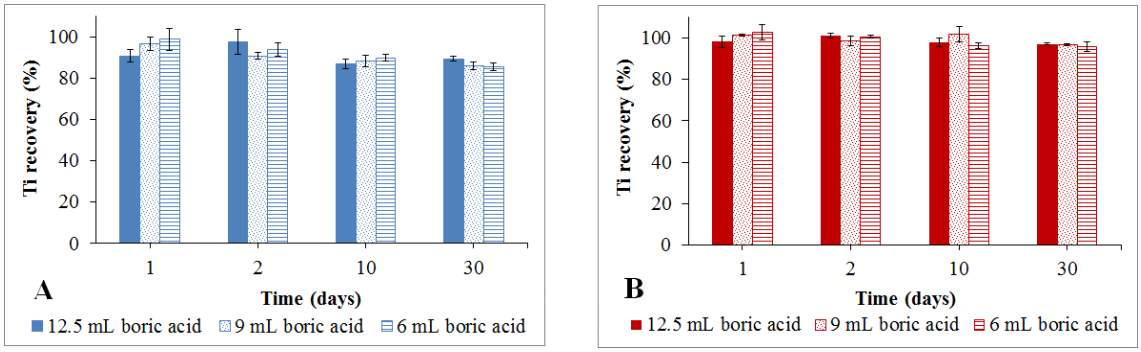


Figure 4.1: The efficiency of a two-step microwave-assisted digestion of nanoscale anatase (A) and rutile (B) using a mixture of 4 mL nitric acid, 2 mL hydrofluoric acid and 1 mL hydrochloric acid (first step) and various amounts of 4 % boric acid (second step). Results represent the average ± STD of three replicates.

From the data of Figure 4.1 it is evident that one day after the digestion the recoveries between determined and added Ti in anatase and rutile in general lied between 97 and 102 %, which indicates an efficient sample decomposition. The recoveries around 100 % were observed for rutile in samples measured 30 days after the digestion, while for anatase the recoveries for Ti gradually decreased with time and were 30 days after the digestion between 85 and 90 %. The slight losses of Ti in digested anatase solution are most likely related to the adsorption of Ti ions on the negatively charged glass surfaces [206] despite low pH (< 1) of samples. No decrease in Ti concentration over time is observed for digested nanoscale rutile. Namely, since rutile contains 5 wt. % SiO_2 as a surface coating, Si ions are also released into the solution during the digestion procedure and are adsorbed on the glass surface, hindering Ti ions adsorption. In order to prevent the possibility of Ti ions adsorption on glass surface, in the following experiments Teflon laboratory ware was applied. The same experiments as shown in Figure 4.1 were repeated for digested samples stored in Teflon. The data revealed that the recoveries for anatase and rutile were around 100 %, even 30 days after the digestion, when stored in Teflon. In contrast to the hydrophilic glass surface with the negative charge, Teflon (polytetrafluoroethylene) as a hydrophobic polymer does not adsorb Ti ions [207]. Data from the above experiments demonstrated that the amount of 4 % H_3BO_3 added in the second step of the digestion procedure did not have a significant influence on the efficiency of anatase and rutile decomposition. Therefore, to minimize the consumption of acids, 6 mL of 4 % H_3BO_3 was further applied and Teflon laboratory ware used in the following experiments. The limit of detection (LOD) and quantification (LOQ) for the determination of Ti in nanoscale anatase and rutile by ICP-MS after microwave-assisted digestion were calculated on the basis of three times and 10 times the STD of the signal of nine blank samples analysed, respectively. Low LOD (0.086 ng Ti/mL) and LOQ (0.287 ng Ti/mL) were obtained. The linearity of measurement for Ti in nanoscale anatase and rutile by ICP-MS was obtained over the concentration range from LOQ to 100 ng Ti/mL.

4.1.2 Determination of total Ti concentrations in aqueous solutions of TiO_2NPs by ICP-MS

In order to demonstrate the applicability of the optimized microwave-assisted digestion for decomposition of TiO_2NPs in aqueous solutions, 10 mg of anatase or rutile were weighed into a Teflon vessel and 20 mL of water was added. The microwave-assisted digestion procedure and sample manipulation was performed as described before. For comparison of

analytical data, powdered nanoscale TiO_2 without the addition of water was analysed under the same analytical procedure. Results of these experiments are presented in Table 4.1.

Table 4.1: Recoveries between the determined and expected Ti concentrations in nanoscale anatase and rutile samples after a two-step microwave-assisted digestion. A mixture of 4 mL HNO_3, 2 mL HF and 1 mL HCl in the first step and 6 mL of 4 % boric acid in the second step were added to (A) 10 mg of sample and (B) 10 mg of sample + 20 mL of water. Concentration of Ti was determined by ICP-MS immediately after the digestion.

Sample		Recovery (%)	Average (%)	RSD (%)
Anatase	A	95.2 101.5 97.3	98.0	3.2
	B	98.2 98.0 101.2	99.1	1.8
Rutile	A	97.6 101.3 104.5	101.1	3.5
	B	100.7 99.9 99.9	100.2	0.4

Data from Table 4.1 demonstrate that the recoveries between the determined and added Ti concentrations lie between 98 and 101 % for nanoscale anatase and rutile when powdered samples were digested as well as when 20 mL of water was added to powdered samples before the digestion. Good repeatability of results between three replicates with RSTD ± 3.5 % was obtained. This extends the applicability of the analytical procedure for the quantification of nanoscale Ti in environmental waters as well as in other aqueous matrices. For instance, the same digestion procedure was successfully applied for estimating possible migration of TiO_2NPs from non-stick food contact coatings (e.g. frying pans) into food [208]. Migration tests into simulants (deionized water, 3 % acetic acid and 5 g/L citric acid) were performed (2 h at 100 °C), and thermal and mechanical degradation of the matrix was studied. Concentrations of TiO_2NPs in simulants were determined by ICP-MS after microwave-assisted digestion and were up to 861 µg/L (147 µg/dm).

4.1.3 Stabilization of TiO_2NPs in aqueous solutions

In sizing and quantification of nanoscale Ti it is of crucial importance to maintain efficient dispersion of NPs in solution throughout the analytical procedure. Aggregates of NPs can be separated by introducing the mechanical force or by overcoming weak attractive forces by electrostatic, steric or electrosteric interaction with the addition of dispersing agents that adsorb on the surface of particles, suppressing their aggregation [209]. In the present work, among pretreatment methods available for dispersing of NPs, different mechanical and ultrasonication procedures in combination with various dispersing agents were tested. As dispersing agents 0.5 wt % cationic polymer PEI 600 (polyethylenimine), 1 wt % anionic dispersant Darvan C (ammonium polymethacrylate) and 1 wt % non-ionic surfactant Triton X-100 (with hydrophilic polyethyleneoxide chain and hydrophobic aromatic hydrocarbonlipophilic group) were used. First, mechanical shaking (horizontal shaker) in combination with vortex and/or ultrasonic agitation (ultrasonic bath) was applied to aqueous suspension of nanoscale anatase and rutile at different time intervals from 5 to 60

min (mechanical shaking), 0.5 to 1 min (vortex) and 5 to 30 min (ultrasonic bath). The same sample treatments were used for TiO_2NPs samples dispersed in PEI 600, Darvan C and Triton X-100. After treatment, suspensions were appropriately diluted and 10 mL aliquots transferred into Teflon vessels. Microwave-assisted digestion procedure was applied and concentrations of Ti in digested sample determined by ICP-MS. The recoveries from 70 to 100 % with poor repeatability (RSD ± 30 %) were obtained. Lower recoveries are most probably related to the ineffective mechanical shaking of NPs. For improving the dispersing efficiency, ultrasonic homogeniser with probe (referred to as ultrasonication) was then used for preparation of suspensions of TiO_2NPs in water or in different dispersing agents.

In order to test if ultrasonication disperses TiO_2NPs more efficiently in aqueous solution than mechanical shaking, vortex or ultrasonic bath, 50 mL dispersions of rutile were prepared by applying 3 min of ultrasonication in water and using the same dispersing agents. After ultrasonication 10 mL sample aliquots were immediately transferred into Teflon vessels and microwave-assisted digestion was applied. Ti concentrations in digested samples were determined by ICP-MS. The recoveries between the determined and expected Ti concentration are presented in Figure 4.2.

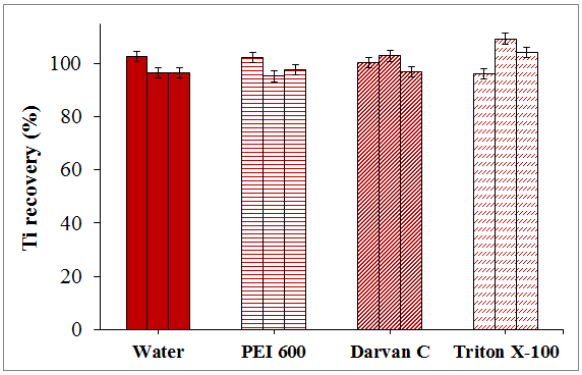


Figure 4.2: The efficiency of dispersion of nanoscale rutile in MilliQ water, using ultrasonication and different dispersing agents. Each bar represents one replicate, while error bars represent the STD of Ti measurement by ICP-MS.

As can be seen from Figure 4.2, the use of ultrasonication or ultrasonication with different dispersing agents efficiently disperses the nanoscale rutile in suspensions, enabling their quantitative transfer into Teflon vessels. Good recoveries ranging from 95 to 105 % were obtained. STD between three replicates for nanoscale rutile dispersed in water, PEI 600, Darvan C and Triton X-100 were ± 3.6 %, ± 3.5 %, ± 3.0 % and ± 6.6 %, respectively. Slightly worse repeatability using Triton X-100 for dispersion is presumably related to high viscosity of this dispersing agent and to the weaker adsorption of non-ionic Triton X-100 on the charged surfaces of TiO_2NPs in comparison to the cationic PEI 600 and anionic Darvan C. The latest two surfactants are more strongly bound to the NPs surface due to the presence of ionic groups, resulting in more efficient stabilization of NPs.

To additionally verify the stability of TiO_2NPs dispersions, zeta potential was measured in a wide pH range. pH is an important parameter for controlling the NPs stability, since it affects the surface charge and particle interactions. Aggregation and sedimentation of NPs in general increases as the pH approaches to the point of zero charge – isoelectric point (IEP). The region of low suspension stability typically appears at zeta potential values from –30 to +30 mV, whereas at zeta potentials higher than +30 or lower than –30 mV NPs remain dispersed in suspensions [210]. As the most efficient approach

for dispersing TiO_2NPs in solution, ultrasonication in combination with different dispersing agents was applied in the following experiments. The adsorption of surfactants on the NPs surface causes changes of its properties, which results in changing their zeta potential [211]. Zeta potentials of nanoscale rutile dispersed by ultrasonication in water, PEI 600, Darvan C or Triton X-100 are presented as a function of pH in Figure 4.3.

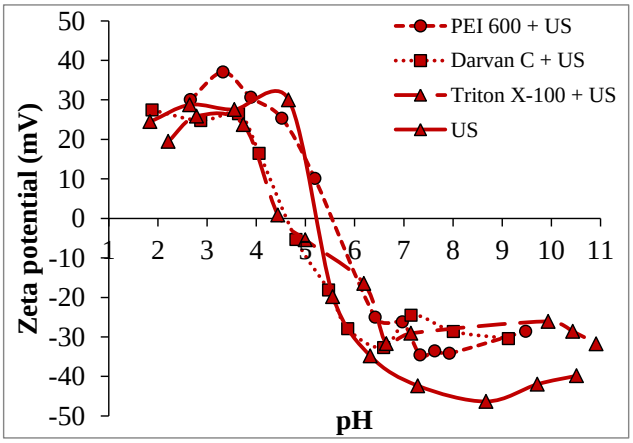


Figure 4.3: Zeta potentials of nanoscale rutile in MilliQ water dispersed by ultrasonication (US) and the use of different dispersing agents as a function of pH.

From Figure 4.3 it can be seen that rutile dispersed in water has IEP at pH 5.3. As expected, PEI 600 slightly shifted IEP toward higher pH (5.6), while Darvan C and Triton X-100 shifted IEP toward a lower pH (4.5). NPs are generally stabilized by the adsorption of a dispersant (polyelectrolyte) layer around the particle surface. Positive charge allows PEI to complex with negatively charged TiO_2NPs, shifting IEP towards higher pH. On the other hand, ammonium salt of polymethacrylic acid (Darvan C) changes the surface charge of TiO_2NPs to a more negative value, increasing the electrostatic repulsion between the particles and shifting IEP towards lower pH [212]. The same observation can be seen for rutile NPs dispersed in Triton X-100, where hydrophobic chains are adsorbed onto the NPs surfaces, while the hydrophilic ethylene oxide chains repulse each other, causing the stabilization of NPs in suspension [213].

Results presented in Figure 4.3 indicate that stability of nanoscale rutile dispersed in water, PEI 600, Darvan C or Triton X-100 is similar in acidic pHs, but is higher in alkaline pHs for NPs dispersed only in water. Lower zeta potentials of TiO_2NPs dispersed in surfactants are most probably related to the formation of surfactants aggregates on the NPs surface due to the hydrophobic interactions between nonpolar chains of the surfactants. In our experiments, the concentrations of surfactants were significantly lower than their critical micelle concentrations, which leads to the formation of surfactant aggregates [213, 214]. These aggregates destabilize NPs in suspension and decrease zeta potential. At the pH of nanoscale rutile suspensions (pH 6.5) zeta potentials for NPs dispersed in water, PEI 600, Darvan C or Triton X-100 were – 38.0, – 25.0, – 32.7 and – 32.4 mV, respectively. It can be concluded that the applied dispersing agents do not improve the stability of TiO_2NPs in aqueous suspensions. Efficient dispersion of NPs in MilliQ water was already achieved by the use of ultrasonication.

4.1.4 Stability of TiO_2NPs in environmental water samples

The sample matrix of environmental waters (e.g. concentration of NOM, ionic strength) may have a significant influence on the stability of TiO_2NPs and on the determination of Ti concentrations by ICP-MS. Since concentrations of TiO_2NPs in environmental waters were low, spiking of river and wastewater samples was performed. The relevant characteristics of river and wastewater studied are presented in Table 4.2.

Table 4.2: Selected parameters for river and wastewater samples.

Parameter/ Sample	**pH**	**Conductivity (µS/cm)**	**TOC (mg/L)**	**Ca^{2+} (mg/L)**
River water	7.8	279 ± 2	3.0 ± 0.2	38 ± 1
Wastewater	7.9	854 ± 5	30 ± 2	68 ± 1

As evident, the investigated samples have a pH close to 8. Since NOM may enhance the stability of NPs, TOC which in general originates from decomposition of NOM was measured in river and wastewater samples. TOC was 3.0 ± 0.2 mg/L in river water and ten times higher in wastewater, while electrical conductivity, which is related to the ionic strength, was found to be 279 µS/cm and 854 µS/cm for river and wastewater, respectively. Ca is one of the major cations, which was present in river (38 mg/L) and wastewater (68 mg/L) and importantly contributed to the ionic strength of samples investigated [215]. High Ca content may provoke NPs aggregation, and causes severe isobaric interference on the determination of Ti at *m/z* 48. To avoid this type of interference, Ti concentrations in digested samples were measured at *m/z* 49, while He mode was applied to compensate for possible polyatomic interferences.

In order to evaluate the influence of sample matrix on dispersion efficiency of TiO_2NPs, 50 mL of river and wastewater samples were spiked with 10 mg of nanoscale rutile or anatase, appropriately diluted and 10 mL aliquots transferred into Teflon vessels. During each dilution step, ultrasonication of the suspensions was applied. Ti concentrations originally present in river and wastewater, and in sample aliquots spiked with TiO_2NPs, were determined by ICP-MS after microwave-assisted digestion. The recoveries between the determined and expected Ti concentrations are presented in Table 4.3.

Table 4.3: Determination of Ti concentration in river and wastewater samples and the recoveries between the determined and expected Ti concentrations in water samples spiked with TiO_2NPs (anatase and rutile) after a two-step microwave-assisted digestion. Results represent the mean value of three replicates ± STD of measurements.

Sample	**Ti conc (ng/mL)**	**Crystalline phase of TiO_2NPs added**	**Ti conc in TiO_2NPs added (ng/mL)**	**Ti conc expected (ng/mL)**	**Ti conc determined (ng/mL)**	**Recovery (%)**
River water	74 ± 4	Rutile	161 ± 3	235 ± 4	160 ± 9	68
		Anatase	162 ± 1	236 ± 4	174 ± 12	74
Waste water	2.7 ± 0.1	Rutile	155 ± 13	158 ± 10	81 ± 5	51
		Anatase	178 ± 4	181 ± 5	118 ± 7	65

As can be seen, the recoveries for anatase and rutile dispersed in river and wastewater samples by the use of ultrasonication are significantly lower (ranging from 51 to 74 %) in comparison to quantitative recoveries for rutile dispersed in MilliQ water (Figure 4.2, first three columns). Poor recoveries are related to aggregation of TiO_2NPs in samples

investigated, which prevents the quantitative transfer of NPs suspensions. Due to higher ionic strength of wastewater, the extent of TiO_2NPs aggregation was higher than in river water. The stability of NPs in environmental samples is influenced also by the presence of NOM [216] that increases electrostatic and steric repulsions and thus stabilizing NPs [210]. Despite higher concentration of NOM in wastewater, the impact of high ionic strength on NPs stability prevailed, which resulted in lower recoveries of digested wastewater samples. Since ultrasonication is not efficient enough to break up aggregates, surfactants need to be used to keep particles stable in suspension.
To verify whether the stability of nanoscale anatase and rutile in river and wastewater samples can be improved by the use of dispersing agents, zeta potentials of TiO_2NPs in spiked water samples and spiked water samples with the addition of dispersing agents were measured and are presented in Figure 4.4.

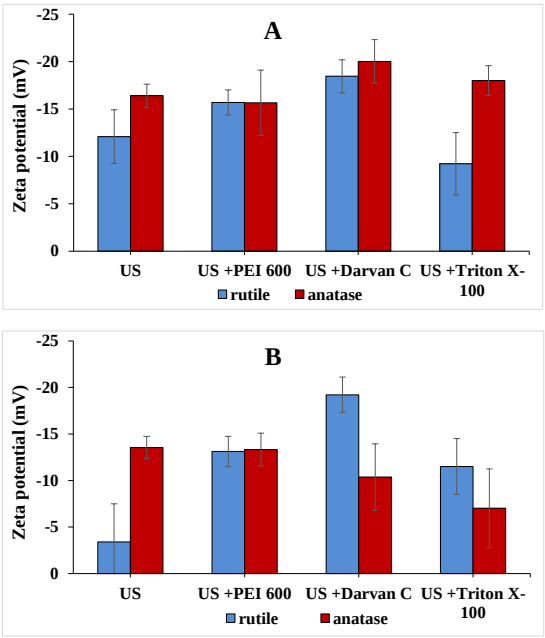


Figure 4.4: Zeta potentials of river water (A) and wastewater (B), spiked with nanoscale anatase and rutile. Samples were dispersed by ultrasonication (US) and by the use of US in combination with different dispersing agents. Results represent the mean value of ten replicates with the STD of the measurements.

From the results in Figure 4.4 it can be seen that zeta potential for nanoscale rutile and anatase dispersed in river and wastewater samples did not exceed the absolute value of 20 mV, indicating that NPs are unstable in dispersions. This is related to the presence of high concentration of cations that are adsorbed on the particles surface, neutralizing their charge, which leads to smaller electrostatic repulsions between NPs. This effect is more pronounced in wastewater due to the higher ionic strength and for rutile due to higher specific surface area (according to the manufacturer data, specific surface area of rutile and anatase is 130-190 m^2/g and 45-55 m^2/g, respectively) [217]. Rutile NPs with higher surface area bind cations more effectively. This decreases the stability of NPs and reduces the zeta potentials. Higher degree of aggregation for rutile dispersed in river and wastewater in comparison to anatase is in accordance with lower Ti recoveries of digested rutile samples (Table 4.3). From Figure 4.4 it is further evident that the use of dispersing agents in combination with ultrasonication does not significantly improve the dispersion efficiency in river or wastewater samples (low zeta potentials), demonstrating the strong influence of matrix constituents on the stability of TiO_2NPs in environmental waters.

The results presented in the chapter 4.1 are based on the data of the published article [200].

4.2 Sizing and Simultaneous Quantification of Nanoscale Titanium Dioxide and a Dissolved Titanium Form by Single Particle Inductively Coupled Plasma Mass Spectrometry

4.2.1 Size and size distribution of TiO_2NPs determined by TEM and DLS

In order to determine the size of two commercial TiO_2NPs powders, TEM images of nanoscale anatase and rutile were measured and are presented in Figure 4.5.

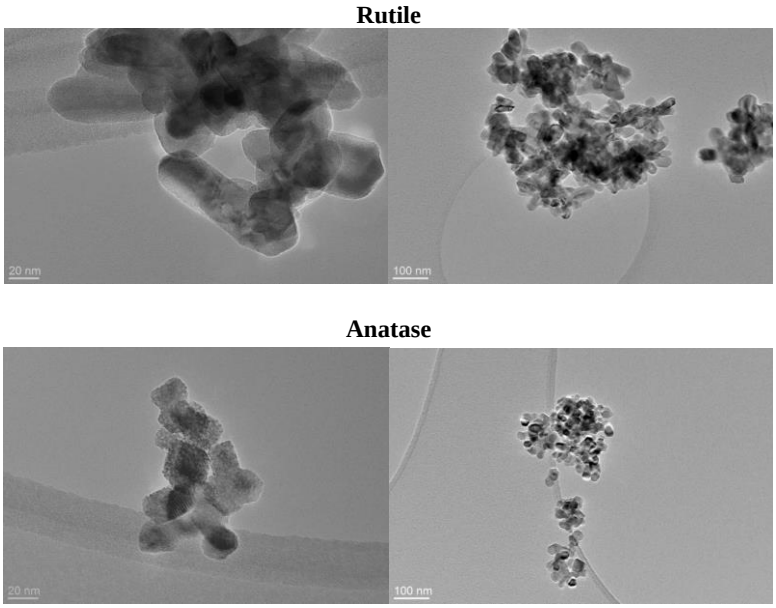


Figure 4.5: TEM images of TiO_2NPs in rutile and anatase crystalline phases, which were taken at magnifications of 100k (left-hand images) and 25k (right-hand images).

The primary particles of rod-shaped rutile observed in the TEM images have diameters between 24 and 30 nm and lengths between 96 and 106 nm (left-hand image). Observed is also the formation of aggregates larger than 160 nm (right-hand image). The primary particle size of spherical nanoscale anatase is between 21 and 38 nm (left-hand image) with aggregates larger than 100 nm (right image). The particle sizes of the rutile NPs determined by TEM are larger than those reported by the manufacturers (10 nm in diameter and 40 nm in length), which could be attributed to the NPs aggregation during storage.

The sizes and size distributions of the nanoscale rutile and anatase in aqueous solutions were further examined using the dynamic light scattering (DLS) method (Figure 4.6).

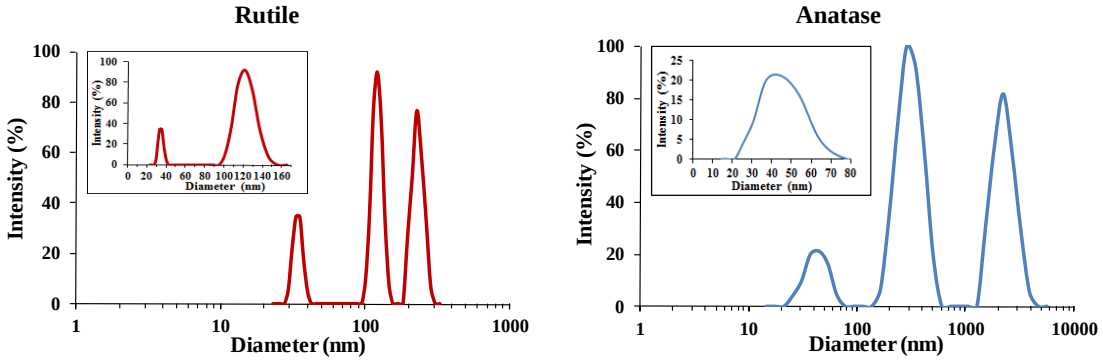


Figure 4.6: DLS hydrodynamic size measurements (intensity-based distributions) of TiO_2NPs in rutile and anatase crystalline phases. Results represent the average of three consecutive measurements corresponding to one stock suspension prepared by ultrasonication.

The data from the DLS measurements were expressed as the average diameter for the size, and the full-width-at-half maximum for the size distribution. The DLS measurements indicate that the nanoscale rutile dispersed in water using ultrasonication has average diameters of 33 ± 6 nm and 117 ± 22 nm, and aggregates with diameters larger than 170 nm. For nanoscale anatase the size distribution with an average diameter of 42 ± 30 nm was determined. Considerable aggregation also occurred, which was evident from two larger peaks (100 to 300 nm and 1000 to 3000 nm). The data on the size and the size distributions of the nanoscale rutile and anatase obtained by DLS are in good agreement with the sizes determined by TEM.

4.2.2 Determination of TiO_2NPs size and size distribution by SP-ICP-MS

Since no suitable reference materials of TiO_2NPs in monodispersed form with well-characterized size exist, for TiO_2NPs sizing, dissolved Ti standards were used to prepare a calibration curve by plotting the mass concentration versus the signal intensity of the dissolved Ti solutions. The procedure applied in our study is well-known and widely used by numerous researchers for different NPs types [144, 148, 150, 168].

To obtain a time scan, a solution of dissolved ^{48}Ti was measured by SP-ICP-MS (Figure 4.7). The time scan (Figure 4.7, D-1) was converted into a signal distribution histogram (Figure 4.7, D-2) and the most common Ti pulse intensity was plotted versus the concentration of dissolved Ti (Figure 4.7, D-3) in order to create the calibration curve. The Ti mass concentration (C) was then converted into the total mass transported into the plasma, the mass flux (W), using Eq. (1) (Figure 4.7, D-4). The slope of the calibration curve in Figure 4.7 D-4 (m) and its interception with the ordinate were inserted into Eq. (2) for the calculation of the mass of an individual particle (m_p).

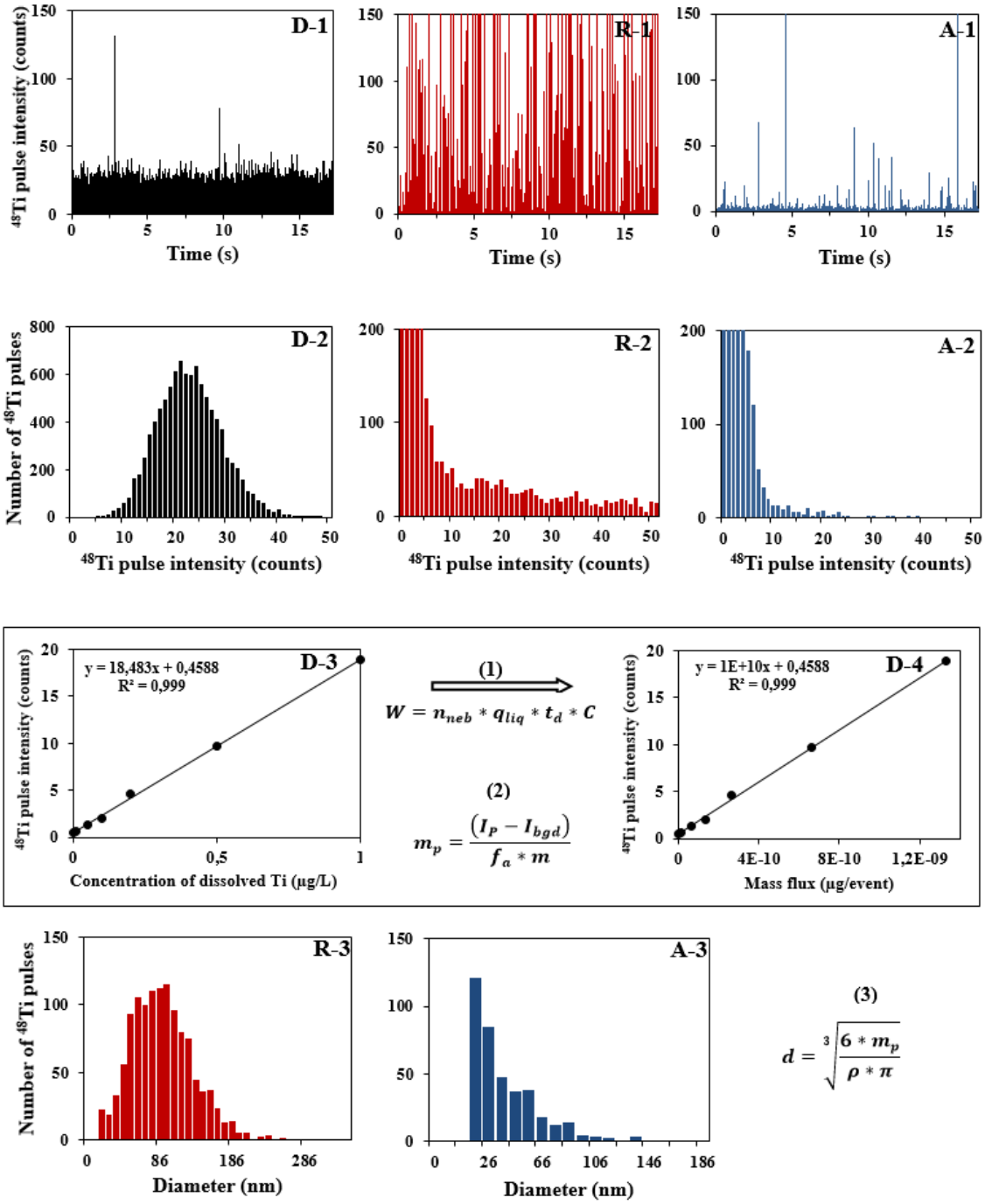


Figure 4.7: Data processing for the determination of the size distribution of TiO2NPs using SP-ICP-MS. Time scans for dissolved Ti (0.5 ng Ti/mL) (D-1), TiO_2NPs in rutile (0.2 ng Ti/mL) (R-1) and anatase (0.6 ng Ti/mL) (A-1); Corresponding signal distribution histograms for dissolved Ti (D-2), TiO_2NPs in rutile (R-2) and anatase (A-2); Calibration curve (dissolved Ti standards) created for particle size calculation (D-3); Calibration curve created for the calculation of the mass of an individual particle (D-4); Size distribution histograms for TiO_2NPs in rutile (R-3) and anatase (A-3). SP-ICP-MS measurements were performed at 10 ms dwell time (the schematic presentation is adapted from ref. [150], while the data are from the present work).

Time scans of the TiO_2NPs in rutile (Figure 4.7, R-1) and anatase (Figure 4.7, A-1) were measured and converted into signal distribution histograms (Figure 4.7, R-2, A-2). Before sizing, the background intensity was subtracted from the TiO_2NPs pulse intensity. The most important contribution to the background intensity arises from the dissolved component of the element in the solution, isobaric and/or polyatomic interferences (if these are not adequately eliminated) and the instrument background. A criterion based on three times the STD of the continuous background was selected for the discrimination of the NPs pulses from the background. Finally, in order to calculate the particle mass (m_p), the average background intensity (I_{bkg}) was subtracted from the individual pulse intensities (I_p) of the TiO_2NPs dataset (Figure 4.7, A-2, R-2) and inserted into Eq. (2). Each particle mass was then converted into a particle diameter (d) with the use of Eq. (3), which enabled to create a size distribution histogram (Figure 4.7, R-3, A-3).

It is clear that a large number of pulses above the background are obtained for anatase (Figure 4.7, A-1) and rutile (Figure 4.7, R-1) NPs, whereas a continuous background signal with only a few single pulses can be seen for the dissolved Ti (Figure 4.7, D-1). Namely, dissolved Ti is continuously introduced into the plasma, where a constant number of atoms are ionized and detected, while the TiO_2NPs in a sufficiently diluted suspension are not homogeneously distributed. Therefore, only a small fraction of aerosol droplets containing one NP are aspirated into the plasma, ionized into the packet of ions and detected as a single pulse. The lower intensity of pulses for the TiO_2NPs in anatase (Figure 4.7, A-1) in comparison to rutile (Figure 4.7, R-1) is related to the smaller NPs in the anatase. From the data in Figure 4.7 (R-3 and A-3), where the SP-ICP-MS measurements were performed at 10 ms dwell time, the mean diameters for the TiO_2NPs in the rutile and anatase were calculated to be 108 ± 10 nm and 29 ± 2 nm, respectively (expressed as an average of three replicates with the STD of the measurements). The corresponding full-width-at-half-maximum for the size distribution of the nanoscale rutile was 90 nm. Since the size distribution of the nanoscale anatase towards smaller particle sizes is below the size LOD, the half-width instead of the full-width-at-half-maximum was determined and calculated to be 15 nm.

The diameters and the full-width-at-half maximum for the rutile and anatase determined with the SP-ICP-MS analysis are in good agreement with the sizes and size distributions obtained from the TEM and DLS measurements. The peak tailing towards larger particle sizes is associated with the formation of larger particles due to the NPs aggregation. This observation is in accordance with the aggregates observed in the TEM and DLS measurements. However, aggregates with sizes larger than 100 nm for anatase and larger than 160 nm for rutile, determined with the TEM and DLS analysis, were not observed using SP-ICP-MS. Namely, the upper size limit for the particle diameter in the SP-ICP-MS is limited by the selective removal of large particles in the spray chamber or their incomplete vaporization in the plasma [168]. On the other hand, the wide size distribution in the histogram of rutile towards the smaller particle sizes indicates the polydispersed nature of the TiO_2NPs in rutile. While TEM and DLS analysis can distinguish between the diameter and length of the rod-shaped rutile NPs, signal in SP-ICP-MS analysis carries no information about two dimensions of non-spherical NPs. Therefore, the mean diameter of rod-shaped nanoscale rutile determined by SP-ICP-MS was calculated assuming a spherical particle shape.

4.2.2.1 Nanoparticle diameter limit of detection

LOD_{size} is related to the capability of a NP to produce a pulse with a number of counts equal to 3 times the standard deviation (σ) of the background (MilliQ water) [152]. From the background signals (2 counts per 10 ms dwell time) with STD of 1 count, the theoretical

LOD_{size} was calculated and found to be 37 nm. Nevertheless, from the size distribution histograms for the TiO_2NPs in the anatase and rutile crystalline phases (Figure 4.7, A-3 and R-3) it is evident that sizing of the TiO_2NPs is possible, even for particles smaller than 37 nm. Alternatively, for calculating the LOD_{size} the smallest pulse height that can be distinguished from the background was considered [168], and a similar LOD_{size} (34 nm for TiO_2NPs) was obtained. Similar LOD_{soze} for TiO_2NPs determined at ^{48}Ti isotope was reported by Dan et al. [156].

4.2.3 Quantitative determination of Ti number concentration in anatase and rutile

In order to evaluate the capability of the SP-ICP-MS method to quantitatively determine the Ti number concentration in TiO_2NPs, dispersions of anatase and rutile with different Ti mass concentrations (0.003-0.6 ng/mL) were prepared. First, the mean dissolved background intensity was subtracted from the pulse intensity using the 3 σ criterion. The particle number concentration was determined by dividing the frequency of the pulse events by the sample flow rate and the transport efficiency. The recoveries, defined as the ratio between the determined and expected Ti number concentrations in the TiO_2NPs, were calculated and are presented in Figure 4.8.

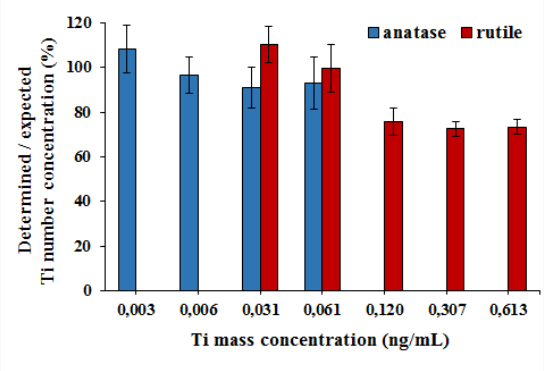


Figure 4.8: Ratio between the determined and expected Ti mass concentrations as a function of Ti mass concentration for anatase and rutile TiO_2NPs, measured by SP-ICP-MS at 10 ms dwell time. Results represent the mean value of three replicates with the STD of the measurements.

As evident, with increasing Ti concentrations, the recoveries are decreasing, and for the anatase they lie between 108 and 91 %, while for the rutile they are between 110 and 73 %. Namely, at higher NP concentrations the occurrence of multiple particle events, which are each counted as a single particle event, is increasing. With an increasing Ti concentration, the background signal is also increased, which makes it difficult to detect TiO_2NPs that produce signals near the background [150]. These phenomena led to an underestimation of the particle concentrations, regardless of their size (anatase or rutile). For this reason, it is important that the number of particles entering the plasma in one dwell time is controlled by the appropriate sample flow rate and/or dilution.

4.2.3.1 Nanoparticle concentration limit of detection

The limit of detection for particle number concentration (LOD_{NP}) is related to the capability of counting three NP events using Eq. (6) [168]:

$$LOD_{NP} = 3 \times \frac{1}{\eta_{neb} q_{liq} t_d} \tag{6}$$

From Eq. (6) it is evident that a lower LOD_{NP} can be achieved by improving the transport efficiency, increasing the sample flow rate, and/or using longer acquisition times. However, the flow rates should be carefully adjusted to prevent multiple particle events and reasonable acquisition times should be chosen. The LOD_{NP} for TiO_2NPs was found to be 2.3 x 10^5 NPs/L. To convert the LOD_{NP} to the mass concentration limits of detection, the size as well as the composition and density of each type of TiO_2NPs were considered and the calculated LOD_{NP} corresponded to 3.69 x 10^{-3} ng Ti/mL for rutile and 0.058 x 10^{-3} ng Ti/mL for anatase.

4.2.4 Influence of dwell time on the determination of the number concentration and size distribution of TiO_2NPs

In order to evaluate the influence of different dwell times on the quantification of TiO_2NPs by SP-ICP-MS, dwell times of 3, 5 and 10 ms were applied in measurements of the number concentrations and size distributions of the anatase and rutile. Aqueous suspensions of anatase and rutile at different Ti mass concentrations (0.003 and 0.006 ng/mL for anatase and 0.03 and 0.06 ng/mL for rutile) were prepared and measured at different dwell times (Figure 4.9). The Ti number concentrations were determined and the recoveries between the determined and expected Ti in the TiO_2NPs were calculated as described in the paragraph 4.2.3.

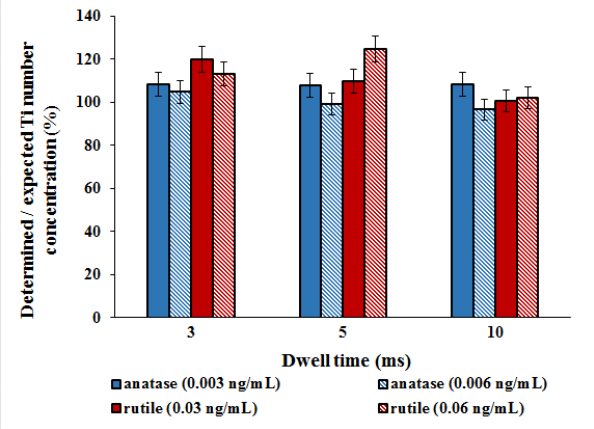


Figure 4.9: Ratio between the determined and expected Ti mass concentrations as a function of dwell time for two Ti mass concentrations (0.003 and 0.006 ng Ti/mL for anatase and 0.03 and 0.06 ng Ti/mL for rutile) of TiO_2NPs measured by SP-ICP-MS. Results represent the mean value of three replicates with the STD of the measurements.

From Figure 4.9 it is evident that with shorter dwell times the estimated Ti number concentration and consequently the measured recoveries are increasing for the anatase and rutile. As expected, 3 and 5 ms dwell times are too short for measuring the anatase and rutile for the investigated TiO_2NPs concentrations, since particle events within a single dwell period are only partially measured. The dwell time also affects the analytical performance of the dissolved Ti fraction. The LODs for the dissolved Ti fraction, which were determined at 3, 5 and 10 ms dwell times, were calculated to be 0.101, 0.071 and 0.045 ng Ti/mL, while the slopes of the calibration plots for the dissolved Ti were 28.4, 26.2 and 18.4 counts per µg Ti/L, respectively. Therefore, a 10 ms dwell time was selected

due to the lowest LOD, despite the reduced sensitivity for the determination of the Ti at this dwell time.

The influence of different dwell times on the particle size of TiO_2NPs in anatase and rutile determined by SP-ICP-MS was also evaluated. Dispersions of anatase and rutile were prepared at different Ti concentrations and measured at 3, 5 and 10 ms dwell times. The mean diameters were calculated from the size distribution histograms, following the procedure described in the paragraph 4.2.2., and were close to those observed in the TEM images. The dwell times do not have a significant influence on the determined mean diameters for the anatase and rutile NPs, despite the expected particle splitting between subsequent measurements, which may lead to an underestimation of the mean diameters if the dwell times are too short. However, a 10 ms dwell time was selected for the quantification and sizing of the TiO_2NPs and the dissolved Ti by SP-ICP-MS due to the better recoveries for the NPs mass concentration and the lower LOD for the dissolved Ti fraction at longer dwell times.

4.2.5 Simultaneous quantification of TiO_2NPs and dissolved Ti

In an evaluation of the biological effects of TiO_2NPs it is necessary to distinguish between the dissolved Ti ions and the nanoscale TiO_2. In environmental water samples, considerable concentrations of dissolved Ti, which originate from the soluble Ti compounds, can be present as a natural background. Although Ti is the ninth most abundant element in the Earth's crust, it is present in natural water in very low concentrations due to its very low mobility under almost all environmental conditions. However, some dissolved Ti may be released into stream water through the weathering of ferromagnesian minerals, anatase, etc. The Ti concentrations in natural water can range from <0.01 to 16.8 μg/L, with a median value of 0.9 μg/L [218].

Since there are no adequate monodispersed TiO_2NP standards available, the capability of SP-ICP-MS for simultaneous quantification of nanoscale and dissolved metal forms was first verified by an analysis of the monodispersed AgNPs with a 40 nm size in the presence of dissolved Ag. In Figure 4.10 an example of a time scan (A-1) and a signal distribution histogram (A-2) for 0.5 ng/mL of AgNPs in the presence of 0.5 ng/mL of dissolved Ag are presented. The SP-ICP-MS measurements were performed at 3 ms dwell time.

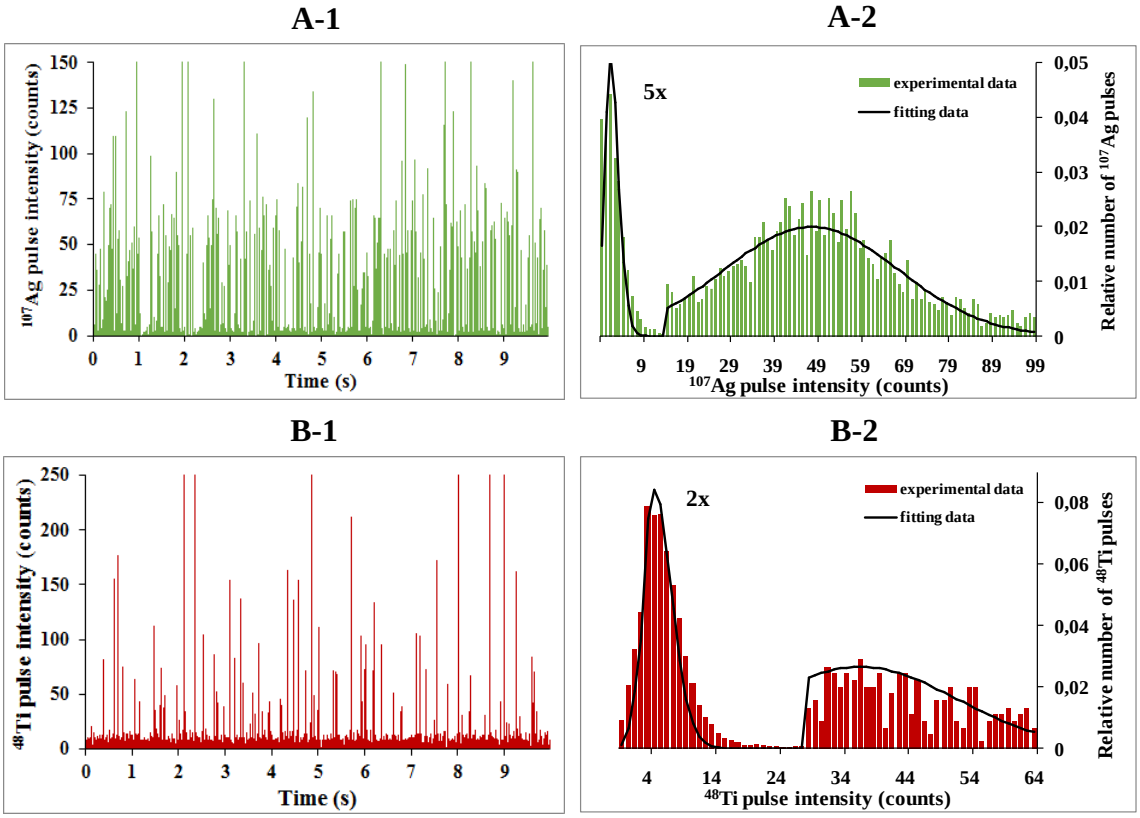


Figure 4.10: Time scans (A-1, B-1) and signal distribution histogram (A-2, B-2) for the mixture of 40 nm AgNPs and dissolved Ag and the mixture of TiO_2NPs and dissolved Ti, respectively. Measurements were performed by SP-ICP-MS at 3 ms dwell time for the AgNPs and 10 ms for the TiO_2NPs. Signals from the dissolved form of the element are fitted to a Poisson distribution, while signals from the particulate form of the element are fitted to a Gaussian distribution.

In the signal distribution histogram (Figure 4.10, A-2), first, the distribution for low-intensity signals, which represents the dissolved Ag and background, was fitted to the Poisson distribution, assuming that the ions randomly reach the detector. The second distribution, which was fitted to the Gaussian distribution, represents the AgNPs [143]. Once the dissolved and NP fractions had been resolved, each fraction was quantified by summing the number of counts for each distribution obtained in the histograms. Before the integration of the NP fraction, the mean dissolved background intensity was subtracted from the pulse intensity. The integration data was then compared with the calibration curve obtained with the use of dissolved Ag standards and the mass concentrations for Ag in the particulate and dissolved form were calculated [152]. The ratio between the determined and expected Ag mass concentrations was found to be 95 % for AgNPs and 98 % for dissolved Ag.

The same approach was then applied for the simultaneous quantification of TiO_2NPs and dissolved Ti. For this purpose, dispersions of nanoscale anatase and rutile in different concentrations, to which dissolved Ti was added, were prepared. In Figure 4.10, B-1 the time scan for the mixture of rutile (0.3 ng Ti/mL) and dissolved Ti (0.5 ng Ti/mL) is presented, indicating the presence of TiO_2NP pulses and a continuous background of dissolved Ti. The relative numbers of pulses (numbers of pulses divided by the total number of NP events) were plotted against pulse intensity, creating a signal distribution histogram (Figure 4.10, B-2). The well-resolved distributions for the dissolved and particulate forms

were fitted to Poisson and Gaussian functions, respectively, and the mass concentrations of the dissolved Ti and TiO_2NPs were calculated.

The results of the recovery tests for the simultaneous determination of the Ti mass concentrations in anatase and rutile TiO_2NPs and the dissolved Ti are presented in Table 4.4.

Table 4.4: Recoveries between determined and expected mass concentrations for the simultaneous determination of the Ti mass concentration in TiO_2NPs and dissolved Ti by SP-ICP-MS. Results represent the mean value of three replicates with the STD of the measurements.

	TiNP added (ng/mL)	**Ti(IV) added (ng/mL)**	**TiNP measured (ng/mL)**	**Ti(IV) measured (ng/mL)**	**Recovery TiNP (%)**	**Recovery Ti(IV) (%)**
rutile	0.298 ± 0.006	0.500 ± 0.005	0.298 ± 0.034	0.456 ± 0.031	100	91
	0.0323 ± 0.0006	0.050 ± 0.001	0.0312 ± 0.0024	0.047 ± 0.003	97	94
anatase	0.580 ± 0.012	0.500 ± 0.005	0.480 ± 0.020	0.525 ± 0.024	83	105
	0.348 ± 0.007	0.500 ± 0.005	0.320 ± 0.064	0.470 ± 0.038	92	94
	0.0580 ± 0.0012	0.050 ± 0.001	0.0562 ± 0.0010	0.0558 ± 0.0007	97	112
	0.0348 ± 0.0007	0.050 ± 0.001	0.0301 ± 0.0033	0.0628 ± 0.001	87	126

The data from Table 4.4 demonstrate that the recoveries for nanoscale rutile range from 97 and 100 %, and for dissolved Ti from 91 to 94 %. It can be further seen that for anatase these recoveries are between 83 and 97 % for the nanoscale Ti form and between 94 and 126 % for the dissolved Ti form. In general, the lower recoveries for TiO_2NPs in anatase in comparison to rutile may be attributed to the smaller size of the NPs that can be partially overlapped with the dissolved Ti background, which makes the discrimination of the dissolved and nanoparticulate forms more difficult. For the same reason, recoveries higher than 100 % were observed for the dissolved Ti.

4.2.6 Quantification and sizing of TiO_2NPs in river water samples

In order to assess the applicability of the procedure developed for the sizing and quantification of TiO_2NPs in environmental waters, a river water sample was collected. It contained 38 mg Ca/L, which causes severe isobaric interferences in the determination of Ti at m/z 48. To avoid this type of interferences, the Ti concentrations in the river water measured by ICP-MS and SP-ICP-MS were performed at m/z 47, while the He mode was applied to compensate for possible polyatomic interferences. The theoretical LOD_{size} determined for TiO_2NPs at ^{47}Ti isotope (7.3 % abundance) was found to be 55 nm and is higher than LOD_{size} determined at the most abundant ^{48}Ti isotope (73.72 % abundance) (37 nm) (see data in paragraph 4.2.2.1.). Namely, the use of a more abundant isotope contributes to the higher sensitivity and consequently to the lower LOD_{size}. In the literature, LOD_{size} determined at ^{47}Ti or ^{49}Ti isotopes ranged from 65 to 100 nm [142, 148, 168, 177]. Lower LOD_{size} determined at ^{47}Ti in the present study is related to the low baseline due to the use of He gas that effectively removes polyatomic interferences in ICP-MS determination.

The total Ti concentration in the river water determined by ICP-MS was found to be 0.602 ± 0.012 ng Ti/mL, which is within the range reported for other natural waters [218]. In order to determine the dissolved and nanoparticulate fractions of Ti in the river water SP-ICP-MS analysis was carried out. The time scan of the river water sample is presented in Figure 4.11 A.

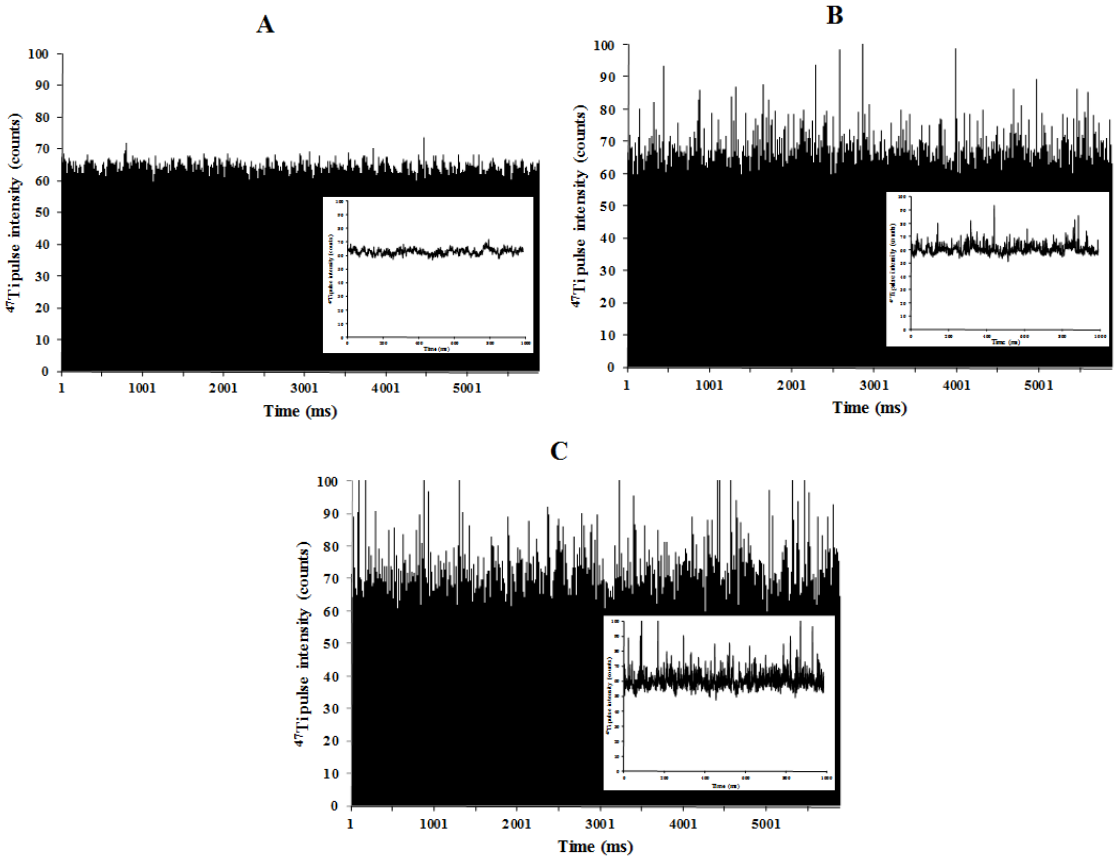


Figure 4.11: Time scans of river water sample (A), sample spiked with rutile (0.0256 ng Ti/mL) (B) and sample spiked with anatase (0.00113 ng Ti/mL) (C). SP-ICP-MS measurements were performed at 10 ms dwell time.

Due to the increased signal intensity of the dissolved Ti in the river water, which can be seen in the elevated background (enlarged time scans in Figure 4.11), the overlap of the signals for the NPs and the dissolved fraction is more pronounced. Therefore, to distinguish between the dissolved and nanoscale Ti, the 5 σ criterion was chosen [144] and the mass concentrations were determined as described in the paragraph 4.2.5. The concentration of dissolved Ti was 0.588 $\pm$ 0.022 ng Ti/mL, while nanoscale Ti was found to be below the LOD_{NP} (<0.0001 ng/mL), since no sources of titania, e.g. industrial activities or release of nano titania from sunscreens (swimming in the river), were present in the vicinity. To evaluate the influence of the sample matrix on the determination of the TiO_2NPs mass concentration and their size, the river water was spiked with different concentrations of rutile (0.0256 ng Ti/mL) and anatase (0.00113 ng Ti/mL). Corresponding time scans, which clearly indicate the appearance of TiO_2NP pulses and the continuous background of dissolved Ti present in the river water, are presented in Figure 4.11 (B, C), while the recoveries calculated as the ratio between the determined and expected TiNPs concentrations are presented in Table 4.5.

Table 4.5: Simultaneous determination of the mass concentration of dissolved Ti and TiNPs in a river water sample by SP-ICP-MS and recoveries between the determined and expected mass concentrations in a sample spiked with TiO_2NPs (anatase and rutile). Results represent the mean value of three replicates with the STD of the measurements.

Sample/ Spiked sample	**TiNP added (ng/mL)**	**Ti(IV) measured (ng/mL)**	**TiNP measured (ng/mL)**	**Recovery TiNP (%)**
river water	/	0.588 ± 0.022	< 0.0001	/
rutile	0.0256 ± 0.0005	0.581 ± 0.030	0.0267 ± 0.0013	104
anatase	0.00113 ± 0.00002	0.585 ± 0.037	0.00156 ± 0.00008	138

The expected Ti mass concentrations were determined after the microwave-assisted digestion of the TiO_2NP suspensions [200]. It is evident that the addition of TiO_2NPs to the river water has no influence on the quantification of the dissolved Ti originally present in the sample. Good recoveries were obtained for the nanoscale rutile (104 %), while for anatase, with the smaller NPs, the higher recoveries (138 %) are most likely related to the contribution of the dissolved Ti background to the NPs signal.

For the sizing of the TiO_2NPs added to the river water, it was necessary to accurately determine the transport efficiency. For this purpose, monodispersed AgNPs (40 nm) and dissolved Ag standard solutions were prepared in the river water and the transport efficiency calculated using the particle size method. η_{neb} for the river water was found to be 3.9 ± 0.2 %. Following the procedure described in paragraph 4.2.2., the mean diameters of TiO_2NPs added to the river water were calculated and found to be 128 nm for the rutile and 44 nm for anatase. Although the theoretical LOD_{size} (55 nm) is higher than the mean diameter of anatase determined in the river water, sizing of the TiO_2NPs is possible even for smaller particles. Slightly larger diameters than those determined for the rutile and anatase dispersed in MilliQ water (108 and 29 nm, respectively) can be attributed to the NPs aggregation due to the ionic strength of the river water.

The results presented in the chapter 4.2 are based on the data of the published article [219].

4.3 The Behavior of Zero-Valent Iron Nanoparticles and Their Interactions with Cd^{2+} in Wastewaters Investigated by Single Particle ICP-MS

4.3.1 Characterization of nZVI nanoparticles

The basic parameters of the nZVI (Nanofer25 slurry) used in the nanoremediation experiments are presented in Figure 4.12.

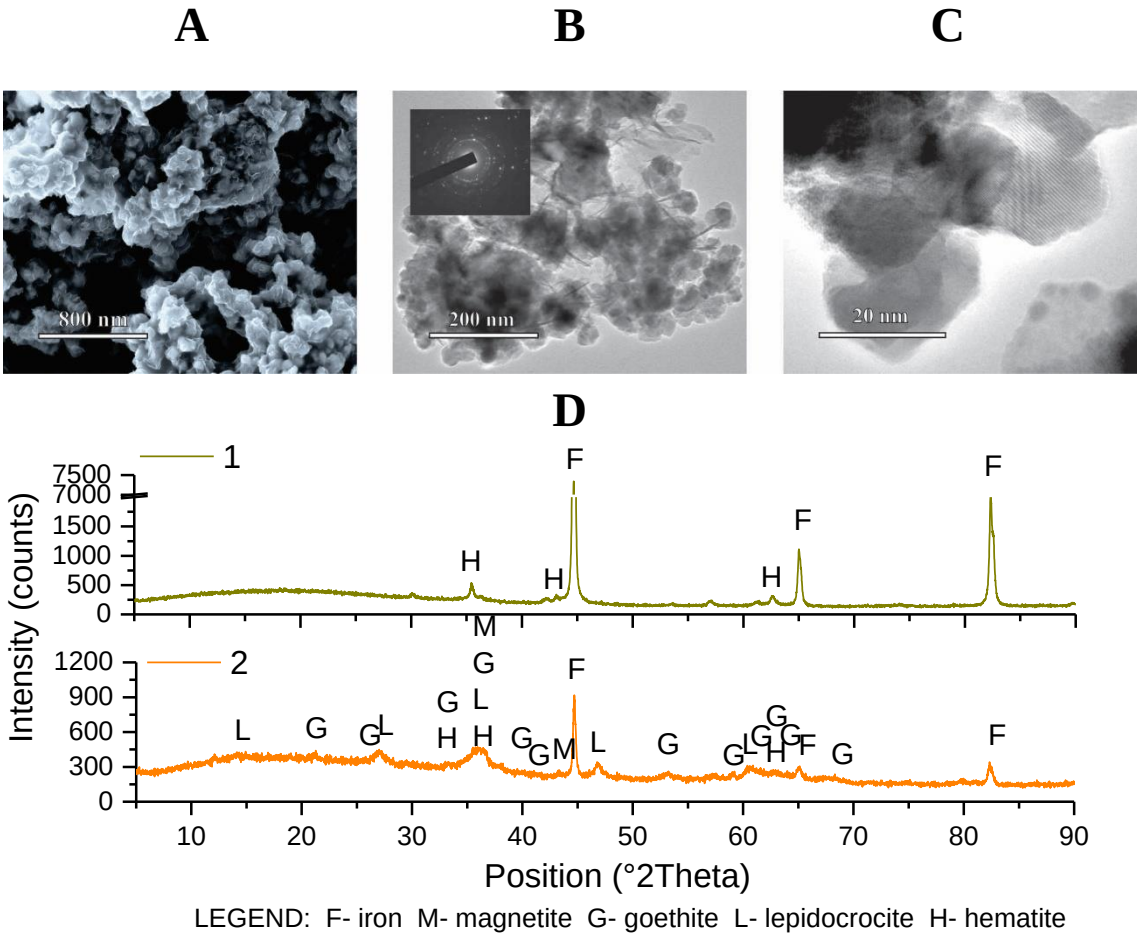


Figure 4.12: (A) FESEM picture, (B) SAED pattern, (C) TEM picture of fresh nZVI and powder X-ray diffraction pattern of (D1) fresh nZVI in MilliQ water and (D2) nZVI after 23 days of settling in the effluent wastewater.

FESEM and TEM analysis showed that the primary size of nZVI particles lies between 20 and 80 nm and that their shell is 4 – 6 nm thick. It can also be seen that individual nZVI particles are larger than 200 nm. Rounded particles, which are irregularly shaped, form aggregates of µm size. X-ray powder diffraction (XRD) analysis further demonstrated that nZVI have a well-defined crystalline core structure, where a zero-valent iron (α-Fe^0) body-centred cubic cell (bcc) phase prevails. Less pronounced peaks that belong to the Fe present in the oxide shell of the nZVI are the peaks of the hematite (α-Fe_2O_3) and goethite (α-FeOOH) phase for fresh nZVI dispersed in MilliQ water and for nZVI settled in the effluent wastewater after 23 days, respectively. The mass fraction of available Fe^0 content in nZVI, determined by a H_2 evolution method based on the principle described by Liu et al. [220],

was followed in fresh nZVI dispersed in MilliQ water and in nZVI in different aqueous matrices (after mixing for 4 h) with increasing settling time. The Fe^0 content in freshly dispersed nZVI was found to be 85 wt. %, while the mass fraction of Fe^0 in different aqueous matrices was reduced over settling time. Corrosion of Fe^0 was the fastest during the first 4 h of mixing (65 wt. % of Fe^0 was oxidized) and slowed down during the process of particle settling. When nZVI were exposed to different water matrices, Fe corrosion products were formed the most rapidly in synthetic wastewater, while a higher percent of the oxidized Fe was found in the effluent wastewater after 7 days of settling. The process of Fe^0 oxidation was the slowest in MilliQ water at all the studied settling times.

Cd^{2+} can be potentially released from nZVI into the remediated water due to nZVI ageing [20, 221]. In addition, matrix constituents can also complex Cd^{2+} and release it from nZVI [221]. In order to verify the purity of nZVI, total Cd concentration was determined by ICP-MS after digestion of nZVI in hydrochloric acid and was found to be 3.70 µg/g.

4.3.2 Optimization of Fe measurement by triple quadrupole ICP-MS

In order to achieve a sensitive and interference-free measurement of very low concentrations of nZVI in wastewaters by SP-ICP-MS, four different gases, i.e. helium (He) as a collision gas in high energy collision mode (HECM) as well as hydrogen (H_2), oxygen (O_2) and ammonia (NH_3) as reaction gases, were tested using the MS/MS mode. First, the flow rate for each gas was optimized to obtain the highest ^{56}Fe signal intensity of a standard Fe solution (1 µg/L) and the lowest signal intensity of a blank solution (MilliQ water). The optimal flow rates for He, H_2, NH_3 and O_2 were found to be 9.0 mL/min, 5.0 mL/min, 1.8 mL/min in 3 mL/min of He and 3.6 mL/min, respectively.

To study the reactions between gas molecules and the ^{56}Fe isotope in the collision-reaction cell, product ion scanning was used to identify the main reaction products. The highest sensitivity was observed for a single product ion $^{56}Fe^+$. For O_2 and NH_3, a selective and efficient reaction with ^{56}Fe was also observed, resulting in the formation of FeO (at *m/z* 72) and $Fe(NH_3)_2$ (at *m/z* 90) and $Fe(NH_3)_3$ (at *m/z* 107) complexes. The most sensitive reaction product ions identified were selected for further method optimization.
The efficiency of different measurement modes for reducing the most common polyatomic interferences ($^{40}Ar^{16}O^+$, $^{40}Ca^{16}O^+$) was studied by measuring the ^{56}Fe signal intensity in MilliQ water and in 50 µg/L Ca solution, both spiked with 1 µg/L Fe (Figure 4.13). The calculated signal-to-background (S/B) ratios were high in all measurement modes when Fe was measured as a single product ion. Among all the reaction gases tested, the highest S/B ratio was achieved using H_2 reaction gas, demonstrating its effectiveness in removing the interferences while retaining Fe sensitivity.

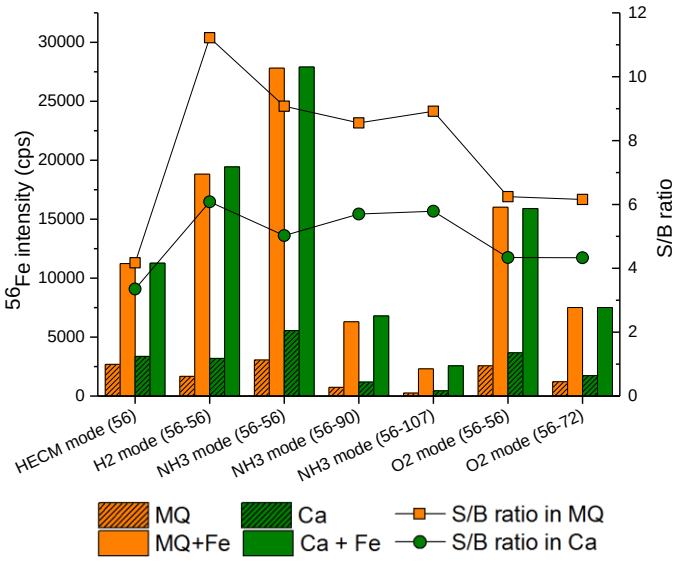


Figure 4.13: ^{56}Fe signal intensity measured in MilliQ water (MQ), MQ spiked with 1 µg/L Fe (MQ + Fe), 50 µg/L Ca solution (Ca) and 50 µg/L Ca solution spiked with 1 µg/L Fe (Ca + Fe) applying different measurement modes. The signal-to-background (S/B) ratio of ^{56}Fe in MQ or 50 µg/L Ca solution is also presented.

The good performance when detecting iron as ^{56}Fe isotope in all three reaction gases was also confirmed by achieving the highest sensitivity and the lowest LOD (Table 4.5). However, good agreement between the determined and certified Fe concentrations in two different quality control materials (surface and wastewater) was found only for H_2 reaction gas. In addition, the spike recovery test for 50 µg/L Ca solution and effluent wastewater confirmed the accuracy of the method for the determination of Fe in environmental water samples using H_2 as a reaction gas.

Table 4.5: Sensitivity, limits of detection (LOD) and accuracy check for the determination of Fe by QQQ ICP-MS using different collision–reaction cell conditions. For the accuracy check, SPS-SW1 surface and SPS-WW1 waste water quality control materials were used. Spike recovery test was also performed in 50 µg/L Ca solution and effluent wastewater.

Gas	**Sensitivity (cps/µg)**	**LOD_{size} (nm)**	**LOD_{NP} (ng/L)**	**Fe concentration of the background (ng/L)**
NH_3	5.02 x 10^{12}	45	1.42	105 ± 5
O_2	2.13 x 10^{13}	43	0.779	263 ± 23
H_2	3.42 x 10^{13}	36	0.709	134 ± 2

The performances of H_2, NH_3 or O_2 as reaction gases in MS/MS mode were further compared for measurement of nZVI by SP-ICP-MS. Limits of detection for the nZVI size (LOD_{size}) and mass concentration (LOD_{NP}), Fe concentration of the background as well as sensitivity are presented in Table 4.6. As evident, H_2 used as a reaction gas showed the highest sensitivity for measuring Fe at *m/z* 56 in MS/MS mode and the most effectively removed polyatomic interference of $^{40}Ar^{16}O^+$. Consequently, the lowest LOD_{size} (36 nm) and LOD_{NP} (0.709 ng/L) were obtained. Therefore, H_2 reaction mode was chosen in further experiments for quantification and sizing of nZVI by SP-ICP-MS.

Table 4.6: Sensitivity, LOD_{size}, LOD_{NP} and Fe concentration of the background for nZVI, determined by SP-ICP-MS at m/z 56, using different reaction gases in MS/MS mode.

				SPS-SW1	SPS-WW1	10 µg/L Fe + 50 µg/L Ca solution	10 µg/L Fe + effluent wastewater
Measurement mode		**Sensitivity (cps L/µg)**	**LOD (µg/L)**	**Recovery (%)**	**Recovery (%)**	**Spike recovery (%)**	**Spike recovery (%)**
HECM	Single quad	20,198	0.0300	109.8	102.8	112.3	94.3
H_2	(56 → 56)	38,027	0.0079	100.0	98.9	106.5	95.3
O_2	(56 → 56)	29,211	0.0181	127.8	101.6	109.3	95.9
	(56 → 72)	14,540	0.0252	103.3	103.3	110.9	99.4
NH_3	(56 → 56)	51,018	0.0121	105.0	106.9	157	107
	(56 → 90)	12,693	0.0083	107.4	108.7	134	90.2
	(56 → 107)	4,784	0.0293	132.3	101.5	158	91.1

Under the optimized instrumental parameters for SP-ICP-MS analysis of nZVI dispersed in MilliQ water, their size distribution was determined. Three consecutive analyses are presented in Figure 4.14. The median diameter was calculated to be 43 nm, which correlates well with the sizes observed by TEM. Good repeatability (2.57 %) for the determination of size distribution was obtained. The determined diameter is however only the approximation of the actual nZVI size, since sizing in SP-ICP-MS relies on the assumption that particles are spherical, which can, in case of irregularly shaped rounded nZVI particles, affect the accuracy of the size determination.

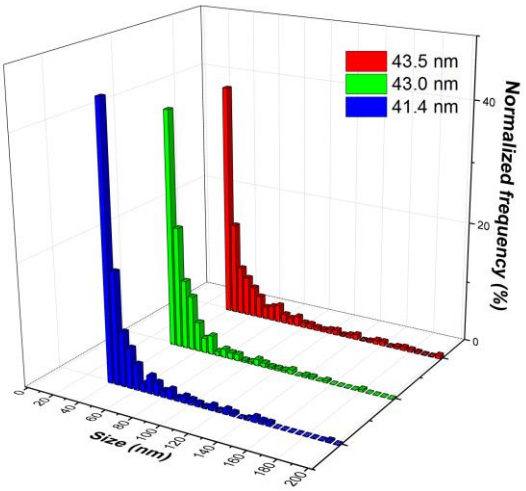


Figure 4.14: Repeatability of the size distributions of nZVI dispersed in MilliQ water, determined in H_2 reaction mode by SP-ICP-MS (bin size 5 nm). Numbers in the legend show median diameters for the individual size distribution.

4.3.3 Problems related to SP-ICP-MS sizing under changing chemical composition of nZVI

Determination of the particles size by SP-ICP-MS requires knowing their chemical composition, shape and density, in order to convert the mass of element per particle into the corresponding size. If this information is not available, an estimation of the particle size can be done assuming a specific shape and composition [129].

Data on nanoparticle characterization (Figure 4.12) indicate that nZVI have a core-shell structure in which the core of fresh nZVI dispersed in MilliQ water contains 85 wt. % Fe^0 and the shell is comprised of 15 wt. % Fe_2O_3. Based on these data, particle density and mass fraction of Fe in nZVI were calculated to be 7.479 g/mL and 0.955, respectively. It is generally known that the oxide shell of nZVI tends to grow with time of remediation due to nZVI oxidation, while the Fe core shrinks. As a consequence of altering the chemical composition, a mass fraction of Fe^0 in nZVI is also changing with time. For accurate determination of nZVI size by SP-ICP-MS, knowledge of the Fe mass fraction and chemical composition of nZVI is needed. Therefore, the available Fe^0 content in nZVI in various sample matrices at different settling times was determined as described in paragraph 4.3.1., and used for calculation of the density and mass fraction of Fe in nZVI, assuming that the composition of the oxide shell over the 7 days of settling remained in the form of Fe_2O_3 for nZVI in MilliQ water and in the form of FeOOH for nZVI in synthetic and effluent wastewater (Figure 4.12).

The changing chemical composition of nZVI with increasing time of exposure to the different water matrices affects also the calculated LOD_{size} (Eq. (5)). Although the signal intensity of the Fe background remains constant, LOD_{size} changes due to different Fe mass fraction and particle density. Therefore, LOD_{size} for particles with changing composition ($LOD_{size,2}$) was calculated from the LOD_{size} of the fresh nZVI in MilliQ water (36 nm, $LOD_{size,1}$) following the Eq. (7) [167].

$$LOD_{size,2} = LOD_{size,1} \times \left(\frac{f_{a,2}}{f_{a.1}} \times \frac{\rho_2}{\rho_1} \right)^{-1/3} \quad (7)$$

For instance, for 0.25 g/L of nZVI exposed to the effluent wastewater for 1 hour the calculated LOD_{size} was increased to 54 nm due to the changed chemical composition of nZVI. Calculated LOD_{size} excludes low-intensity events which do not correspond only to the instrument background and dissolved Fe but also to the nZVI smaller than LOD_{size} (according to the TEM and FESEM analysis nZVI have radii between 20 and 80 nm). Therefore, the Fe fraction that is below this LOD_{size} cannot be considered as the background, which consists only of dissolved Fe ions, but includes also NPs smaller than LOD_{size}. This was taken into account when interpreting the data obtained by SP-ICP-MS.

4.3.4 The influence of sample matrix on the nZVI behavior during nanoremediation

Different factors, such as magnetic properties of nZVI that cause their aggregation, surface oxidation, which leads into the formation of corrosion product precipitates, and interactions with the environmental components, influence the behavior of nZVI in remediated waters. These processes change with time due to the reactive nature of the nZVI and mainly depend on the properties of environmental matrix (ionic strength and organic matter), which affects electrosteric stabilization of nZVI [222].

In order to study the influence of different water matrices on the behavior of nZVI, MilliQ water, synthetic and effluent wastewater were treated with 0.25 g/L of nZVI. The concentration of Fe fraction $>$ and $\leq LOD_{size}$, as well as nZVI number concentration and median diameters were determined by SP-ICP-MS (Figure 4.15). The Fe concentrations at each settling time were normalized to the concentration determined in the relevant matrix at time 0 h.

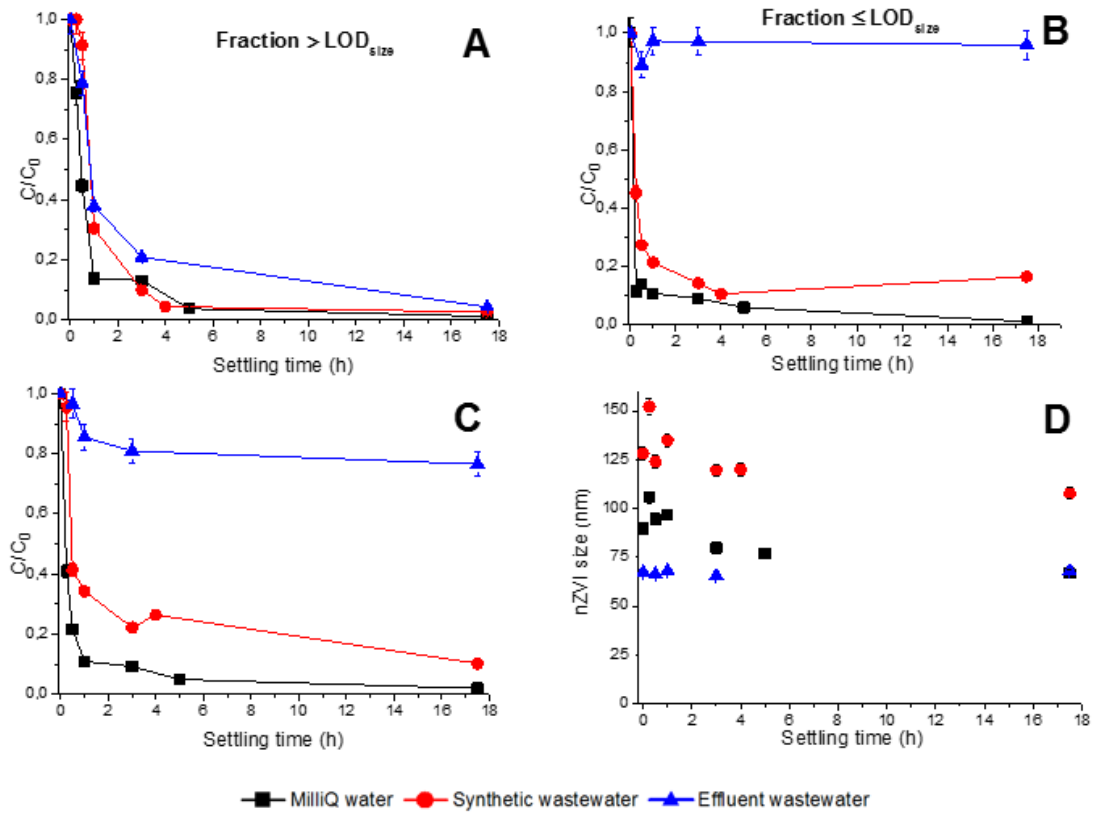


Figure 4.15: The influence of settling time on the nZVI mass concentration (A, fraction size > LOD_{size} and B, fraction size ≤ LOD_{size}), number concentration (C) and their size (D) in the water samples investigated. nZVI concentrations at different settling times were normalized to the initial nZVI concentration determined at time 0 h. Error bars represent STD between two measurements of the same sample.

As expected, concentrations of nZVI in all three matrices decrease with the increasing settling time due to the precipitation of Fe corrosion products. Settling of nZVI is the slowest in the effluent wastewater and the fastest in MilliQ water. Only a small percentage of nZVI > LOD_{size} remains suspended in MilliQ water (1.1 %), synthetic wastewater (2.6 %) and effluent wastewater (4.3 %) (related Fe concentrations 0.35, 0.92 and 5.7 µg/mL, respectively). Despite the highest concentration of cations and the highest electrical conductivity, which favor the particle settling, the high content of organic matter stabilized the nZVI in the effluent wastewater. Namely, organic matter adsorbs on the nanoparticle surface, providing strong steric repulsive forces that oppose the attractive magnetic interactions of nZVI [223]. On the other hand, in MilliQ water with very low ionic strength and organic matter, attractive magnetic forces between particles prevail, leading to faster aggregation and sedimentation of nZVI. Consequently, nZVI do not have time to be oxidized. This is in agreement with our observation that MilliQ water is the least corrosive among the investigated matrices.

We further observed that nZVI fraction ≤ LOD_{size} (NPs smaller than LOD_{size} and dissolved Fe) in effluent wastewater remains almost constant over 18 hours of settling, most probably due to the dissolution of nZVI, which could be attributed to the high ionic strength, high amount of organic acids (organic matter) and dissolved Fe already present in the effluent wastewater (i.e. 160 µg/L). Panias et al. [224] reported that these factors

favor the dissolution of Fe oxide. However, by SP-ICP-MS, the dissolved Fe content could not be discriminated from nZVI particles smaller than LOD_{size}.

From Figure 4.15 it can also be seen that after 4 h of mixing in MilliQ water, synthetic and effluent wastewater, the sizes of nZVI particles were at the start of settling 90 nm, 128 nm and 67 nm, respectively, and were significantly larger from the size of freshly dispersed nZVI in MilliQ water (43 nm). This indicates that oxidation of nZVI and formation of aggregates of Fe corrosion products occur already during the dispersion of nZVI by mixing. In MilliQ water and synthetic wastewater nZVI aggregates tend to grow in the first half hour of settling. Afterwards the large aggregates settled, while smaller particles still remained in the solution. The decrease in nZVI size was the most pronounced in synthetic wastewater (from 152 nm to 107 nm) and MilliQ water (from 105 nm to 67 nm), while the size of nZVI in the effluent wastewater (around 67 nm) did not change with the time of settling. The smallest particle size observed in the effluent wastewater was related to slow sedimentation and strong dissolution of nZVI. Larger aggregates (around 110 nm) remained in synthetic wastewater even 18 h after the start of settling, since strong attractive electrostatic forces caused by high ionic strength of matrix kept them dispersed in solution.

4.3.5 The influence of Fe load on the nZVI behavior during nanoremediation of effluent wastewater

Oxidation of nZVI and formation of iron corrosion products lead to the generation of aggregates, which settle when reaching a critical size. The speed of this process depends on nZVI properties (i.e. their radius, zeta potential, particle density, magnetic properties) as well as on the initial particle concentration [225].

To investigate the influence of Fe load on the sedimentation and the size of the formed aggregates, the concentration of nZVI fraction $>$ and $\leq LOD_{size}$ as well as the nZVI median diameter were followed in the effluent wastewater treated with different Fe loads at different settling times (Figure 4.16). We observed that the Fe concentrations determined in water at time 0 h presented only 8 to 30 % of initially added nZVI, since most of the particles settled already during the mixing procedure. As expected, the concentration of nZVI $> LOD_{size}$ decreases with increasing the settling time (Figure 4.16A). This decrease was faster at higher initial concentrations of nZVI, since interactions between particles (i.e. attractive electromagnetic forces) were more pronounced, leading to nZVI aggregation and settlement. From Figure 4.16 it can be further seen that after 7 days of settling more particles remained dispersed in effluent wastewater treated with lower Fe loads (lower degree of interactions between particles and higher degree of stabilization with organic matter). After 7 days of settling, Fe concentrations (Fe fraction $> LOD_{size}$) of nZVI that remained dispersed in solution were 0.436, 0.619, 0.034 and 0.008 µg/L when effluent wastewater was treated with 0.1, 0.25. 0.5 and 1.0 g/L Fe loads, respectively.

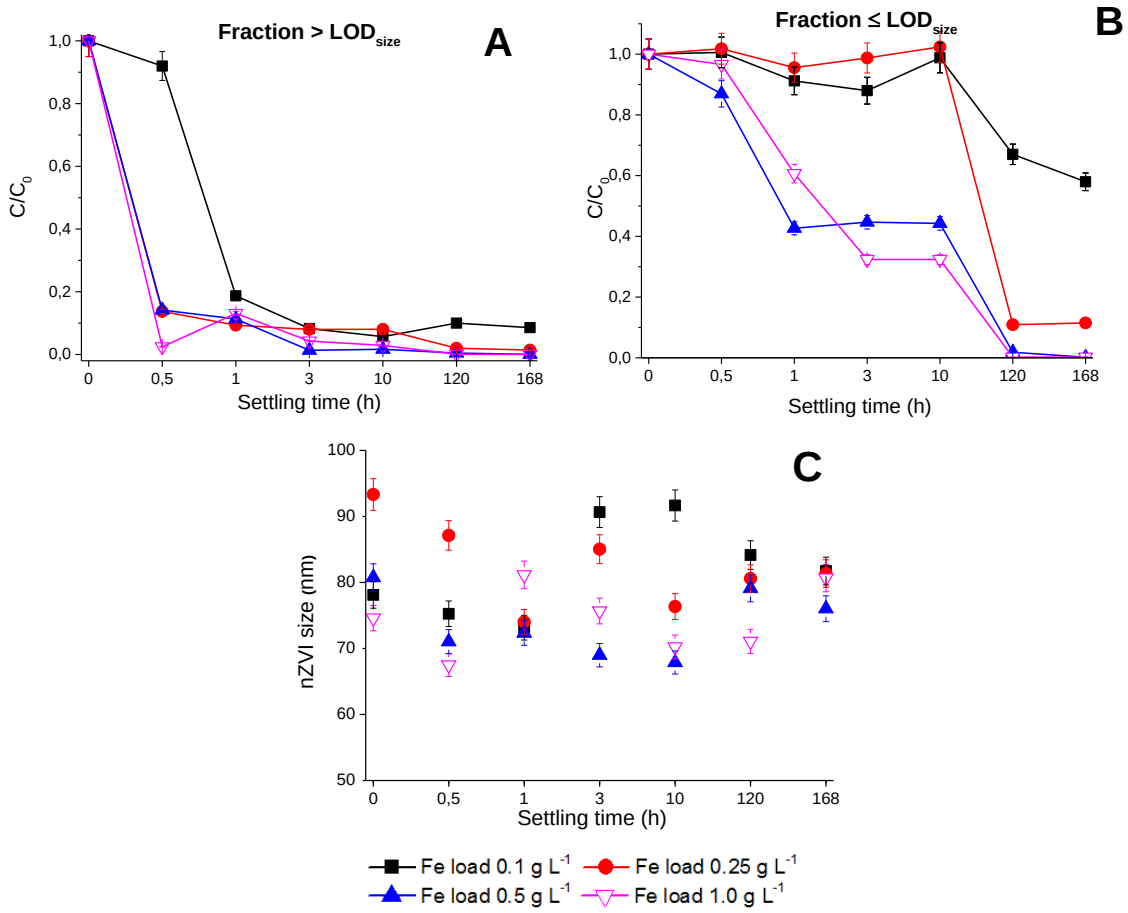


Figure 4.16: The influence of settling time on the nZVI mass concentration (A, fraction size > LOD_{size} and B, fraction size ≤ LOD_{size}) and nZVI size (C) in effluent wastewater treated with different Fe loads. nZVI concentrations at different settling times were normalized to the initial nZVI concentration determined at time 0 h. Error bars represent STD between two measurements of the same sample.

Similar to the findings from Figure 4.16A, the fraction ≤ LOD_{size} (Figure 4.16B) also remained the highest in wastewater treated with 0.1 g/L Fe load. Although by SP-ICP-MS it is not possible to distinguish between the dissolved Fe content and nanosized Fe with particles smaller than LOD_{size}, the high amount of Fe that remained in the solution even after 7 days of settling (60 %) indicates an inefficient remediation and may also represent a nano threat. The data from Figure 4.16B further demonstrate that at Fe loads 0.25 g/L or higher, the fraction ≤ LOD_{size} is efficiently removed from the solution already after 5 days of settling. Considering also the fast settling of nZVI particles > LOD_{size}, an efficient nanoremediation procedure can be expected with a low environmental nano risk.

Since in the first three hours after mixing the particle settling was the most intensive (Figure 4.16A), the sizes of nZVI that remained dispersed in the solution were extended over a broad range from 70 to 90 nm (Figure 4.16C). At longer settling times, the size range of particles tended to decrease and was between 75 and 82 nm after 7 days. Larger nZVI particles were observed in the solutions treated with lower Fe loads, which is related to a stronger interaction between particles that led to the formation of larger aggregates.

4.3.6 Investigation of Cd^{2+} interactions with nZVI and Cd^{2+} removal from contaminated waters

To prevent contamination of drinking water with Cd^{2+}, which is one of the common pollutants released into the environment, it is necessary to remove this toxic metal from contaminated sites, and thus prevent its release into drinking water supplies [226]. nZVI have been employed as an efficient adsorbent for the Cd^{2+} removal from contaminated waters. With the use of XPS (X-ray photoelectron spectroscopy) and EDX (energy-dispersive X-ray) analyses it has been shown that Cd^{2+} ions are removed by chemisorption, which includes the formation of nZVI-Cd inner-sphere surface complexes [227].

In order to follow the removal of Cd^{2+} from contaminated waters, its interactions with nZVI during nanoremediation procedure were studied by measuring Cd in SP-ICP-MS mode. Cd^{2+} attached to nZVI appeared as the pulses (above the continuous background). An example of such interaction in synthetic wastewater spiked with 100 µg Cd^{2+}/L and treated with 0.25 g/L of nZVI is presented in Figure 4.17.

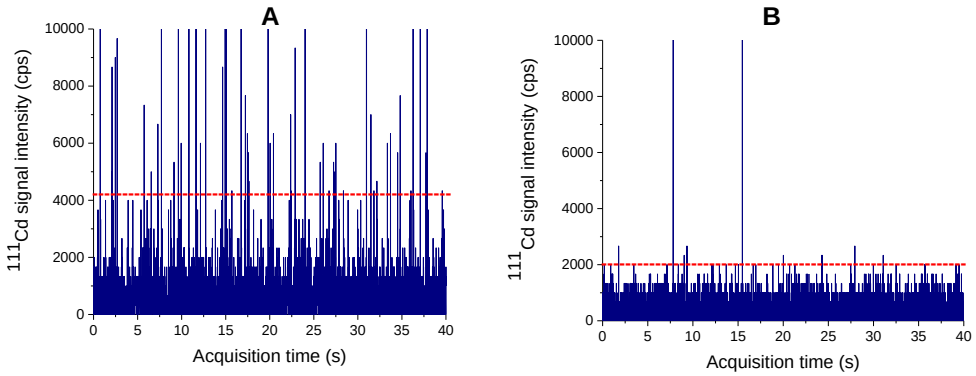


Figure 4.17: Time scans for ^{111}Cd measured in single particle mode at settling time 0 h (A) and 18 h (B) in synthetic wastewater with the applied threshold between the background and particles signal.

As expected the extent of interactions was significantly higher at the beginning of nZVI settling (Figure 4.17A) than after eighteen hours (Figure 4.17B). The influence of settling time on concentration of dissolved Cd^{2+} and Cd^{2+} attached to nZVI was then followed in MilliQ water, synthetic and effluent wastewater spiked with 100 µg Cd^{2+}/L and treated with 0.25 g/L of nZVI (Figure 4.18).

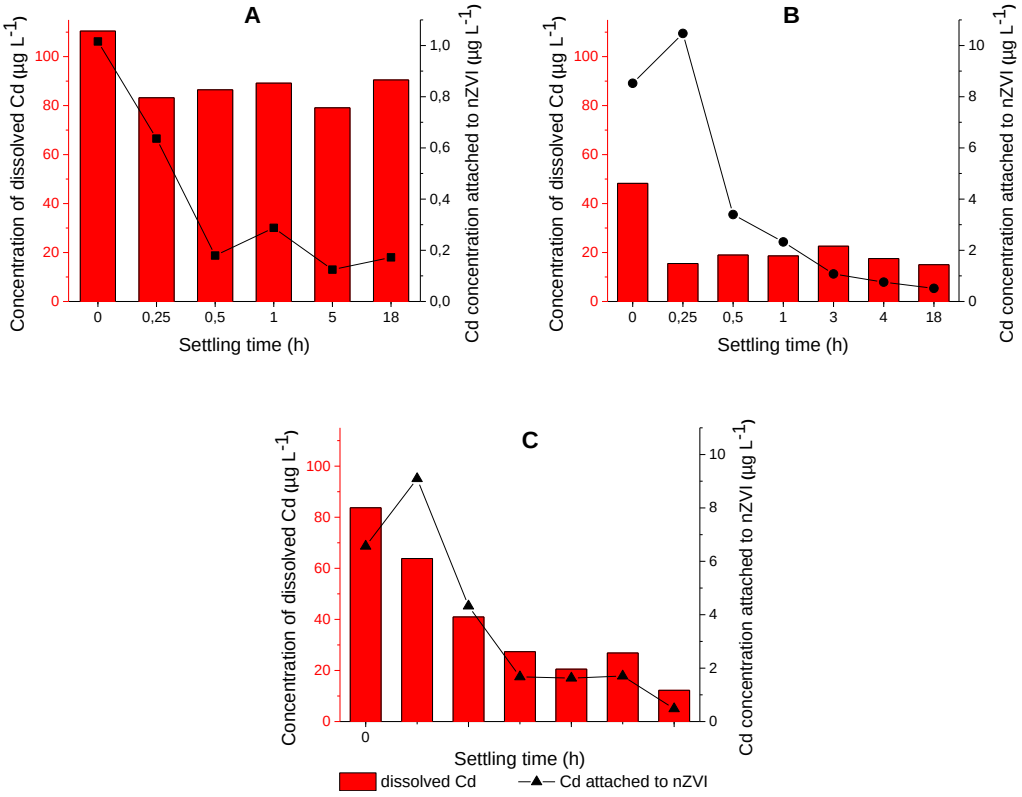


Figure 4.18: The influence of settling time on the concentration of dissolved Cd^{2+} and Cd^{2+} attached to nZVI in MilliQ water (A), synthetic wastewater (B), and effluent wastewater (C) spiked with 100 µg Cd/L and treated with 0.25 g/L of nZVI.

As evident, both Cd concentrations gradually decreased with increasing the settling time, which indicates that interactions of Cd^{2+} with nZVI are the strongest at the beginning of settling, due to the initially available larger amounts of adsorptive sites on nZVI. As time elapsed, Fe corrosion products are formed, which leads to aggregation of nZVI, resulting in the decrease of their specific surface area. Therefore, the total amount of Cd^{2+} that can be attached to nZVI is reduced [227, 228]. We further observed that 19, 73 and 86 % of total Cd^{2+} concentration was removed from MilliQ water, synthetic wastewater and effluent wastewater, respectively. The concentration of Cd^{2+} attached to nZVI was because of fast settling of nZVI in MilliQ water (see also data from Figure 4.15), about 10 times lower than in the synthetic and effluent wastewater. Consequently, nanoremediation of Cd^{2+} in MilliQ water was not effective. Due to more efficient dispersion of nZVI in synthetic and effluent wastewater, a higher amount of Cd^{2+} was attached to nZVI and removed with Fe corrosion products. The slower rate of Cd^{2+} removal from effluent wastewater is related to a higher amount of organic matter, which coated the active sites of nZVI particles, reducing the extent of their interactions with Cd^{2+}.

To verify the applicability of SP-ICP-MS for studying the interactions of Cd^{2+} with nZVI under realistic environmental conditions, the concentration of dissolved Cd^{2+} and Cd^{2+} attached to nZVI was followed in effluent wastewater treated with different Fe loads after different settling times (Figure 4.19).

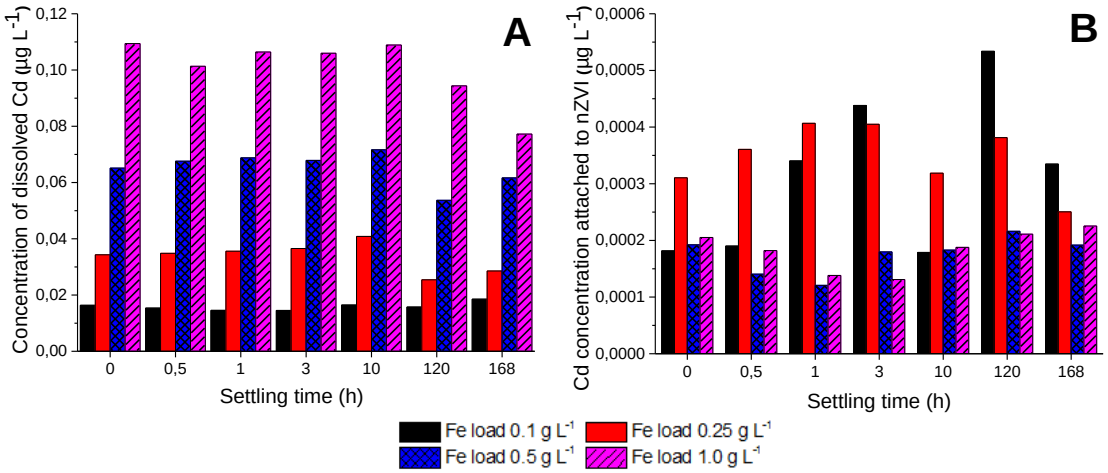


Figure 4.19: The influence of settling time on the concentration of dissolved Cd^{2+} (A) and Cd^{2+} attached to nZVI (B) in effluent wastewater treated with different Fe loads.

The total Cd concentration originally present in the effluent water was low (0.007 µg/L). It can be seen that with the increasing Fe loads, the dissolved Cd content was gradually increased at all the studied settling times (Figure 4.19A). The highest increase (15 times) was observed at time zero, when Fe load was 1.0 g/L of nZVI. This indicates that Cd present as a contaminant in nZVI is complexed by organic matter and released into the effluent water [221]. However, its concentration is low and is not environmentally relevant [14]. From Figure 4.19B it is further evident that concentrations of Cd^{2+} attached to nZVI were also very low, close to LOD (<0.0001 µg/L), and in general decreased with increasing Fe loads.

The results confirmed that SP-ICP-MS can be applied for studying the interactions of Cd^{2+} with nZVI in complex environmental matrices with very low Cd concentrations, enabling quantitative determination of Cd^{2+} concentration that interacts with nZVI. SP-ICP-MS is indispensable as a complementary tool to e.g. XPS or EDX techniques [226], which can provide information about the type of interactions, but cannot give quantitative data.

4.4 Single-Particle ICP-MS Characterization of Silver Nanoparticles Translocation in the *ex vivo* Human Placental Perfusion Model to Predict Potential Fetal Exposure

4.4.1 Characterization of AgNPs

The basic characteristics for both AgNP types (i.e. AgPEG and AgCOONa NPs), including total Ag mass concentration, dissolved Ag fraction in water, mass percent of surface coating, primary particle size and zeta-potential in water are presented in Table 4.7.

Table 4.7: Summary of AgNP characteristics. Results for Ag mass concentration (N=3), dissolved Ag fraction (N=2) and zeta potential (N=5) represent mean ± STD.

AgNP characteristic	**AgPEG**	**AgCOONa**
Ag mass concentration (mg/mL)	3.12 ± 0.06	5.30 ± 0.01
Dissolved Ag fraction (w/w %)	7.9 ± 0.4	0.31 ± 0.01
Percent of functionalization (w/w %)	64.1	16.3
Primary particle diameter	2-15 nm	5-15 nm
Zeta potential (mV) at pH 5	-10.7 ± 0.4	-32.5 ± 1.1

Besides revealing the primary particle size, TEM analysis further showed that AgPEG suspension contained three populations – very small Ag spheres of 2-8 nm, Ag spheres close to 7-15 nm, and a third minor population of very large and irregular particles in the 200-1000 nm size range, while AgCOONa NP suspensions displayed large assemblies of 100-500 nm containing multiple individual Ag ENM spheres of 5-15 nm (Figure 4.20).

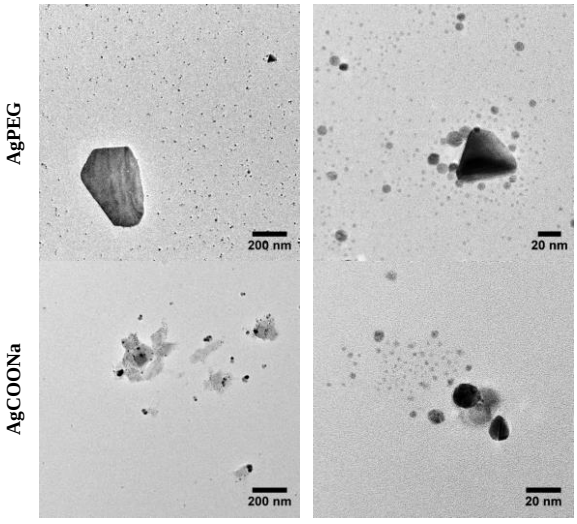


Figure 4.20: TEM images of AgPEG and AgCOONa NPs.

4.4.2 Stability of AgNPs in perfusion medium

In order to assess if AgNPs aggregate/agglomerate in PM, hydrodynamic size and size distribution of AgNPs in UPW and PM were determined by DLS (Figure 4.21). Size distributions obtained for AgPEG (multimodal distribution) and AgCOONa NPs (bimodal distribution) in water were in agreement with the TEM results (Figure 4.20). In PM, the formation of bigger particles was observed in particular for AgCOONa NPs, while only a slightly broader size distribution was measured for AgPEG NPs. Scattering entities in PM without NPs (around 10 nm and 500 nm) were most likely from the high levels of proteins present in the medium.

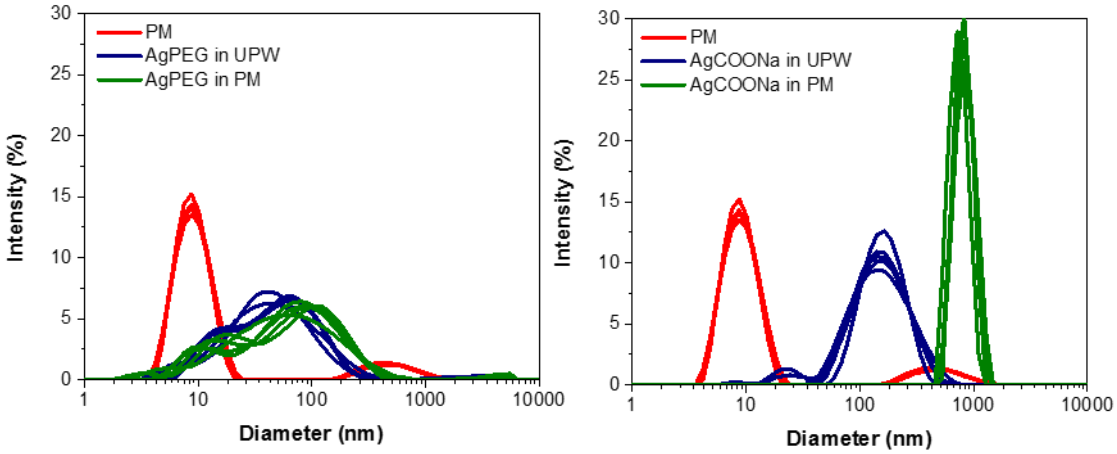


Figure 4.21: DLS hydrodynamic size measurements (intensity-based distributions) of PM alone and AgPEG (left) and AgCOONa NPs (right), dispersed in UPW or PM (1 mg/mL).

Aggregation of AgCOONa NPs in PM was further confirmed by SP-ICP-MS measurements of Ag mass concentrations ($>$ and $\leq$ 25 nm) and size distributions of AgCOONa and AgPEG NPs dispersed in UPW and PM in the same Ag concentrations as they were used in the perfusion experiment (Figure 4.22 and Table 4.8). While size distributions and mass concentrations of AgPEG NPs were similar in UPW and PM, AgCOONa NPs formed bigger particles (41 nm) in PM as in UPW (34 nm) resulting in bigger median size, higher mass concentration of AgNPs $>$ 25 nm and lower mass concentration of AgNPs $\leq$ 25 nm in PM.

The size distributions and mass concentrations of AgNPs, determined in suspension of AgPEG NPs, dispersed either in UPW or PM, do not differ significantly. In contrast, AgCOONa NPs dispersed in PM form bigger particles (41 nm) in comparison to UPW (34 nm), which results in bigger median size, higher mass concentration of AgNPs $>$ 25 nm and lower mass concentration of AgNPs $\leq$ 25 nm in PM.

According to the TEM analysis (Table 4.7, Figure 4.20), most of the particles are smaller than the selected size LOD (i.e. 25 nm), determined by SP-ICP-MS. Since this LOD excludes low-intensity events corresponding to the NPs smaller than 25 nm (Figure 4.22), calculated mass fractions of Ag $>$ 25 nm are relatively low: 1.5 % and 1.3 % for AgPEG NPs and 44 % and 79 % for AgCOONa NPs, dispersed in water and PM, respectively (Table 4.8). The low mass fraction of AgNPs $>$ 25 nm for AgPEG NPs corresponds to the relatively large population of particles smaller than 15 nm (according to TEM analysis). Furthermore, the Ag fraction that is below LOD cannot be considered

as the background which consists only of dissolved Ag, but includes also NPs smaller than 25 nm.

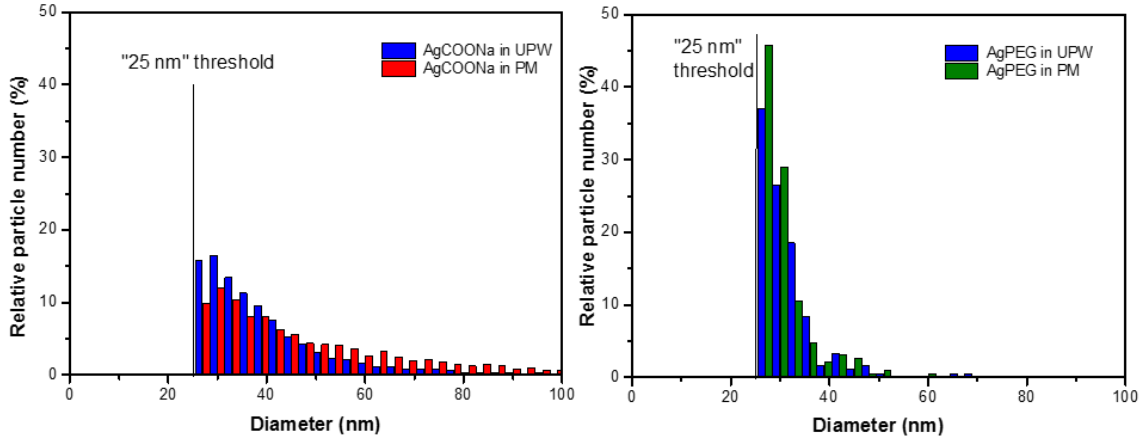


Figure 4.22: Size distributions of AgCOONa (left) and AgPEG NPs (right), freshly prepared in UPW and PM, determined by SP-ICP-MS.

Table 4.8: Mass concentrations of AgNPs > 25 nm and ≤ 25 nm and median NPs diameter, determined by SP-ICP-MS, for suspensions of AgPEG and AgCOONa NPs in UPW and PM. Results present mean values ± STD from two replicates.

AgNP type	Medium	Expected Ag mass conc.* (µg/mL)	Mass conc. of AgNPs> 25 nm (µg/mL)	Mass conc. of AgNPs≤ 25 nm+Ag ions (µg/mL)	Mass fraction of AgNPs> 25 nm** (%)	Ag mass recovery *** (%)	Median particle diameter (nm)
AgPEG	UPW	12.48	0.141 ± 0.004	9.05 ± 0.24	1.5	73.6	27.7 ± 0.3
	PM		0.121 ± 0.004	8.98 ± 0.14	1.3	72.9	27.4 ± 0.3
AgCOONa	UPW	39.26	13.45 ± 0.27	17.0 ± 0.7	44	77.6	34.3 ± 0.3
	PM		29.1 ± 2.0	7.65 ± 0.31	79	93.6	40.8 ± 0.4

*Based on ICP-MS analysis of digested stock suspensions
**Based on the total Ag mass concentration determined by SP-ICP-MS (≤ 25 nm + > 25 nm)
***Calculated as Ag mass concentration (≤ 25 nm + >25 nm) determined by SP-ICP-MS in comparison to the Ag mass concentration determined by ICP-MS in digested AgNPs samples.

Stability of 1 mg/mL AgNPs in PM at 4 °C was evaluated by DLS over an extended period of time to exclude potential NP aggregation and/or dissolution, which may occur due to the time lag between sample collection and SP-ICP-MS analysis in the different labs. Hydrodynamic diameter and size distribution of AgCOONa NPs was highly similar when measured immediately or after storage at 4 °C for 4 days. For AgPEG NPs only a slight decrease in Z-average mean was observed.

4.4.3 AgCl precipitation in perfusion medium

Precipitation of AgCl(s) is a process of concern in toxicological studies carried out under laboratory conditions at high Cl^- concentrations and high total Ag concentrations. In order to test if Ag ions can form AgCl precipitates with Cl ions present in PM, different

concentrations of ionic Ag (100 µg/mL, 10 µg/mL and 1 µg/mL) were prepared in PM and their size distributions measured by DLS immediately after their preparation (Figure 4.23) and 4 days later. AgCl precipitation in PM (additional peak in the size distribution with a peak maximum at around 100-200 nm) was only detectable by DLS when ionic Ag concentration was 10 µg/mL or higher (Figure 4.23). Even after prolonged incubation (4 days at 4 °C or RT), no AgCl particle formation was evident at 1 µg/mL Ag concentration since size distribution was similar over time. According to the determined dissolved Ag fraction of AgPEG and AgCOONa (Table 4.7), 1 µg/mL and 0.11 µg/mL of Ag ions is expected to be present on the maternal side for AgPEG (8 % of 12.48 µg/mL) and AgCOONa NPs (0.3 % of 39.26 µg/mL), respectively. Therefore, the formation of AgCl particles in PM over time is unlikely to occur in our placental perfusion studies.

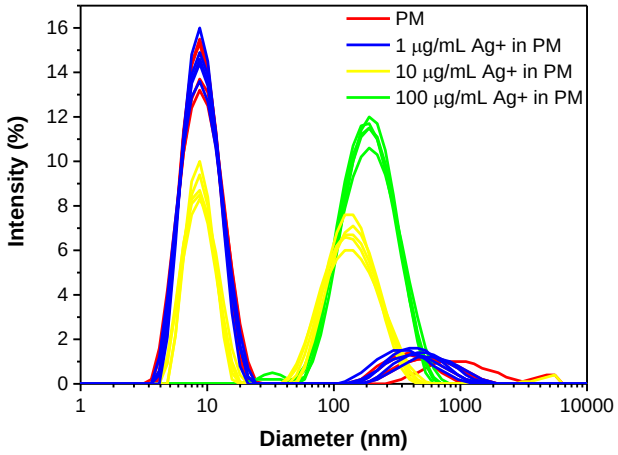


Figure 4.23: DLS hydrodynamic size measurements (intensity-based distributions) of PM and different concentrations of ionic Ag in PM (100 µg/mL, 10 µg/mL and 1 µg/mL). Samples were analyzed immediately after their preparation.

4.4.4 Translocation of AgNPs across the human placental barrier

SP-ICP-MS analysis was exploited to understand if AgNPs were able to cross the human placental barrier in an *ex vivo* placenta perfusion model. 40 µg/ml AgPEG NPs (12.5 µg/ml Ag) or 74 µg/ml AgCOONa (39 µg/ml Ag) were added to the maternal circulation, and changes of Ag mass concentrations of the fraction $>$ 25 nm and the fraction $\leq$ 25 nm (AgNPs $\leq$ 25 nm and dissolved Ag) were followed over the time of perfusion in maternal and fetal circulations (Figure 4.24). The concentrations of AgNPs were chosen as doses that were non-toxic to BeWo trophoblast cells after 6 h of exposure according to an MTS viability assay (Figure 4.25) but still relatively high to be able to see particle uptake and/or translocation and to mimic a potential worst-case exposure scenario. A higher dose of AgCOONa was applied since these NPs had a strong propensity to agglomerate in PM (Figure 4.21, Figure 4.22), which is expected to significantly reduce the placental transfer [80, 201].

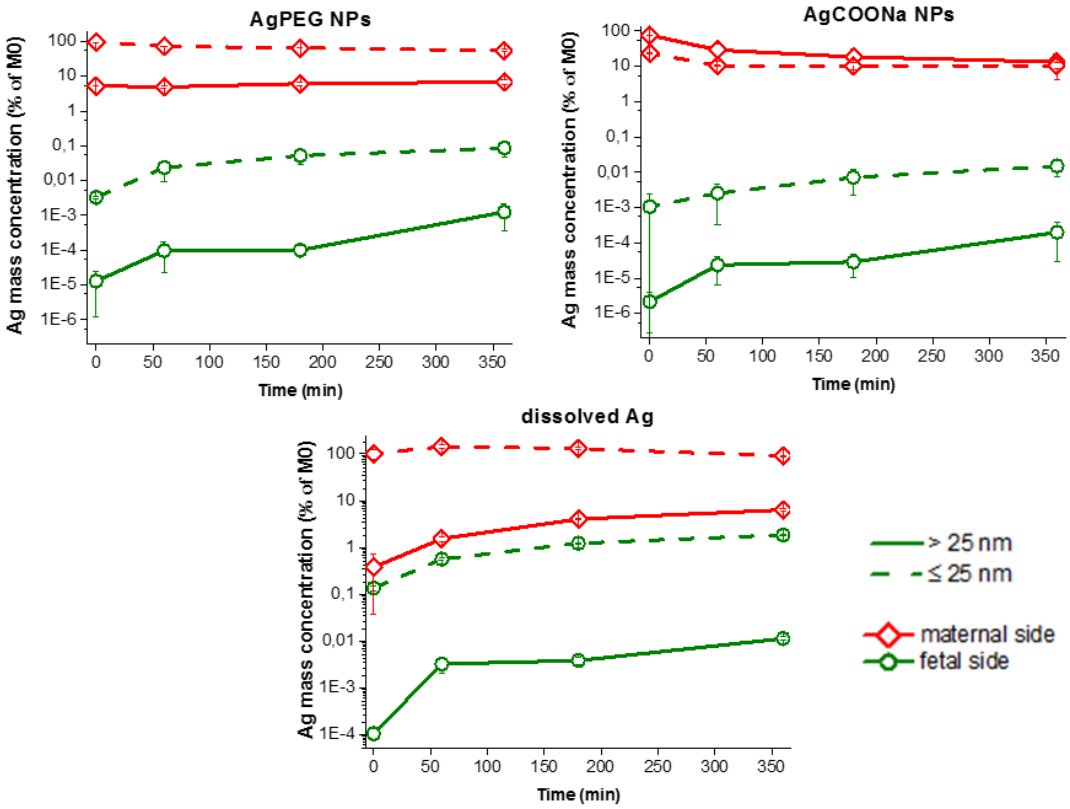


Figure 4.24: Perfusion profiles and transfer rates of Ag mass fraction >25nm (continuous line) and ≤ 25 nm (dashed line) during *ex vivo* human placental perfusion with AgPEG NPs, AgCOONa NPs and dissolved Ag, measured on the maternal (red colour) and fetal side (green colour) over a time period of 6 h. Data represent the mean ± STD of the independent experiments (N=2 for AgPEG NPs, N=3 for AgCOONa NP) and the mean ± STD from analytical repetitions of one experiment (N=1 for dissolved Ag).

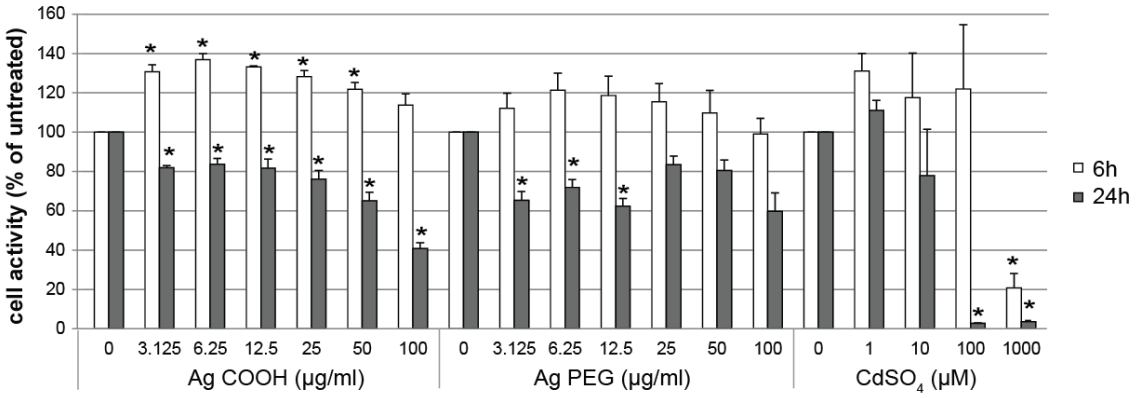


Figure 4.25: Effects of Ag NPs on BeWo cell viability. Cell viability of BeWo cells was assessed by MTS assay 6 and 24h after treatment with the indicated concentrations of NPs. $CdSO_4$ was used as a positive control. Optical density was measured at 490 nm and values are blank corrected as well as normalized to the untreated samples. Data represent mean ± SEM of 3 individual experiments.

After perfusion with AgCOONa or AgPEG NPs, Ag mass fraction > and ≤ 25 nm in the fetal circulation increased with the time of perfusion, but overall, only very low amounts of the maternally applied Ag doses were detected on the fetal side (Figure 4.24 A, B). On the maternal side, Ag mass concentrations of both fractions remained relatively stable for AgPEG NPs while for AgCOONa NPs, a strong decrease in both fractions was observed, indicating on a general "loss of material" over time in case of AgCOONa NPs. This is related to either their possible accumulation in the placental tissue or to their strong aggregation in PM, as already observed by DLS (formation of particles up to the micrometer size-range). Aggregates/agglomerates with such a big size were not detected with SP-ICP-MS since particles that contain a large mass of Ag due to low number of particles, settling in tubes or problems related to sub-sampling cannot be detected by a single particle method. Stronger aggregation observed for AgCOONa NPs in PM could be attributed to the carboxylate groups whose charge is compressed in the presence of high ionic strength in PM. Repulsive forces between AgCOONa NPs are then reduced, leading into the particle aggregation. Polyethylene glycol coating, on the other hand, provides strong steric stabilization for AgPEG NPs even in the presence of high ionic strength.

Although the transfer of AgNPs is very low, it might be that the strong accumulation in the placental tissue might damage placental functionality and thereby lead to indirect embryotoxicity. Even if the transfer is low teratogenic effects may occur in particular for a chronic exposure scenario since the fetus is particularly vulnerable to toxic compounds already at low levels. Previous studies which were conducted on animal models showed that exposure of rodents to AgNPs may [229] or may not [71] cause adverse effects on the embryo's health. However, there is recent evidence that AgNPs have been shown to cause developmental neurotoxicity in human embryonic neural precursor/stem cells [230, 231].

The percentage of Ag particles > 25 nm that crossed the placental barrier after 6 h of perfusion was 0.0013 ± 0.0009 % for AgPEG NPs (N=2) and 0.00020 ± 0.00017 % for AgCOONa NPs (N=3), suggesting that AgPEG NPs were around 6 times more efficiently transported across the placenta than AgCOONa NPs. AgPEG and AgCOONa NPs used in our study mostly differ in surface properties which can lead into different dispersion behavior of AgNPs in PM, affecting their size through potential aggregation/agglomeration. Lower translocation of AgCOONa can be therefore explained by their strong aggregation in PM.

In addition to quantifying the Ag mass concentrations of different size fractions, SP-ICP-MS analysis was also applied to obtain information on the number-based particle size distribution (Figure6).

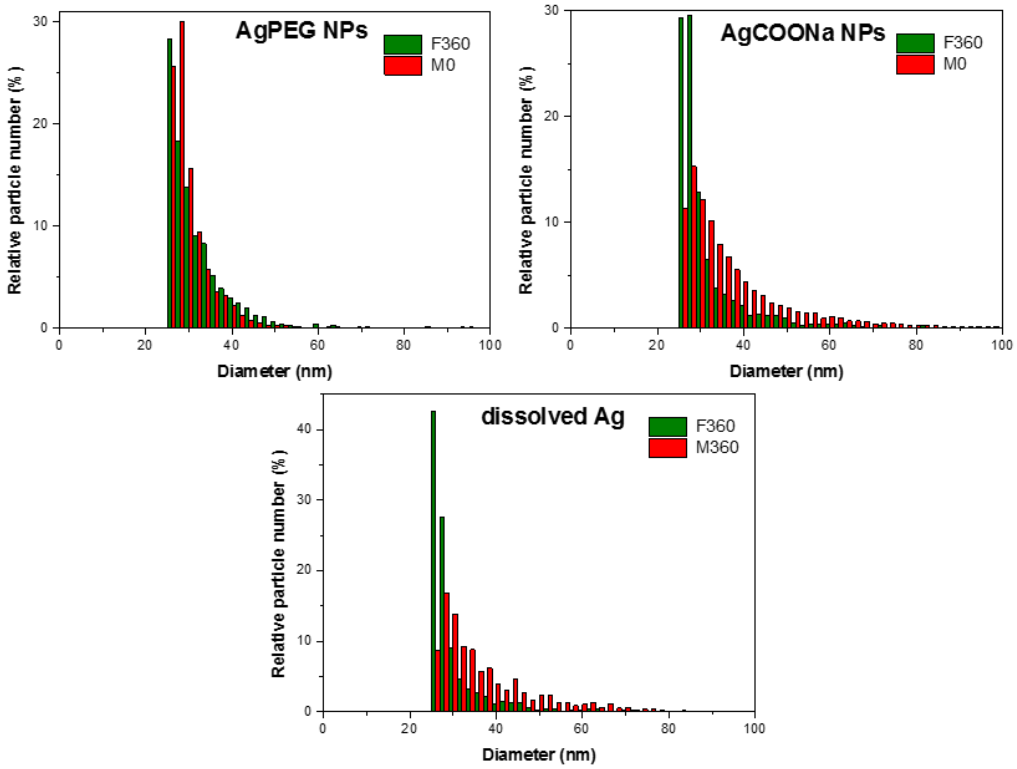


Figure 4.26: Size distributions of NPs formed on the maternal side (red colour) and fetal side (green colour) in the perfusion experiments with AgPEG NPs, AgCOONa NPs and dissolved Ag.

For perfusion experiments with AgCOONa NPs, smaller particles were present in the fetal circulation at the end of perfusion (median particle diameter 27.3 nm) as compared to the maternal side at the beginning of perfusion (32.9 nm). In contrast, there was no significant difference in the particle size distribution of AgPEG NPs between the maternal (27.8 nm) and the fetal side (27.1 nm).

Moreover, size-dependent translocation is especially reflected in more efficient translocation of Ag fraction $\leq$ 25 nm (containing AgNPs $\leq$ 25 nm and/or Ag ions) with 0.0865 $\pm$ 0.0381 % for AgPEG NPs and 0.0151 $\pm$ 0.0077 % for AgCOONa NPs. It has been already observed for different types of NPs, independent of the species origin (rodent, human) or the complexity of the model (*in vivo, ex vivo, in vitro*), that the number of transferred NPs was higher for smaller compared with larger particles [79].

In an attempt to better understand if AgNPs translocation did occur in the form of particulate Ag or due to particle dissolution, transfer of ions and re-precipitation of AgNPs at the fetal side, a perfusion with $AgNO_3$ was performed (Figure 4.24C). Dissolved Ag could exist on the maternal side either due to the possible particle dissolution in PM over time or due to the AgNP suspensions that might already contain dissolved Ag (8 % of AgPEG and 0.3 % in AgCOONa – Table 4.8). Ag ions were able to pass the placental barrier since an increase of the Ag mass fraction $\leq$ 25 nm was measured in the fetal circulation over time. Interestingly, Ag particles $>$ 25 nm appeared in the maternal as well as fetal circulation and their concentrations increased gradually throughout the perfusion

study. The mass concentration of AgNP > 25 nm on the fetal side was 0.0120 µg/mL after 6 hours of perfusion. This value was in the same concentration range as the mass concentration of AgNPs > 25 nm that was observed on the fetal side after perfusion with AgNPs (0.060 ± 0.047 µg/mL for AgPEG (N=2) and 0.081 ± 0.071 µg/mL for AgCOONa (N=3)). Moreover, in the perfusion experiment with $AgNO_3$, the size distribution of the newly precipitated particles on the fetal side after 6 hours (26.5 nm) was similar to the size distribution of particles detected on the fetal side after AgPEG (28.2 nm) or AgCOONa NPs (27.3 nm) were added (Figure6). The size distributions of the particles on the maternal and fetal side after 6 hours of perfusion with $AgNO_3$ indicate that a significant number of particles was formed on both sides. Bigger particles on the maternal side are due to the fact that dissolved Ag is present longer and in a higher concentration on the maternal side than on the fetal side.

The concentrations and size distributions of the particles detected on the fetal side after the addition of dissolved Ag into the maternal circuit were comparable to the particles when AgNPs were added. This demonstrates that particles on the fetal side observed in the perfusion with AgNPs are not necessarily the result of translocated pristine AgNPs but could also be Ag precipitates, formed from the dissolved Ag that crosses the placental barrier. Although no particle formation was observed in PM which contained relevant ionic Ag concentrations (see paragraph 4.4.3.), Ag precipitation can occur in the perfusion experiment most probably due to the presence of other proteins which could be released to PM from the placental tissue. For instance, amino acids containing thiol groups (i.e. cysteine and methionine) have high affinity to ionic Ag, forming Ag(I)–thiol complexes [232]. Bolea et al. [189] further showed that the process, where dissolved Ag released from AgNPs and associated with the proteins present in the culture medium, is accelerated by the presence of the cells. However, in placenta no particle formation (AgNPs > 25 nm) occurs when dissolved Ag is applied.

4.4.5 Comparison of Ag translocation determined by SP-ICP-MS or conventional ICP-MS

Total Ag mass concentrations on the maternal and fetal side with the time of perfusion were also determined by conventional ICP-MS analysis and compared to the results obtained by SP-ICP-MS (Ag mass fraction > + ≤ 25 nm) (Figure7). There was no significant difference (t test, $p < 0.01$) between the Ag concentrations determined by both methods for the perfusion studies with AgCOONa NPs. However, in case of AgPEG NPs, about 3 times higher Ag concentrations were detected in the maternal perfusates by ICP-MS compared to SP-ICP-MS. The possible reasons for Ag losses might lie in the SP-ICP-MS method itself. Namely, quantification of the fraction ≤25 nm which prevails, especially in case of AgPEG, was less accurate since the SP-ICP-MS analyses (dilution factor, calibration curve range) were not optimized for that fraction. Another reason are different surface properties of AgNPs that can cause their settling and/or sticking on the tubes and/or in ICP-MS system, leading into larger losses of the material. AgPEG NPs are obviously more subjected to these changes, which has been observed already for AgNPs dispersed in PM (Table 4.8), where 73 % of AgPEG NPs and 94 % of AgCOONa NPs was detected by SP-ICP-MS.

The percentage of total Ag that crossed the placental barrier (measured on the fetal side after 6 h of perfusion) was 0.0174 ± 0.0208 % for AgCOONa and 0.0395 ± 0.0182 % for AgPEG NPs when determined by conventional ICP-MS and 0.0153 ± 0.0078 % for AgCOONa and 0.0877 ± 0.0390 % for AgPEG NPs when determined by SP-ICP-MS.

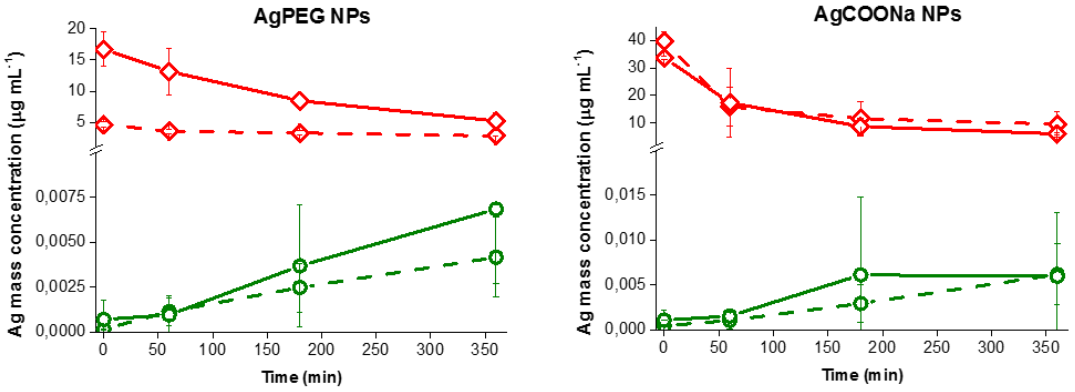


Figure 4.27: Comparison of perfusion profiles and transfer rates of Ag during *ex vivo* human placental perfusion with AgPEG NPs and AgCOONa NPs, determined by SP-ICP-MS (dashed lines) and conventional ICP-MS (continuous lines). Presented are Ag concentrations measured on the maternal (red colour) and fetal side (green colour) of the placenta over a time period of 6 h. Data represent the mean ± STD of the independent experiments (N=2 (SP-ICP-MS) or N=3 (ICP-MS) for AgPEG NPs, N=3 (SP-ICP-MS) and N=2 (ICP-MS) for AgCOONa NPs).

4.4.6 Accumulation of AgNPs in the placental tissue

Although placental Ag transfer was very low, Ag mass concentration in the maternal circulation was declining in particular for AgCOONa NPs (Figure 4.24). In order to investigate the degree of AgNPs accumulation in the placenta, tissue samples were enzymatically treated to release NPs from the tissue without altering their properties. Enzymatic treatment of the tissue samples with the use of the stable and highly active enzyme Proteinase K, that is able to completely digest complex organic matrices by degrading proteins into amino acids, has been shown to be effective for quantitative analysis of AgNPs in a chicken meat matrix [114].

Ag mass fraction > and ≤ 25 nm were measured in placental tissues after 6 h of perfusion with AgPEG NPs, AgCOONa NPs or $AgNO_3$ (Figure8). For AgCOONa NPs, a much higher Ag fraction > 25 nm of the applied dose did accumulate in the placenta (4.1 %) as compared to AgPEG NPs (0.02 %). The mass concentration of the Ag fraction ≤ 25 nm for AgCOONa NPs (8 %) was also higher as compared to AgPEG NPs (2 %). Overall, Ag mass fraction >25 nm presented 36 % and 0.7 % of the total internalized Ag mass concentration determined by SP-ICP-MS (≤ 25 nm + > 25nm) for AgCOONa NPs and AgPEG, respectively, which is similar to the mass fractions determined for pristine AgNPs, suspended in UPW (see Table 4.8). When $AgNO_3$ was added to the maternal circulation, predominantly Ag ions and/or small AgNPs were taken up by the placental tissue (17 % for fraction ≤25 nm, 0.03 % for AgNPs > 25 nm).

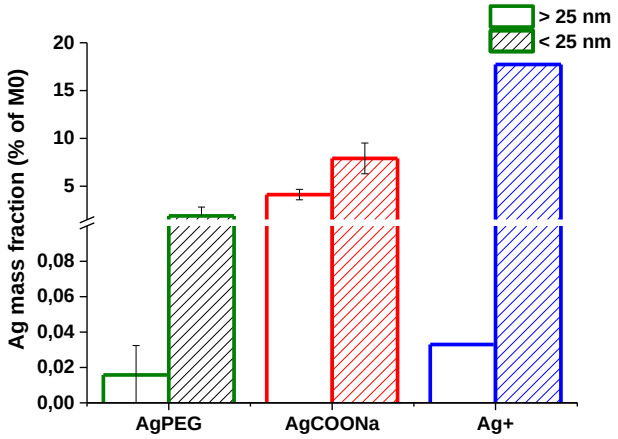


Figure 4.28: Mass concentration of Ag fraction > and ≤ 25 nm, determined by SP-ICP-MS in enzymatically treated tissue samples, from perfusion with AgPEG NPs, AgCOONa NPs and $AgNO_3$. Ag mass concentrations in placenta collected after 6 h of perfusion are normalized to the applied Ag concentration measured in M0 samples by conventional ICP-MS. Data represent the mean ± STD of the independent experiments (N=2 for AgPEG NPs, N=2 for AgCOONa NPs, N=1 for $AgNO_3$).

Higher uptake of Ag fraction ≤ 25 nm compared to AgNPs > 25 nm when perfusion was performed with both AgNP types, and higher percentage of the total applied Ag dose in the placenta when perfusion was performed with dissolved Ag suggests that Ag in its ionic form is more bioavailable than in particulate form, similar to other reports [78, 89]. A possible explanation for the high accumulation of dissolved Ag in the human placenta may be the presence of high levels of the metal-binding protein metallothionein in this tissue [233]. It has been already shown that prenatal exposure of rodents to Ag in both ionic and nanoparticle forms increases the levels of Ag in offspring tissues and induces oxidative stress, with the ionic form being more toxic [72]. Translocation and toxicity of particulate Ag can even be induced by Ag ions that are released from the particle surface [234]. Given its toxicity, Ag^+ should therefore also be taken into account in evaluating the toxicity of AgNPs in placental tissue.

When comparing AgCOONa NPs sizes determined on the maternal and fetal side with those in placental tissue after 6 h of perfusion (Figure9), we observed slightly larger AgCOONa particles (aggregates/agglomerates) on the maternal side (30.8 nm) and in the placental tissue (34.0 nm) compared to the smaller particles on the fetal side (27.4 nm), indicating that preferentially small particles crossed the placental barrier, while larger ones (aggregates/agglomerates) accumulated in the tissue. In case of AgPEG NPs, there was no difference in median diameters of particles on the maternal side (29.0 nm), in placental tissue (27.3 nm) and on the fetal side (28.2 nm) after 6 h of perfusion. However, in comparison to pristine AgNPs suspended in UPW (Table 4.8), no dissolution or aggregation of AgNPs accumulated in placenta was observed after 6 hours of perfusion (similar mass fraction of Ag ≤ 25 nm: 99 % for AgPEG and 66 % for AgCOONa NPs, and similar particle size: 27.3 nm for AgPEG NPs and 34.0 nm for AgCOONa NPs).

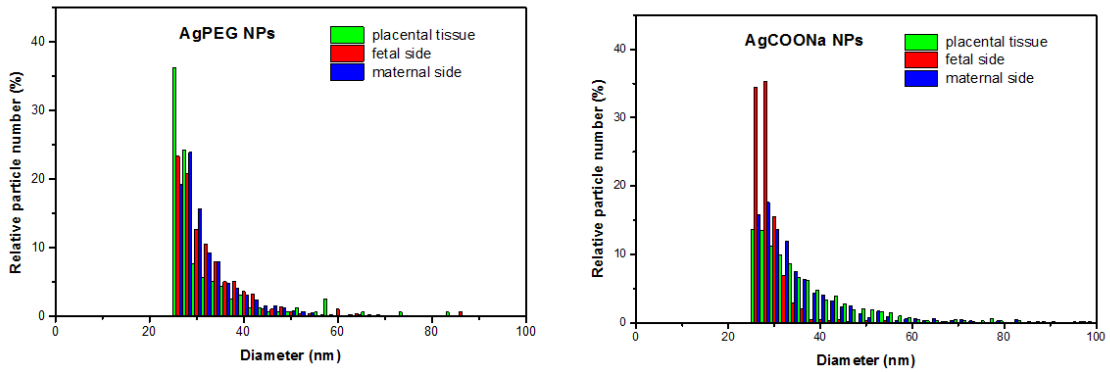


Figure 4.29: Comparison of size distributions of AgPEG and AgCOONa NPs, determined by SP-ICP-MS in the samples on maternal, fetal side and in placenta tissue after 6 h of perfusion.

4.4.7 Comparison of translocation data with other studies

Previously published work has investigated the translocation of AgNPs in rodents, performed mostly in *in vivo* studies. The translocation levels of Ag, measured by ICP-MS in the tissues of pups as the total Ag mass concentrations and expressed as the percentages of the administered dose, ranged from 0.008–0.009 % [83], 0.036 % [73], 0.085–0.147 % [82], 0.097 % [235] to 0.2-0.5 % [84], while the percentage of Ag accumulated in placenta varied between 0.2 % [83] and 0.04-1.3 % [84]. When comparing our translocation data in relation to the previous data on placental AgNPs transfer important differences, such as different placental transfer models applied (*in vivo* transfer studies in rodents versus *ex vivo* perfusion of human placenta), different properties of AgNPs used (various dose, size and coatings) and different ways of AgNPs administrations have to be taken into account. This is important since previous results were all from animal models where the placental structure and function is significantly different. However, translocation levels of AgNPs reported in the mentioned studies are in the same range to those observed in our study (0.015-0.088 %, calculated as Ag mass fraction $>$ and $\leq$ 25 nm), while the percentage of translocated dissolved Ag was for about 2 orders of magnitude higher. Moreover, the percentage of Ag accumulated in placenta was about 10 times higher in our study (3.6 -12 %) than those reported before. The difference is most probably related to the different ways of AgNPs administration to the placenta and fetus. In *in vivo* experiments where AgNPs were intravenously or orally dosed to the rodents, NPs were not distributed only to the placenta but also to the other organs of the adult rodent, mainly in the liver and kidneys [236]. This demonstrates that the results obtained from the studies using rodents must be interpreted carefully with respect to the relevance to humans. Our study which used *ex vivo* human placental perfusion model therefore represents an important supplement for the investigation of AgNPs translocation and accumulation in human placenta.

4.5 Use of Alkaline or Enzymatic Sample Pre-treatment Prior to Characterization of Silver Nanoparticles in Human Tissue by Single Particle ICP-MS

4.5.1 Investigation of potential matrix effects on calibration

First, we wanted to evaluate whether ionic Ag standards (for the determination of the ICP-MS response) and AuNPs (for determination of the transport efficiency) should be prepared in the same matrix as the digested tissue samples or whether they can be prepared in UPW. Therefore, the transport efficiency based on the particle frequency and particle size method was determined in UPW, 1 % TMAH (representing the matrix for alkaline treatment) and in 30 times diluted enzyme solution (representing the matrix for enzymatic treatment followed by approximately 30 times dilution of the enzymatic digest with UPW), by diluting AuNP and ionic Au standards in the relevant matrices (Table 4.9). ICP-MS response for ionic Au and Ag was determined by measuring a blank (UPW or relevant matrix) and different concentrations of ionic Au (0.2, 0.5 and 1.0 µg/L) or Ag standards (0.2, 0.5, 1.0 and 2.0 µg/L), respectively.

Table 4.9: Comparison of the transport efficiencies (calculated with particle frequency and particle size method by diluting AuNPs and ionic Au standards in relevant matrices, respectively) and ICP-MS responses for ionic Ag and ionic Au standards with related R^2 values prepared in relevant matrices. Results, which represent the values measured on the same day, were comparable to a second measurement on another day.

	Transport efficiency (%)		**Ionic Au**		**Ionic Ag**	
Matrix	**Particle frequency method**	**Particle size method**	**ICP-MS response (cps/µg/L)**	**R^2**	**ICP-MS response (cps/µg/L)**	**R^2**
UPW	5.8	6.7	42,361	0.9971	83,390	0.9978
1 % TMAH	7.1	11.2	64,920	0.9999	67,315	0.9958
Enzyme solution	7.8	8.0	36,787	0.9996	36,734	0.9785

Similar transport efficiencies (6-8 %) were determined with the two methods, particle frequency and particle size method, independently of the used matrix (17). The only exception was observed for the transport efficiency (11 %) determined by the particle size method in the 1 % TMAH matrix. This was related to the 53 % higher ICP-MS response for ionic Au in 1 % TMAH in comparison to UPW and enzyme solution. Possibly, TMAH has a stabilizing effect for the Au ions and reduced the loss of Au ions in the sample introduction system. However, TMAH does not have this effect for AuNPs and consequently, the transport efficiency (as it is based on the transport efficiency for ions) was overestimated.

The ICP-MS response for ionic Ag solution in 1 % TMAH and enzyme solution decreased in comparison to ionic Ag solution in UPW by 19 % and 56 %, respectively (Table 4.9). Moreover, the Ag responses showed good linearity ($R^2 > 0.99$) in all three matrices. The formation of particles from the ions in these matrices was observed. For the same mass concentration of the analyzed Ag ion solution (33 ng/L), 21 ± 18 particles were detected in 1 % TMAH and 29 ± 9 in enzyme solution during 3 min of SP-ICP-MS analysis. The particle formation could result in a lower ICP-MS response by reduction of the Ag ion concentration. A 50 % underestimation of the ICP-MS response would lead to a 50 %

underestimation of the particle and background mass concentration as well as a 25 % overestimation of the AgNP diameter. Consequently, matrix matching was not applied and the ICP-MS response determined for ionic Ag in UPW. For ionic Au no particle formation was observed.
Finally, transport efficiencies and ICP-MS responses determined in UPW were applied for sizing and quantification of AgPEG40 NPs suspended in UPW, 1 % TMAH and enzyme solution (30 times diluted) (Table 4.10). Stock suspension of AgPEG40 NPs was diluted 10^6 times in UPW or the relevant matrices to a final mass concentration of 20 ng/L. This concentration resulted in a sufficient number of detected particles without exceeding the 10 % contribution limit for multiple events as described above. As particle size and particle frequency method led to a similar transport efficiency, only results based on the particle size method are presented. As can be seen, particle mass concentrations and median particle sizes obtained for AgPEG40 NPs suspended in UPW and AgPEG40 NPs spiked to 1 % TMAH or enzyme solution were not significantly different (t-test) (Table 4.10, Figure 4.30).

Table 4.10: Ag mass concentration of NPs and background and median size for AgPEG40 NPs prepared in UPW and matrices relevant to each treatment type at a mass concentration of 20 ng/L (N=2). Transport efficiency (with the use of the "particle size method") and ICP-MS response were determined in UPW.

Matrix in which NPs were suspended	**Mass conc. of AgNPs (ng/L)**	**Ag mass conc. of background (ng/L)**	**Ag mass recovery* (%)**	**Median particle size (nm)**
UPW	10.5 ± 0.3	1.9 ± 0.8	65 ± 1	34.2 ± 0.0
1 % TMAH	12.3 ± 0.4	<LOD[1]	62 ± 2	33.5 ± 0.2
Enzyme solution	13.7 ± 0.3	<LOD[2]	68 ± 1	34.5 ± 0.0

*Calculated from the total Ag mass concentration (NPs + background) determined by SP-ICP-MS in comparison to the Ag mass concentration provided by the manufacturer (20 mg/L; diluted 10^6 times to 20 ng/L)
[1]LOD in 1 % TMAH = 11 ng/L
[2]LOD in enzyme solution = 42 ng/L

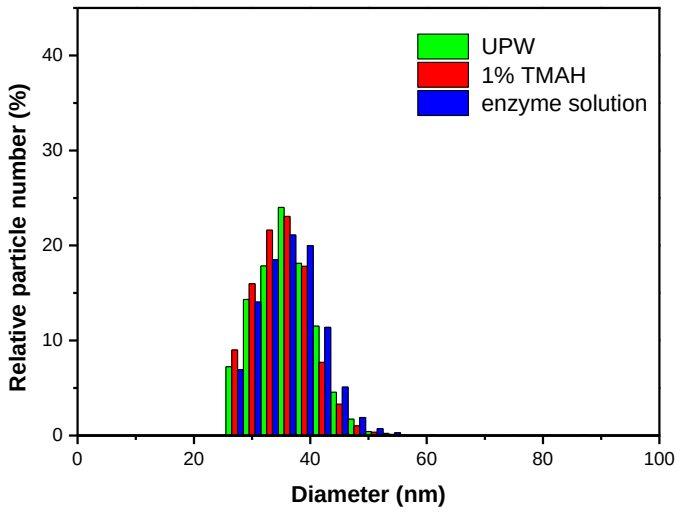


Figure 4.30: Particle size distribution (bin size 2 nm) obtained by spICPMS for AgPEG40 NPs suspended in UPW and AgPEG40 NPs spiked to 1 % TMAH or enzyme solution.

4.5.2 Comparison of spike recoveries and AgNP size distributions after enzymatic and alkaline treatment of placenta tissues

In order to investigate how the alkaline and enzymatic treatment influences the mass concentrations and size distribution of AgNPs in placental tissue, 100 mg of tissue homogenates from a control perfusion experiment (placenta samples were collected before the start of the perfusion experiment) were spiked with 10 µL of diluted AgNP stock suspensions with a concentration of 329 µg/mL for AgCOONa NPs and 134 µg/mL for AgPEG NPs. The achieved tissue concentrations were 26.8 mg/kg_{tissue} and 66.0 mg/kg_{tissue} for AgPEG and AgCOONa NPs, respectively. These concentrations were selected to be approximately the same as the AgNPs concentrations used in the perfusion experiments. All samples were prepared in duplicates. After spiking, samples were homogenized by the use of a vortex mixer for 1 minute to assure a proper mixing of tissue homogenate and AgNPs before the enzymatic or alkaline treatment. Suspensions of AgNPs at the same Ag concentrations were prepared in UPW as well. Prior to the SP-ICP-MS analysis, spiked samples and suspensions of AgNPs in UPW were diluted in the same way in order to make a comparison between the determined mass concentrations and sizes possible.

The particle size distributions of the two types of AgNPs, AgPEG and AgCOONa, in enzymatically treated tissue and UPW were similar (Fig 4.31 and 4.32, left graphs), showing that enzymatic digestion did not significantly affect the particle sizes, *e.g.* through aggregation or dissolution. The determined median particle diameters were around 27 nm for AgPEG and 34 nm for AgCOONa, and not statistically different before and after enzymatic treatment for both particle types (Table 4.11). Higher (total) Ag mass recoveries were obtained in an enzymatically treated tissue (98 and 124 %) in comparison to UPW (44 and 78 %) for AgPEG and AgCOONa, respectively, which indicated a stabilizing effect of the enzymatic digest. The fraction of AgNPs > 25 nm relative to the total Ag mass concentration was not affected by the enzymatic treatment and remained 1 % for AgPEG and 40 % for AgCOONa as in the case of dilution in UPW.

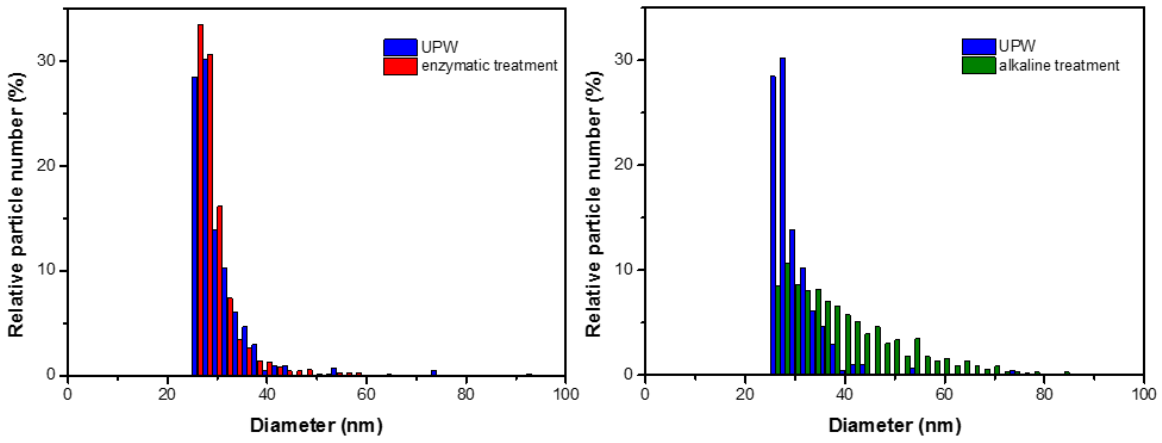


Figure 4.31: Particle size distribution (bin size 2 nm) obtained by spICPMS for AgPEG NPs in placental tissue after enzymatic (left; red histogram) or alkaline treatment (right; green histogram). The particle size distribution for AgPEG NPs in UPW is presented for comparison (blue histograms).

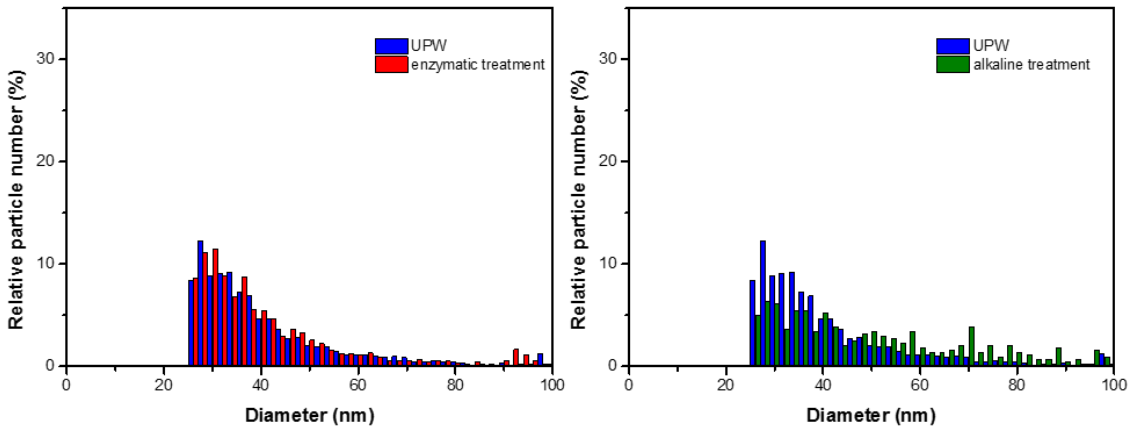


Figure 4.32: Particle size distribution (bin size 2 nm) obtained by spICPMS for AgCOONa NPs in placental tissue after enzymatic (left; red histogram) or alkaline treatment (right; green histogram). The particle size distribution for AgPEG NPs in UPW is presented for comparison (blue histograms).

Table 4.11: Ag mass recovery, mass fraction of AgNPs > 25 nm and median particle size for AgPEG and AgCOONa in UPW (N=4) and in placental tissue after enzymatic and alkaline treatment (N=2) (mean ± STD).

AgNP type	**Treatment**	**Ag mass recovery* (%)**	**Mass fraction of AgNPs > 25 nm** (%)**	**Median particle size (nm)**
AgPEG	UPW	44 ± 7	1.0 ± 0.5	27.3 ± 0.1
	Enzymatic treatment	98 ± 6	1.5 ± 0.7	27.5 ± 0.1
	Alkaline treatment	118 ± 2	93 ± 1	35.5 ± 0.5
AgCOONa	UPW	78 ± 8	40 ± 4	34.1 ± 0.4
	Enzymatic treatment	124 ± 1	37.0 ± 5	34.2 ± 0.3
	Alkaline treatment	133 ± 13	115 ± 17	45.2 ± 2.3

*Calculated from the total Ag mass concentration (NPs + background) determined by SP-ICP-MS in comparison to the Ag mass concentration expected in the spiked tissue samples (calculated based on the Ag mass concentration of the spiking suspension, spiking volume and dilution factors)
**relative to the total Ag mass concentration (> 25 nm and ≤ 25 nm) determined by SP-ICP-MS

After alkaline treatment, the particle size distributions of the two types of AgNPs, AgPEG and AgCOONa, showed the occurrence of larger NPs in comparison to UPW (Fig. 4.31 and 4.32, right graphs). The determined median particle diameters increased from around 27 nm to 36 nm for AgPEG and from 34 nm to 45 nm for Ag COOH (Table 4.11). Higher (total) Ag mass recoveries were obtained in alkaline treated tissue (118 % for AgPEG and 133 % for AgCOONa) in comparison to UPW (44 % for AgPEG and 78 % for AgCOONa). The fraction of AgNPs > 25 nm relative to the total Ag mass concentration increased from 1 % in UPW to 93 % after alkaline treatment for AgPEG and from 40 % to 115 % for AgCOONa. These findings indicated agglomeration/aggregation of both types of AgNPs due to the alkaline treatment of the tissue. A further possible mechanism could be the formation of large AgNPs from ionic Ag.

In the only study that used TMAH solubilization followed by SP-ICP-MS analysis for releasing of AgNPs from biological matrices so far, no significant (> 5 nm) change of the

size distribution of 100 nm AgNPs with PVP coating was observed after alkaline treatment of ground beef (Ag spiking concentration of 0.019 mg/kg wet weight) [103]. A "nearly identical" size distribution was described for a mixture of 60 nm and 100 nm AgNPs. The presented histograms indicated a slight shift of the size distribution to larger size values after alkaline treatment.

In order to investigate if alkaline or enzymatic treatments caused particle formation from ionic Ag, 10 µL of 10 µg/mL ionic Ag was spiked to 100 mg of control tissue homogenates (50 mg of tissue), which results in 2 mg of Ag^+/kg_{tissue}, and subjected to the alkaline and enzymatic treatment. This concentration was selected to be approximately the same as the expected Ag tissue concentration if all Ag, which was dosed to the perfusion experiment (1 mg/L), accumulates in the analysed tissue (4 mg of Ag^+/kg_{tissue}). 1 mg/L of ionic Ag was also prepared in the matrices relevant to each treatment type, *i.e.* 1 % TMAH or enzyme solution (30 times diluted) and measured by SP-ICP-MS, applying the same dilution factor before the analysis (20,000 times). The number of detected particles, Ag mass concentration (> 25 nm and ≤ 25 nm) and median particle size observed in 3 min long run are presented in Table 4.12.

Table 4.12: Ag mass concentration, median particle size and the number of particles, detected by SP-ICP-MS analysis, for the enzymatically or alkaline treated control tissue samples, 1 % TMAH and enzymatic solution, spiked with 1 mg/L of ionic Ag (20,000 times diluted before analysis to 50 ng/L). Results represent the average value with the STD between two replicates.

Treatment type	**Matrix**	**Ag mass conc. (> 25 nm) (ng/L)**	**Ag mass conc. (≤ 25 nm) (ng/L)**	**Number of particles**	**Median particle size (nm)**
Alkaline	spiked control tissue	32.8 ± 4.2	17.7 ± 4.8	8,383 ± 907	33 ± 2
	TMAH	0.235 ± 0.128	24.7 ± 1.5	50 ± 13	29 ± 1
Enzymatic	spiked control tissue	0.320 ± 0.002	46.7 ± 5.4	88 ± 52	26 ± 0
	enzymatic solution	0.055 ± 0.000	31.3 ± 0.6	38 ± 4	25 ± 0

As it can be seen, a significant number of particles (8,383) was formed after alkaline treatment of the spiked placental tissue sample with a median particle size of 33 nm, while 50 particles with 29 nm median size were detected for the same concentration of ionic Ag in 1 % TMAH. Ag precipitation during alkaline treatment apparently occurs due to the components present in the tissue or PM and not only because of the use of 1 % TMAH. Gomes et al. [237] observed Ag particle formation in alkaline conditions in the presence of alkoxides as reducing agents, formed from any molecule containing a hydroxyl (OH) group. In our case, alkaline TMAH and the presence of the tissue that contains proteins with –OH groups might create an ideal environment for the formation of particles. Enzymatic treatment on the other hand did not cause a significant formation of particles, neither in the treated placental tissue nor in the enzymatic solution alone.

From the data presented in Table 4.12 it can be concluded that Ag precipitation contributed, at least to a certain extent, to the above-described results for AgPEG and AgCOONa in the alkaline treated tissue. It was also demonstrated that TMAH itself does not lead to a significant particle formation when there is no tissue present. In the study by Gray et al. [103], no particle formation from ionic Ag was observed. The spiking concentrations for ionic Ag were 50 times lower (0.04 mg Ag^+/kg_{tissue}) compared to the concentration used in our study (2 mg $Ag+/kg_{tissue}$). The ratio between TMAH volume and tissue mass of both studies was similar. The method described in [103] adds 10 mL of TMAH to 0.5 g tissue, resulting in a final TMAH concentration of 20 %. We use 0.1 g tissue (in 0.2 g tissue homogenate) and add 2 mL of TMAH and 0.3 mL UPW, resulting

in a final TMAH concentration of 20 % as well. Further work is required to understand the observed differences of the two studies.

4.5.3 Quantification and characterization of AgNPs accumulated in human placenta in the *ex vivo* human placental perfusion model

Enzymatic treatment of the placental tissue followed by SP-ICP-MS analysis was proven to be effective for the characterization and quantification of AgCOONa and AgPEG NPs, which were spiked to placental tissue samples. However, accumulation of NPs under real exposure scenarios involves many dynamic interactions between NPs, matrix and biological processes of the target organism [111]. Therefore, for testing if the same procedure was capable of extracting AgNPs accumulated under a realistic exposure scenario, placental tissues from human *ex vivo* placenta perfusion experiments were investigated. The median sizes of AgPEG NPs and AgCOONa NPs accumulated in the placental tissue after 6 h of perfusion were determined by SP-ICP-MS and calculated to be 26.7 ± 0.4 nm and 33.7 ± 0.3 nm, respectively. Mass fractions of AgNPs > 25 nm were 1.1 ± 0.1 % and 29 ± 1 % for AgPEG and AgCOONa, respectively. Median sizes, mass fractions of AgNPs > 25 nm as well as size distributions (Figure3) of both AgNP types accumulated in placenta after 6 h of perfusion were comparable with properties of AgNPs determined in spiked placental tissues. This indicates that either no dissolution/aggregation of AgNPs occurs during their accumulation in human placenta or that SP-ICP-MS cannot provide any information about the agglomeration state of the NPs in the tissue as it is altered by the sample preparation procedure.

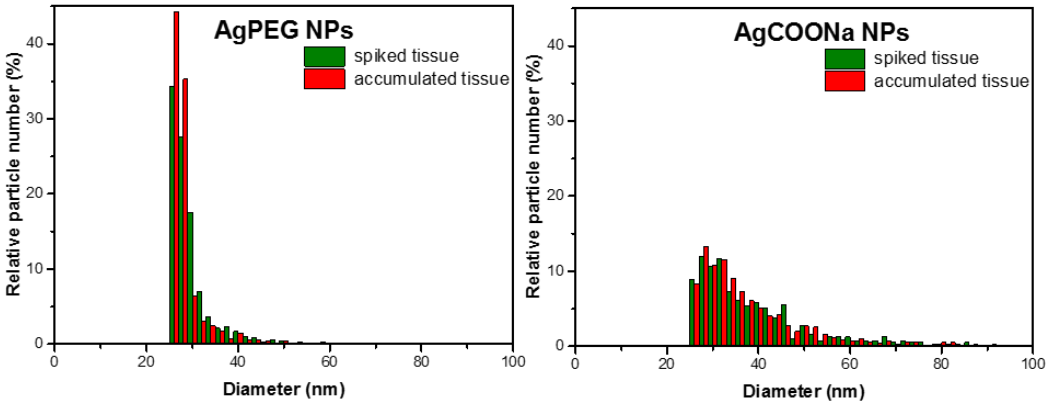


Figure 4.33: Particle size distribution (bin size 2 nm) obtained by spICPMS for AgPEG NPs and AgCOONa NPs in spiked placental tissue (green histogram) and placental tissue in which AgNPs accumulated after 6 h of perfusion (red histogram). All placental tissues were enzymatically treated.

Furthermore, Ag mass concentrations of AgNPs accumulated in placental tissue obtained by SP-ICP-MS after enzymatic treatment were compared with the concentrations obtained by conventional ICP-MS after the digestion of the tissues with acids (Table 4.13).

Table 4.13: Comparison of Ag concentrations (in nanograms of Ag per gram of placental tissue) in placental tissues collected after 6 h of perfusion, obtained by SP-ICP-MS after enzymatic treatment and by conventional ICP-MS after the digestion with acids. The given values represent the mean ± STD of two determinations for each sample. Presented are also p-values (t-test, $p < 0.01$) for comparison of Ag concentrations between two treatments.

Perfusion experiment	**Enzymatic digestion (SP-ICP-MS)**	**Acid digestion (ICP-MS)**	**p-value**
AgPEG NPs	3,994 ± 407	2,821 ± 262	0.305
AgCOONa NPs	12,597 ± 848	13,720 ± 6544	0.827
Ag +	765 ± 110	879 ± 12	0.351
control	25.0	<4.0	0.001

There was no significant difference (t-test, $p < 0.01$) between the Ag concentrations determined after the enzymatic treatment (spICPMS) and acid digestion (conventional ICPMS) for most of the tissue samples, suggesting that enzymatic treatment of the placental tissue is capable of extracting all AgNPs from tissues, similar to a more traditional acid digestion.

Chapter 5

Conclusions

In this doctoral dissertation the SP-ICP-MS method was optimized and applied for the detection and characterization of the most commonly used metal-based NPs (TiO_2NPs, AgNPs, nZVI) in complex environmental and biological matrices. Special care was devoted to the sample preparation and stabilization of NPs, as well as their quantitative extraction from biological matrices, with an emphasis on preservation of NPs original properties throughout the analytical procedure.

Procedures for effective stabilization of TiO_2NPs in aqueous samples, which are of significant importance when analytical methods for sizing of nanoscale Ti are applied, were studied. Nanoscale TiO_2 (rutile) was effectively stabilized in MilliQ water, using ultrasonication for dispersion. The efficiency of dispersion was verified by the determination of total Ti concentration with ICP-MS after the microwave-assisted digestion, which was optimized for decomposition of powdered TiO_2NPs and their dispersions in aqueous solutions. In combination with different dispersing agents (PEI 600, Darvan C and Triton X-100), ultrasonication did not significantly improve the stabilization of TiO_2NPs in MilliQ water. By applying the same dispersing procedures to river and wastewaters, spiked with nanoscale rutile and anatase, it has been demonstrated that due to high ionic strength, the stability of NPs was significantly decreased. In wastewater, despite the high content of NOM, the effect of high ionic strength prevailed. TiO_2NPs aggregation was reflected through low zeta potentials and poor Ti recoveries in the digested water samples. The data of the present investigation contribute to reliable procedures for the digestion and quantitative determination of TiO_2NPs in aqueous samples. In order not to compromise the NPs original properties, ultrasonication without the use of dispersing agents is recommended for dispersion of TiO_2NPs.

Sizing and simultaneous quantification of TiO_2NPs (anatase and rutile) and dissolved Ti was performed by SP-ICP-MS under optimized conditions with the optimal dwell time of 10 ms. Good recoveries between the determined and expected TiNPs mass concentrations and the calculated size distributions of the TiO_2NPs in anatase and rutile, which agreed well with the sizes determined from TEM and DLS measurements, confirmed the accuracy of the developed SP-ICP-MS procedure. It was further demonstrated that the procedure optimized for the determination of Ti in environmental waters can be applied in the sizing and quantification of TiNPs in river water samples spiked with nanoscale TiO_2. Although nanoscale titania was not present in measurable concentrations in the collected river water samples, SP-ICP-MS can be used for following its concentration at industrially exposed sites or bathing resorts.

The concentration and behaviour of nZVI after their use in nanoremediation was followed by SP-ICP-MS applying triple quadrupole ICP-MS equipped with a reaction cell technology in the MS/MS mode. Severe polyatomic interferences at m/z 56 were overcome with the use of H_2 as a reaction gas, which enabled sensitive measurements of low Fe

concentrations by SP-ICP-MS. For accurate determination of nZVI concentration and size by SP-ICP-MS, changing chemical composition due to oxidation of nZVI over time was considered. The optimized analytical procedure enabled us to follow the influence of the sample matrix, Fe load and settling time on the behavior of nZVI, as well as quantitative determination of Cd^{2+} concentration that interacts with nZVI. The results demonstrated that water matrix and Fe load have a key role in nanoremediation processes. The aggregation and sedimentation of nZVI increased with increasing the settling time. In effluent water the sedimentation was slower than in MilliQ water. Consequently Cd^{2+} was more efficiently (86 %) removed from effluent wastewater. The trace amounts of Cd^{2+}, which remained in the remediated water, were distributed between the dissolved fraction or were attached to the residual nZVI. The results from nanoremediation of the effluent wastewater with varying Fe loads showed that the sedimentation was faster at a higher initial concentration of nZVI. However, after 7 days of settling, negligible concentration of nZVI remained dispersed in the effluent wastewater at Fe loads 0.25 g/L or higher, indicating that the use of nZVI in nanoremediation under the described conditions does not present an environmental nano threat and enables effective removal of Cd from the effluent wastewater.

Translocation and accumulation of AgNP with different surface functionalization was studied on the *ex vivo* human placenta perfusion model by SP-ICP-MS. The results showed that AgPEG particles are more efficiently transported across placenta, while AgCOONa particles are accumulated in higher degree in placental tissue. The different translocation and accumulation behavior for both AgNP types could be caused by the differences in surface properties and/or size distributions in the perfusion medium. Although translocation was low for both NP types, the small amount of translocated ions/NPs may be sufficient to induce potential teratogenic effects considering the high vulnerability of the developing fetus and previous work, which showed potential neurodevelopmental effects. The results further demonstrate that particles detected on the fetal side are not necessarily the result of translocated pristine AgNPs but could also be Ag precipitates, formed from the dissolved Ag that crosses the placental barrier. Therefore, a careful assessment of particle dissolution and their redisposition under physiological conditions is essential to prevent artifacts in placental translocation studies using soluble NPs.

For studying AgNPs accumulation in human placental tissue by SP-ICP-MS, two potentially suitable sample preparation methods, alkaline treatment with the use of TMAH and enzymatic treatment with the use of enzyme Proteinase K, were compared. The results suggest that alkaline treatment followed by SP-ICP-MS analysis cannot be used for extracting AgNPs from the placental tissue samples because of Ag^{+} precipitation that apparently occurs due to the presence of TMAH and components in the tissue. On the other hand, during enzymatic treatment with Protease K the properties of AgNPs extracted from placental tissue were preserved. The experiments further showed that matrix matching cannot be applied for quantification and sizing of the digested tissue samples by SP-ICP-MS. Instead, ICP-MS response and transport efficiency were determined in water. The optimized analytical method with the use of enzymatic digestion coupled to SP-ICP-MS was successfully applied for quantification and sizing of AgPEG and AgCOONa NPs accumulated in placenta during *ex vivo* human perfusion experiment. Ag mass recovered from placental tissue using SP-ICP-MS analysis was comparable to the total Ag mass recovered using microwave-assisted digestion. The SP-ICP-MS method also provided additional information on the characterization of AgNPs (i.e. size distribution, ionic/particulate form of Ag) that can significantly contribute to the interpretation of toxicological data generated during human placenta perfusion experiments.

References

[1] SCENIHR, "The scientific aspects of the existing and proposed definitions relating to products of nanoscience and nanotechnologies," p. 22, 2007.

[2] T. Commission, T. European, and C. Joint, "L 275/38," pp. 2010–2012, 2011.

[3] M. Farre´ and D. Barcelo´, "Introduction to the Analysis and Risk of Nanomaterials in Environmental and Food Samples", in: *Analysis and Risk of Nanomaterials in Environmental and Food Samples*, vol. 59. Elsevier, 2012.

[4] S. J. Klaine, P. J. J. Alvarez, G. E. Batley, T. F. Fernandes, R. D. Handy, D. Y. Lyon, S. Mahendra, M. J. Mclaughlin and J. R. Lead, "Critical review Nanomaterials in the environment: behavior, fate, bioavailability, and effects," *Environmental toxicology and chemistry,* vol. 27, no. 9, pp. 1825–1851, 2008.

[5] M. D. Montano, G. V. Lowry, F. von der Kammer, J. Blue, and J. F. Ranville, "Current status and future direction for examining engineered nanoparticles in natural systems," *Environ. Chem.*, vol. 11, pp. 351–366, 2014.

[6] I. Bhatt and B. N. Tripathi, "Interaction of engineered nanoparticles with various components of the environment and possible strategies for their risk assessment.," *Chemosphere*, vol. 82, no. 3, pp. 308–17, 2011.

[7] M. E. Vance *et al.*, "Nanotechnology in the real world: Redeveloping the nanomaterial consumer products inventory," *Beilstein J. Nanotechnol.*, vol. 6, no. 1, pp. 1769–1780, 2015.

[8] A. Weir, P. Westerhoff, L. Fabricius, K. Hristovski, and N. von Goetz, "Titanium dioxide nanoparticles in food and personal care products.," *Environ. Sci. Technol.*, vol. 46, no. 4, pp. 2242–50, 2012.

[9] A. Menard, D. Drobne, and A. Jemec, "Ecotoxicity of nanosized TiO2. Review of in vivo data.," *Environ. Pollut.*, vol. 159, no. 3, pp. 677–84, 2011.

[10] X. Qu, P. J. J. Alvarez, and Q. Li, "Applications of nanotechnology in water and wastewater treatment," *Water Res.*, vol. 47, no. 12, pp. 3931–3946, 2013.

[11] M. A. Hassanien and A. M. El Shahawy, "Environmental Heavy Metal Pollution and Effects on Child Mental Development," Lubomir I. Simeonov et al. Eds., Springer, Dordrecht, 2010.

[12] M. P. Waalkes, "Cadmium carcinogenesis in review.," *J. Inorg. Biochem.*, vol. 79, no. 1–4, pp. 241–4, 2000.

[13] R. K. Zalups and S. Ahmad, "Molecular handling of cadmium in transporting epithelia." Toxicology and Applied Pharmacology, vol. 186, pp. 163–188, 2003.

[14] "Guidelines for Drinking-water Quality Fourth Edition WHO Library Cataloguing-in-Publication Data," *World Heal. Organ.*

[15] R. A. Crane and T. B. Scott, "Nanoscale zero-valent iron: Future prospects for an emerging water treatment technology," *J. Hazard. Mater.*, vol. 211–212, pp. 112–125, 2012.

[16] T. Pradeep, "Noble metal nanoparticles for water purification: A critical review,"

Thin Solid Films, vol. 517, no. 24, pp. 6441–6478, 2009.

[17] C. Noubactep and S. Caré, "On nanoscale metallic iron for groundwater remediation," *J. Hazard. Mater.*, vol. 182, no. 1–3, pp. 923–927, 2010.

[18] G. E. Batley, J. K. Kirby, and M. J. McLaughlin, "Fate and Risks of Nanomaterials in Aquatic and Terrestrial Environments," *Acc. Chem. Res.*, vol. 46, no. 3, pp. 854–862, 2013.

[19] D. O. Carroll, B. Sleep, M. Krol, H. Boparai, and C. Kocur, "Advances in Water Resources Nanoscale zero valent iron and bimetallic particles for contaminated site remediation," *Adv. Water Resour.*, vol. 51, pp. 104–122, 2013.

[20] B. Calderon and A. Fullana, "Heavy metal release due to aging effect during zero valent iron nanoparticles remediation," *Water Res.*, vol. 83, pp. 1–9, 2015.

[21] Z. Shi *et al.*, "Methods for characterizing the fate and effects of nano zerovalent iron during groundwater remediation," *J. Contam. Hydrol.*, vol. 181, pp. 1–19, 2014.

[22] M. Ahamed, M. S. AlSalhi, and M. K. J. Siddiqui, "Silver nanoparticle applications and human health," *Clin. Chim. Acta*, vol. 411, no. 23–24, pp. 1841–1848, 2010.

[23] A. López-Serrano, R. M. Olivas, J. S. Landaluze, and C. Cámara, "Nanoparticles: a global vision. Characterization, separation, and quantification methods. Potential environmental and health impact," *Anal. Methods*, vol. 6, no. 1, p. 38, 2014.

[24] P. Biswas and C. Wu, "Nanoparticles and the Environment," *Journal of the Air & Waste Management Association*, vol. 55, no. 6, pp. 708–746, 2012.

[25] A. Charron and R. M. Harrison, "Atmospheric Nanoparticles," *Environ. Hum. Heal. Impacts Nanotechnol.*, pp. 163–209, 2009.

[26] H. Weinberg, A. Galyean, and M. Leopold, "Evaluating engineered nanoparticles in natural waters," *TrAC Trends Anal. Chem.*, vol. 30, no. 1, pp. 72–83, 2011.

[27] B. Nowack and T. D. Bucheli, "Occurrence, behavior and effects of nanoparticles in the environment.," *Environ. Pollut.*, vol. 150, no. 1, pp. 5–22, 2007.

[28] F. Laborda *et al.*, "Detection, characterization and quantification of inorganic engineered nanomaterials: A review of techniques and methodological approaches for the analysis of complex samples," *Anal. Chim. Acta*, vol. 904, pp. 10–32, 2016.

[29] E. Navarro *et al.*, "Environmental behavior and ecotoxicity of engineered nanoparticles to algae, plants, and fungi.," *Ecotoxicology*, vol. 17, no. 5, pp. 372–86, 2008.

[30] A. M. E. L. Badawy, T. P. Luxton, R. G. Silva, K. G. Scheckel, and M. T. Suidan, "Impact of Environmental Conditions (pH , Ionic Strength , and Electrolyte Type) on the Surface Charge and Aggregation of Silver Nanoparticles Suspensions," *Environ. Sci. Technol.*, vol. 44, no. 4, pp. 1260–1266, 2010. 2010, 44, 1260–1266

[31] P. Leroy, C. Tournassat, and M. Bizi, "Influence of surface conductivity on the apparent zeta potential of TiO2 nanoparticles," *J. Colloid Interface Sci.*, vol. 356, no. 2, pp. 442–453, 2011.

[32] F. Mafuné, J. Kohno, Y. Takeda, T. Kondow, and H. Sawabe, "Structure and Stability of Silver Nanoparticles in Aqueous Solution Produced by Laser Ablation," *J. Phys. Chem. B*, vol. 104, no. 35, pp. 8333–8337, 2000.

[33] E. M. Hotze, T. Phenrat, and G. V Lowry, "Nanoparticle aggregation: challenges to understanding transport and reactivity in the environment.," *J. Environ. Qual.*, vol. 39, pp. 1909–1924, 2010.

[34] T. Tervonen, I. Linkov, J. R. Figueira, J. Steevens, M. Chappell, and M. Merad, "Risk-based classification system of nanomaterials," *J. Nanoparticle Res.*, vol. 11, no. 4, pp. 757–766, 2008.

[35] H. Hyung, J. D. Fortner, J. B. Hughes, and J.-H. Kim, "Natural Organic Matter Stabilizes Carbon Nanotubes in the Aqueous Phase," *Environ. Sci. Technol.*, vol. 41, no. 1, pp. 179–184, 2006.

[36] A. B. M. Giasuddin, S. R. Kanel, and H. Choi, "Adsorption of humic acid onto nanoscale zerovalent iron and its effect on arsenic removal," *Environ. Sci. Technol.*, vol. 41, no. 6, pp. 2022–2027, 2007.

[37] N. Akaighe, S. W. Depner, S. Banerjee, V. K. Sharma, and M. Sohn, "The effects of monovalent and divalent cations on the stability of silver nanoparticles formed from direct reduction of silver ions by Suwannee River humic acid/natural organic matter.," *Sci. Total Environ.*, vol. 441, pp. 277–89, 2012.

[38] J. T. K. Quik, I. Velzeboer, M. Wouterse, A. A. Koelmans, and D. van de Meent, "Heteroaggregation and sedimentation rates for nanomaterials in natural waters.," *Water Res.*, vol. 48, pp. 269–79, 2014.

[39] P. Miralles, T. L. Church, and A. T. Harris, "Toxicity, Uptake, and Translocation of Engineered Nanomaterials in Vascular plants.," *Environ. Sci. Technol.*, vol. 46, no. 17, pp. 9224–39, 2012.

[40] M. A. Maurer-Jones, I. L. Gunsolus, C. J. Murphy, and C. L. Haynes, "Toxicity of engineered nanoparticles in the environment.," *Anal. Chem.*, vol. 85, no. 6, pp. 3036–49, 2013.

[41] T.W. May, R.H. Wiedmeyer, "A table of polyatomic interferences in ICP-MS," *At. Spectrosc.,* vol. 19, pp. 150-155, 1998.

[42] K. Aschberger, C. Micheletti, B. Sokull-Klüttgen, and F. M. Christensen, "Analysis of currently available data for characterising the risk of engineered nanomaterials to the environment and human health--lessons learned from four case studies.," *Environ. Int.*, vol. 37, no. 6, pp. 1143–56, 2011.

[43] N. Singh *et al.*, "NanoGenotoxicology: The DNA damaging potential of engineered nanomaterials," *Biomaterials*, vol. 30, no. 23–24, pp. 3891–3914, 2009.

[44] M. D. Avakian *et al.*, "The origin, fate, and health effects of combustion by-products: A research framework," *Environ. Health Perspect.*, vol. 110, no. 11, pp. 1155–1162, 2002.

[45] L. Morawska and J. Zhang, "Combustion sources of particles. 1. Health relevance and source signatures," *Chemosphere*, vol. 49, no. 9, pp. 1045–1058, 2002.

[46] B. Armstrong, E. Hutchinson, J. Unwin, and T. Fletcher, "Lung cancer risk after exposure to polycyclic aromatic hydrocarbons: A review and meta-analysis," *Environ. Health Perspect.*, vol. 112, no. 9, pp. 970–978, 2004.

[47] B. J. Shaw and R. D. Handy, "Physiological effects of nanoparticles on fish: a comparison of nanometals versus metal ions.," *Environ. Int.*, vol. 37, no. 6, pp. 1083–97, 2011.

[48] K. Hund-Rinke and M. Simon, "Ecotoxic effect of photocatalytic active nanoparticles (TiO2) on algae and daphnids.," *Environ. Sci. Pollut. Res. Int.*, vol. 13, no. 4, pp. 225–32, 2006.

[49] B. Campos, C. Rivetti, P. Rosenkranz, J. M. Navas, and C. Barata, "Effects of nanoparticles of TiO2 on food depletion and life-history responses of Daphnia

magna.," *Aquat. Toxicol.*, vol. 130–131, pp. 174–83, 2013.

[50] X. Zhu, Y. Chang, and Y. Chen, "Toxicity and bioaccumulation of TiO2 nanoparticle aggregates in Daphnia magna," *Chemosphere*, vol. 78, no. 3, pp. 209–215, 2010.

[51] Z. Clemente, V. L. Castro, C. M. Jonsson, and L. F. Fraceto, "Minimal levels of ultraviolet light enhance the toxicity of TiO2 nanoparticles to two representative organisms of aquatic systems," *J. Nanoparticle Res.*, vol. 16, p. 2559, 2014.

[52] R. J. Miller, S. Bennett, A. A. Keller, S. Pease, and H. S. Lenihan, "TiO2 nanoparticles are phototoxic to marine phytoplankton.," *PLoS One*, vol. 7, no. 1, p. e30321, 2012.

[53] G. Federici, B. J. Shaw, and R. D. Handy, "Toxicity of titanium dioxide nanoparticles to rainbow trout (Oncorhynchus mykiss): gill injury, oxidative stress, and other physiological effects.," *Aquat. Toxicol.*, vol. 84, no. 4, pp. 415–30, 2007.

[54] W. Fan *et al.*, "Nano-TiO2 enhances the toxicity of copper in natural water to Daphnia magna.," *Environ. Pollut.*, vol. 159, no. 3, pp. 729–34, 2011.

[55] D. B. Warheit, T. R. Webb, K. L. Reed, S. Frerichs, and C. M. Sayes, "Pulmonary toxicity study in rats with three forms of ultrafine-TiO2 particles: differential responses related to surface properties.," *Toxicology*, vol. 230, no. 1, pp. 90–104, 2007.

[56] C. Jin *et al.*, "Cellular toxicity of TiO2 nanoparticles in anatase and rutile crystal phase," *Biol. Trace Elem. Res.*, vol. 141, pp. 3–15, 2011.

[57] K. Gerloff *et al.*, "Distinctive toxicity of TiO2 rutile/anatase mixed phase nanoparticles on Caco-2 cells," *Chem. Res. Toxicol.*, vol. 25, pp. 646–655, 2012.

[58] C. R. Keenan, R. Goth-Goldstein, D. Lucas, and D. L. Sedlak, "Oxidative stress induced by zero-valent iron nanoparticles and Fe(II) in human bronchial epithelial cells.," *Environ. Sci. Technol.*, vol. 43, no. 12, pp. 4555–4560, 2009.

[59] T. R. Pisanic, J. D. Blackwell, V. I. Shubayev, and R. R. Fin, "Nanotoxicity of iron oxide nanoparticle internalization in growing neurons," vol. 28, pp. 2572–2581, 2007.

[60] P. Taylor, K. M. Zabetakis, G. T. N. De Guzmán, A. Torrents, and S. Yarwood, "Toxicity of zero-valent iron nanoparticles to a trichloroethylene-degrading groundwater microbial community," *Journal of Environmental Science and Health, Part A,* no. June, pp. 37–41, 2015.

[61] P. J. Chen, W. L. Wu, and K. C. W. Wu, "The zerovalent iron nanoparticle causes higher developmental toxicity than its oxidation products in early life stages of medaka fish," *Water Res.*, vol. 47, no. 12, pp. 3899–3909, 2013.

[62] C. C. E and N. Carolina, "Relation between the Redox State of Iron-Based Nanoparticles and Their Cytotoxicity toward Escherichia coli," vol. 42, no. 17, pp. 6730–6735, 2008.

[63] A. A. Keller, K. Garner, R. J. Miller, and H. S. Lenihan, "Toxicity of Nano-Zero Valent Iron to Freshwater and Marine Organisms," *PLoS One*, vol. 7, no. 8, pp. 1–10, 2012.

[64] M. I. N. Ahamed, "Ecotoxicity concert of nano zero-valent iron particles- a review," *Journal of Critical Reviews,* vol. 1, no. 1, 2014.

[65] M. C. Stensberg, Q. Wei, E. S. Mclamore, and D. Marshall, "Toxicological studies on silver nanoparticles: challenges and opportunities in assessment, monitoring and imaging," *NIH Public Access*, vol. 6, no. 5, pp. 879–898, 2012.

[66] S. Kim and D.-Y. Ryu, "Silver nanoparticle-induced oxidative stress, genotoxicity and apoptosis in cultured cells and animal tissues," *J. Appl. Toxicol.*, vol. 33, no. 2, pp. 78–89, 2013.

[67] K. Yamashita *et al.*, "Silica and titanium dioxide nanoparticles cause pregnancy complications in mice," *Nat. Nanotechnol.*, vol. 6, no. 5, pp. 321–328, 2011.

[68] A. Pietroiusti *et al.*, "Low Doses of Pristine and Oxidized Single-Wall Carbon Nanotubes Affect Mammalian Embryonic Development," *ACS Nano*, vol. 5, no. 6, pp. 4624–4633, 2011.

[69] L. Campagnolo *et al.*, "Biodistribution and toxicity of pegylated single wall carbon nanotubes in pregnant mice," *Part Fibre Toxicol*, vol. 10, p. 21, 2013.

[70] K. S. Hougaard *et al.*, "A perspective on the developmental toxicity of inhaled nanoparticles," *Reprod. Toxicol.*, vol. 56, pp. 118–140, 2015.

[71] J.-S. Hong *et al.*, "Combined repeated-dose toxicity study of silver nanoparticles with the reproduction/developmental toxicity screening test," *Nanotoxicology*, vol. 8, no. 4, pp. 349–362, 2014.

[72] W. J. Yu *et al.*, "Effects of silver nanoparticles on pregnant dams and embryo-fetal development in rats," *Nanotoxicology*, vol. 1, pp. 1–7, 2013.

[73] M. Charehsaz *et al.*, "Effects of developmental exposure to silver in ionic and nanoparticle form: A study in rats," *Daru-Journal Pharm. Sci.*, vol. 24, pp. 1–13, 2016.

[74] N. A. Philbrook, L. M. Winn, A. R. M. N. Afrooz, N. B. Saleh, and V. K. Walker, "The effect of TiO2 and Ag nanoparticles on reproduction and development of Drosophila melanogaster and CD-1 mice," *Toxicol. Appl. Pharmacol.*, vol. 257, no. 3, pp. 429–436, 2011.

[75] C. M. Powers, E. D. Levin, F. J. Seidler, and T. A. Slotkin, "Silver exposure in developing zebrafish produces persistent synaptic and behavioral changes," *Neurotoxicol. Teratol.*, vol. 33, no. 2, pp. 329–332, 2011.

[76] Y. Wu, Q. Zhou, H. Li, W. Liu, T. Wang, and G. Jiang, "Effects of silver nanoparticles on the development and histopathology biomarkers of Japanese medaka (Oryzias latipes) using the partial-life test," *Aquat. Toxicol.*, vol. 100, no. 2, pp. 160–167, 2010.

[77] T. I. Ala-Kokko, P. Myllynen, and K. Vähäkangas, "Ex vivo perfusion of the human placental cotyledon: implications for anesthetic pharmacology," *Int. J. Obstet. Anesth.*, vol. 9, no. 1, pp. 26–38, 2000.

[78] Enders and Blankenship, "Comparative placental structure.," *Adv. Drug Deliv. Rev.*, vol. 38, no. 1, pp. 3–15, 1999.

[79] M. Panigel, M. Pascaud, and J. L. Brun, "Radioangiographic study of circulation in the villi and intervillous space of isolated human placental cotyledon kept viable by perfusion," *J. Physiol. (Paris).*, vol. 59, no. 1 Suppl, p. 277, 1967.

[80] C. Muoth, L. Aengenheister, M. Kucki, P. Wick, and T. Buerki-Thurnherr, "Nanoparticle transport across the placental barrier : pushing the field forward !," *Nanomedicine*, vol. 11, no. 8, pp. 941-57, 2016.

[81] T. Buerki-Thurnherr, U. Von Mandach, and P. Wick, "Knocking at the door of the unborn child: Engineered nanoparticles at the human placental barrier," *Swiss Med. Wkly.*, vol. 142, pp. 1–9, 2012.

[82] E. A. Melnik *et al.*, "Transfer of silver nanoparticles through the placenta and breast

milk during in vivo experiments on rats," *Acta Naturae*, vol. 5, no. 18, pp. 107–115, 2013.

[83] C. A. Austin *et al.*, "Distribution of silver nanoparticles in pregnant mice and developing embryos," *Nanotoxicology*, vol. 6, pp. 1–11, 2011.

[84] T. R. Fennell *et al.*, "Disposition of intravenously or orally administered silver nanoparticles in pregnant rats and the effect on the biochemical profile in urine," *J. Appl. Toxicol.*, 2016, doi: 10.1002/jat.3387.

[85] J. S. Refuerzo *et al.*, "Size of the nanovectors determines the transplacental passage in pregnancy: study in rats," *Am. J. Obstet. Gynecol.*, vol. 204, no. 6, p. 546.e5-546.e9, 2011.

[86] A. Bruinink, J. Wang, and P. Wick, "Effect of particle agglomeration in nanotoxicology," *Arch. Toxicol.*, vol. 89, no. 5, pp. 659–675, 2015.

[87] A. E. Nel *et al.*, "Understanding biophysicochemical interactions at the nano-bio interface," *Nat. Mater.*, vol. 8, no. 7, pp. 543–557, 2009.

[88] K. Loza *et al.*, "The dissolution and biological effects of silver nanoparticles in biological media," *J. Mater. Chem. B*, vol. 2, p. 1634, 2014.

[89] A. R. Gliga, S. Skoglund, I. Odnevall Wallinder, B. Fadeel, and H. L. Karlsson, "Size-dependent cytotoxicity of silver nanoparticles in human lung cells: the role of cellular uptake, agglomeration and Ag release," *Part. Fibre Toxicol.*, vol. 11, no. 1, p. 11, 2014.

[90] Z. Xiu, Q. Zhang, H. L. Puppala, V. L. Colvin, and P. J. J. Alvarez, "Negligible Particle-Specific Antibacterial Activity of Silver Nanoparticles," *Nano Lett.*, vol. 12, pp. 4271–4275, 2012.

[91] N. Hadrup *et al.*, "The similar neurotoxic effects of nanoparticulate and ionic silver in vivo and in vitro," *Neurotoxicology*, vol. 33, pp. 416–423, 2012.

[92] T. P. J. Linsinger, G. Roebben, C. Solans, and R. Ramsch, "Reference materials for measuring the size of nanoparticles," *TrAC Trends Anal. Chem.*, vol. 30, no. 1, pp. 18–27, 2011.

[93] J. R. Lead and K. J. Wilkinson, "Environmental Colloids and Particles: Current Knowledge and Future Developments," in *Environmental Colloids and Particles*, Chichester, UK: John Wiley & Sons, Ltd, pp. 1–15, 2007.

[94] C. Blasco and Y. Picó, "Determining nanomaterials in food," *TrAC Trends Anal. Chem.*, vol. 30, no. 1, pp. 84–99, 2011.

[95] B. J. Shaw, C. S. Ramsden, A. Turner, and R. D. Handy, "A simplified method for determining titanium from TiO2 nanoparticles in fish tissue with a concomitant multi-element analysis.," *Chemosphere*, vol. 92, no. 9, pp. 1136–44, 2013.

[96] H. Sun, X. Zhang, Q. Niu, Y. Chen, and J. C. Crittenden, "Enhanced accumulation of arsenate in carp in the presence of titanium dioxide nanoparticles," *Water. Air. Soil Pollut.*, vol. 178, pp. 245–254, 2007.

[97] M. G. A. Korn, A. C. Ferreira, and A. Costa, "Comparison of decomposition procedures for analysis of titanium dioxide using inductively coupled plasma optical emission spectrometry," *Microchem. J.*, pp. 2–9, 2002.

[98] C. Yong, "Microwave Digestion - Graphite Furnace Atomic Absorption Spectrometry Determination of Trace Arsenic in the Nano-Titanium Dioxide," *Adv. Mater. Res.*, vol. 718–720, pp. 1113–1117, 2013.

[99] K. Khosravi, M. E. Hoque, B. Dimock, H. Hintelmann, and C. D. Metcalfe, "A novel approach for determining total titanium from titanium dioxide nanoparticles suspended in water and biosolids by digestion with ammonium persulfate," *Anal. Chim. Acta*, vol. 713, pp. 86–91, 2012.

[100] J. C. Méranger and E. Somers, "Determination of antimony in titanium dioxide by atomic-absorption spectrophotometry," *Analyst*, vol. 93, no. 1113, pp. 799–801, 1968.

[101] Z. Šulcek and P. Povondra, *Methods of decomposition in inorganic analysis*. Boca Raton Florida [etc.]: CRC Press, 1989.

[102] R. Peters *et al.*, "Identification and characterization of organic nanoparticles in food," *TrAC Trends Anal. Chem.*, vol. 30, no. 1, pp. 100–112, 2011.

[103] E. P. Gray, J. G. Coleman, A. J. Bednar, A. J. Kennedy, J. F. Ranville, and C. P. Higgins, "Extraction and Analysis of Silver and Gold Nanoparticles from Biological Tissues Using Single Particle Inductively Coupled Plasma Mass Spectrometry," *Environ. Sci. Technol.*, vol. 47, pp. 14315–14323, 2013.

[104] J. Jiménez-Lamana *et al.*, "An insight into silver nanoparticles bioavailability in rats," *Metallomics*, vol. 6, pp. 2242–2249, 2014.

[105] K. Loeschner, M. S. J. Brabrand, J. J. Sloth, and E. H. Larsen, "Use of alkaline or enzymatic sample pretreatment prior to characterization of gold nanoparticles in animal tissue by single-particle ICPMS Characterisation of Nanomaterials in Biological Samples," *Anal. Bioanal. Chem.*, vol. 406, pp. 3845–3851, 2014.

[106] B. Kollander, F. Widemo, E. Ågren, E. H. Larsen, and K. Loeschner, "Detection of lead nanoparticles in game meat by single particle ICP-MS following use of lead-containing bullets," *Anal. Bioanal. Chem.*, vol. 409, pp. 1877–1885, 2017.

[107] K. Loeschner, C. F. Harrington, J.-L. Kearney, D. J. Langton, and E. H. Larsen, "Feasibility of asymmetric flow field-flow fractionation coupled to ICP-MS for the characterization of wear metal particles and metalloproteins in biofluids from hip replacement patients," *Anal. Bioanal. Chem.*, vol. 407, pp. 4541–4554, 2015.

[108] E. Bolea *et al.*, "Detection and characterization of silver nanoparticles and dissolved species of silver in culture medium and cells by AsFlFFF-UV-Vis-ICPMS: application to nanotoxicity tests.," *Analyst*, vol. 139, pp. 914–922, 2014.

[109] H. Klingberg, L. B. Oddershede, K. Loeschner, E. H. E. H. Larsen, S. Loft, and P. Møller, "Uptake of gold nanoparticles in primary human endothelial cells," *Toxicol. Res. (Camb).*, vol. 4, pp. 655–666, 2015.

[110] M. Van Der Zande *et al.*, "Distribution, Elimination, and Toxicity of Silver Nanoparticles and Silver Ions in Rats after 28-Day Oral Exposure," *ACS Nano*, vol. 6, no. 8, pp. 7427–7442, 2012.

[111] S. Makama, R. Peters, A. Undas, and N. W. Van Den Brink, "A novel method for the quantification, characterisation and speciation of silver nanoparticles in earthworms exposed in soil," *Environ. Chem.*, vol. 12, no. 6, pp. 643–651, 2015.

[112] R. J. B. Peters, Z. H. Rivera, G. Van Bemmel, H. J. P. Marvin, S. Weigel, and H. Bouwmeester, "Development and validation of single particle ICP-MS for sizing and quantitative determination of nano-silver in chicken meat Characterisation of Nanomaterials in Biological Samples," *Anal. Bioanal. Chem.*, vol. 406, pp. 3875–3885, 2014.

[113] R. Peters *et al.*, "Single particle ICP-MS combined with a data evaluation tool as a

routine technique for the analysis of nanoparticles in complex matrices," *J. Anal. At. Spectrom.*, vol. 30, pp. 1274–1285, 2015.

[114] K. Loeschner *et al.*, "In-house validation of a method for determination of silver nanoparticles in chicken meat based on asymmetric flow field-flow fractionation and inductively coupled plasma mass spectrometric detection," *Food Chem.*, vol. 181, pp. 78–84, 2015.

[115] K. Loeschner *et al.*, "Detection and characterization of silver nanoparticles in chicken meat by asymmetric flow field flow fractionation with detection by conventional or single particle ICP-MS," *Anal. Bioanal. Chem.*, vol. 405, pp. 8185–8195, 2013.

[116] Y. Dan, W. Zhang, R. Xue, X. Ma, C. Stephan, and H. Shi, "Characterization of gold nanoparticle uptake by tomato plants using enzymatic extraction followed by single-particle inductively coupled plasma-mass spectrometry analysis.," *Environ. Sci. Technol.*, vol. 49, pp. 3007–3014, 2015.

[117] J. Jiménez-Lamana, J. Wojcieszek, M. Jakubiak, M. Asztemborska, and J. Szpunar, "Single particle ICP-MS characterization of platinum nanoparticles uptake and bioaccumulation by Lepidium sativum and Sinapis alba plants," *J. Anal. At. Spectrom.*, vol. 31, pp. 2321–2329, 2016.

[118] Y. Dan, X. Ma, W. Zhang, K. Liu, C. Stephan, and H. Shi, "Single particle ICP-MS method development for the determination of plant uptake and accumulation of CeO2 nanoparticles," *Anal. Bioanal. Chem.*, vol. 408, pp. 5157–5167, Jul. 2016.

[119] D. Bao, Z. G. Oh, and Z. Chen, "Characterization of Silver Nanoparticles Internalized by Arabidopsis Plants Using Single Particle ICP-MS Analysis," *Front. Plant Sci.*, vol. 7, no. February, p. 32, 2016.

[120] V. Armendariz, J. G. Parsons, M. L. Lopez, J. R. Peralta-Videa, M. Jose-Yacaman, and J. L. Gardea-Torresdey, "The extraction of gold nanoparticles from oat and wheat biomasses using sodium citrate and cetyltrimethylammonium bromide, studied by x-ray absorption spectroscopy, high-resolution transmission electron microscopy, and UV-visible spectroscopy.," *Nanotechnology*, vol. 20, no. 10, p. 105607, Mar. 2009.

[121] K. Tiede, A. B. A. Boxall, S. P. Tear, J. Lewis, H. David, and M. Hassellov, "Detection and characterization of engineered nanoparticles in food and the environment.," *Food Addit. Contam. Part A. Chem. Anal. Control. Expo. Risk Assess.*, vol. 25, no. 7, pp. 795–821, Jul. 2008.

[122] S. M. Majedi, B. C. Kelly, and H. K. Lee, "Efficient hydrophobization and solvent microextraction for determination of trace nano-sized silver and titanium dioxide in natural waters.," *Anal. Chim. Acta*, vol. 789, pp. 47–57, Jul. 2013.

[123] F. Loosli, P. Le Coustumer, and S. Stoll, "Effect of electrolyte valency, alginate concentration and pH on engineered TiO2 nanoparticle stability in aqueous solution," *Sci. Total Environ.*, pp. 1–7, 2015.

[124] C. Tso, C. Zhung, Y. Shih, Y.-M. Tseng, S. Wu, and R. Doong, "Stability of metal oxide nanoparticles in aqueous solutions.," *Water Sci. Technol.*, vol. 61, no. 1, pp. 127–33, Jan. 2010.

[125] C. Sentein, B. Guizard, S. Giraud, C. Yé, and F. Ténégal, "Dispersion and stability of TiO 2 nanoparticles synthesized by laser pyrolysis in aqueous suspensions," *J. Phys. Conf. Ser.*, vol. 170, p. 12013, May 2009.

[126] M. Hassellöv, J. W. Readman, J. F. Ranville, and K. Tiede, "Nanoparticle analysis

and characterization methodologies in environmental risk assessment of engineered nanoparticles.," *Ecotoxicology*, vol. 17, no. 5, pp. 344–61, Jul. 2008.

[127] K. Tiede, A. B. A. Boxall, D. Tiede, S. P. Tear, H. David, and J. Lewis, "A robust size-characterisation methodology for studying nanoparticle behaviour in 'real' environmental samples, using hydrodynamic chromatography coupled to ICP-MS," *J. Anal. At. Spectrom.*, vol. 24, no. 7, p. 964, 2009.

[128] D. M. A. M. Luykx, R. J. B. Peters, S. M. van Ruth, and H. Bouwmeester, "A review of analytical methods for the identification and characterization of nano delivery systems in food.," *J. Agric. Food Chem.*, vol. 56, no. 18, pp. 8231–47, 2008.

[129] F. Laborda, E. Bolea, and J. Jiménez-Lamana, "Single particle inductively coupled plasma mass spectrometry for the analysis of inorganic engineered nanoparticles in environmental samples," *Trends Environ. Anal. Chem.*, vol. 9, pp. 15–23, 2016.

[130] S. M. Nelms, Ed., *Inductively Coupled Plasma Mass Spectrometry Handbook*. Oxford, UK: Blackwell Publishing Ltd., 2005.

[131] J. W. Olesik and P. J. Gray, "Considerations for measurement of individual nanoparticles or microparticles by ICP-MS: determination of the number of particles and the analyte mass in each particle," *J. Anal. At. Spectrom.*, vol. 27, no. 7, p. 1143, 2012.

[132] B. Fernández, J. M. Costa, R. Pereiro, and A. Sanz-Medel, "Inorganic mass spectrometry as a tool for characterisation at the nanoscale.," *Anal. Bioanal. Chem.*, vol. 396, no. 1, pp. 15–29, 2010.

[133] C. Degueldre and P. Y. Favarger, "Colloid analysis by single particle inductively coupled plasma-mass spectroscopy: A feasibility study," *Colloids Surfaces A Physicochem. Eng. Asp.*, vol. 217, pp. 137–142, 2003.

[134] J. Liu, K. E. Murphy, R. I. Maccuspie, M. R. Winchester, and B. Drive, "Optimizing Instrument Operation and Data Processing for Single Particle Inductively Coupled Plasma Mass Spectrometry Measurement of Gold Nanoparticles," vol. 1, pp. 151–154, 2013.

[135] M. D. Montaño, J. W. Olesik, A. G. Barber, K. Challis, and J. F. Ranville, "Single Particle ICP-MS: Advances toward routine analysis of nanomaterials," *Anal. Bioanal. Chem.*, vol. 408, pp. 5053–5074, 2016.

[136] G. Cornelis and M. Hassellöv, "A signal deconvolution method to discriminate smaller nanoparticles in single particle ICP-MS," *J. Anal. At. Spectrom.*, vol. 29, pp. 134–144, 2014.

[137] R. Peters *et al.*, "Single particle ICP-MS combined with a data evaluation tool as a routine technique for the analysis of nanoparticles in complex matrices," *J. Anal. At. Spectrom.*, vol. 30, pp. 1274–1285, 2015.

[138] Y. Yang, C. Long, H. Li, Q. Wang, and Z. Yang, "Analysis of silver and gold nanoparticles in environmental water using single particle-inductively coupled plasma-mass spectrometry," *Science of the Total Environment*, 2016, doi:10.1016/j.scitotenv.2015.12.150

[139] A. Hineman and C. Stephan, "Effect of dwell time on single particle inductively coupled plasma mass spectrometry data acquisition quality," *J. Anal. At. Spectrom.*, vol. 29, no. 7, p. 1252, 2014.

[140] Y. Dan, W. Zhang, R. Xue, X. Ma, C. Stephan, and H. Shi, "Characterization of gold nanoparticle uptake by tomato plants using enzymatic extraction followed by

single-particle inductively coupled plasma-mass spectrometry analysis.," *Environ. Sci. Technol.*, vol. 49, pp. 3007–30

[141] C. Degueldre, P.-Y. Favarger, and S. Wold, "Gold colloid analysis by inductively coupled plasma-mass spectrometry in a single particle mode," *Anal. Chim. Acta*, vol. 555, no. 2, pp. 263–268, 2006.

[142] A. R. Donovan, C. D. Adams, Y. Ma, C. Stephan, T. Eichholz, and H. Shi, "Single particle ICP-MS characterization of titanium dioxide, silver, and gold nanoparticles during drinking water treatment," *Chemosphere*, vol. 144, pp. 148–153, 2016.

[143] G. Cornelis and M. Hassellöv, "A signal deconvolution method to discriminate smaller nanoparticles in single particle ICP-MS," *J. Anal. At. Spectrom.*, vol. 29, no. 1, p. 134, 2014.

[144] J. Tuoriniemi, G. Cornelis, and M. Hassellöv, "Size discrimination and detection capabilities of single-particle ICPMS for environmental analysis of silver nanoparticles.," *Anal. Chem.*, vol. 84, no. 9, pp. 3965–72, 2012.

[145] D. Bao, Z. G. Oh, and Z. Chen, "Characterization of Silver Nanoparticles Internalized by Arabidopsis Plants Using Single Particle ICP-MS Analysis," *Front. Plant Sci.*, vol. 7, p. 32, 2016.

[146] H. E. Pace *et al.*, "Single particle inductively coupled plasma-mass spectrometry: a performance evaluation and method comparison in the determination of nanoparticle size.," *Environ. Sci. Technol.*, vol. 46, no. 22, pp. 12272–80, 2012.

[147] K. Ramos, M. M. Gómez-Gómez, C. Cámara, and L. Ramos, "Silver Speciation and characterization of nanoparticles released from plastic food containers by single particle ICPMS," *Talanta*, vol. 151, pp. 83–90, 2015.

[148] R. B. Reed, C. P. Higgins, P. Westerhoff, S. Tadjiki, and J. F. Ranville, "Overcoming challenges in analysis of polydisperse metal-containing nanoparticles by single particle inductively coupled plasma mass spectrometry," *J. Anal. At. Spectrom.*, vol. 27, no. 7, p. 1093, 2012.

[149] Y. Yang, C. L. Long, Z. G. Yang, H. P. Li, and Q. Wang, "Characterization and determination of silver nanoparticle using single particle-inductively coupled plasma-mass spectrometry," *Fenxi Huaxue/ Chinese J. Anal. Chem.*, vol. 42, no. 11, pp. 1553–1560, 2014.

[150] H. E. Pace, N. J. Rogers, C. Jarolimek, V. A. Coleman, C. P. Higgins, and J. F. Ranville, "Determining transport efficiency for the purpose of counting and sizing nanoparticles via single particle inductively coupled plasma mass spectrometry.," *Anal. Chem.*, vol. 83, no. 24, pp. 9361–9, 2011.

[151] D. M. Mitrano, E. K. Lesher, A. Bednar, J. Monserud, C. P. Higgins, and J. F. Ranville, "Detecting nanoparticulate silver using single-particle inductively coupled plasma-mass spectrometry," *Environ. Toxicol. Chem.*, vol. 31, no. 1, pp. 115–121, 2012.

[152] F. Laborda, J. Jiménez-Lamana, E. Bolea, and J. R. Castillo, "Selective identification, characterization and determination of dissolved silver(i) and silver nanoparticles based on single particle detection by inductively coupled plasma mass spectrometry," *J. Anal. At. Spectrom.*, vol. 26, no. 7, p. 1362, 2011.

[153] M. Van Der Zande *et al.*, "Distribution, Elimination, and Toxicity of Silver Nanoparticles and Silver Ions in Rats after 28-Day Oral Exposure," *ACS Nano*, vol. 6, no. 8, pp. 7427–7442, 2012.

[154] S. Makama, R. Peters, A. Undas, and N. W. Van Den Brink, "A novel method for the quantification, characterisation and speciation of silver nanoparticles in earthworms exposed in soil," *Environ. Chem.*, vol. 12, pp. 643–651, 2015.

[155] I.-L. Hsiao *et al.*, "Quantification and visualization of cellular uptake of TiO2 and Ag nanoparticles: comparison of different ICP-MS techniques," *J. Nanobiotechnology*, pp. 1–13, 2016.

[156] Y. Dan, H. Shi, C. Stephan, and X. Liang, "Rapid analysis of titanium dioxide nanoparticles in sunscreens using single particle inductively coupled plasma-mass spectrometry," *Microchem. J.*, vol. 122, pp. 119–126, 2015.

[157] A. P. Gondikas, F. Von Der Kammer, R. B. Reed, S. Wagner, J. F. Ranville, and T. Hofmann, "Release of TiO2 Nanoparticles from Sunscreens into Surface Waters: A One-Year Survey at the Old Danube Recreational Lake.," *Environ. Sci. Technol.*, vol. 48, no. 10, pp. 5415–22, 2014.

[158] I. Kálomista, A. Kéri, and G. Galbács, "On the applicability and performance of the single particle ICP-MS nano-dispersion characterization method in cases complicated by spectral interferences," *J. Anal. At. Spectrom.*, 2016.

[159] M. Hadioui, V. Merdzan, and K. J. Wilkinson, "Detection and Characterization of ZnO Nanoparticles in Surface and Waste Waters Using Single Particle ICPMS," *Environ. Sci. Technol.*, vol. 49, pp. 6141–6148, 2015.

[160] A. Praetorius *et al.*, "Single-particle multi-element fingerprinting (spMEF) using inductively-coupled plasma time-of-flight mass spectrometry (ICP-TOFMS) to identify engineered nanoparticles against the elevated natural background in soils," *Environ. Sci. Nano*, 2017, doi: 10.1039/c6en00455e

[161] C. Degueldre, P.-Y. Favarger, and C. Bitea, "Zirconia colloid analysis by single particle inductively coupled plasma–mass spectrometry," *Anal. Chim. Acta*, vol. 518, no. 1–2, pp. 137–142, 2004.

[162] C. Degueldre and P.-Y. Favarger, "Thorium colloid analysis by single particle inductively coupled plasma-mass spectrometry.," *Talanta*, vol. 62, no. 5, pp. 1051–4, 2004.

[163] M. A. Gomez-Gonzalez, E. Bolea, P. A. O'Day, J. Garcia-Guinea, F. Garrido, and F. Laborda, "Combining single-particle inductively coupled plasma mass spectrometry and X-ray absorption spectroscopy to evaluate the release of colloidal arsenic from environmental samples," *Anal. Bioanal. Chem.*, vol. 408, no. 19, pp. 5125-35, 2016.

[164] J. Navratilova, A. Praetorius, A. Gondikas, W. Fabienke, F. von der Kammer, and T. Hofmann, "Detection of engineered copper nanoparticles in soil using single particle ICP-MS," *Int. J. Environ. Res. Public Health*, vol. 12, pp. 15756–15768, 2015.

[165] J. Tuoriniemi, G. Cornelis, and M. Hassellöv, "Improving the accuracy of single particle ICPMS for measurement of size distributions and number concentrations of nanoparticles by determining analyte partitioning during nebulisation," *J. Anal. At. Spectrom.*, vol. 29, no. 4, p. 743, 2014.

[166] F. Laborda, J. Jiménez-Lamana, E. Bolea, and J. R. Castillo, "Critical considerations for the determination of nanoparticle number concentrations, size and number size distributions by single particle ICP-MS," *J. Anal. At. Spectrom.*, vol. 28, pp. 1220–1232, 2013.

[167] S. Lee, X. Bi, R. B. Reed, J. F. Ranville, P. Herckes, and P. Westerhoff,

"Nanoparticle size detection limits by single particle ICP-MS for 40 elements," *Environ. Sci. Technol.*, vol. 48, pp. 10291–10300, 2014.

[168] F. Laborda, E. Bolea, and J. Jimenez-Lamana, "Single Particle Inductively Coupled Plasma Mass Spectrometry: A Powerful Tool for Nanoanalysis," *Anal. Chem.*, vol. 86, pp. 2270–2278, 2013.

[169] M. Montaño and H. Badiei, "Improvements in the detection and characterization of engineered nanoparticles using spICP-MS with microsecond dwell times," *Environ. Sci. Nano,* vol. 1, no. 4, pp. 338–346, 2014.

[170] O. Borovinskaya, B. Hattendorf, M. Tanner, S. Gschwind, and D. Günther, "A prototype of a new inductively coupled plasma time-of-flight mass spectrometer providing temporally resolved, multi-element detection of short signals generated by single particles and droplets," *J. Anal. At. Spectrom.*, vol. 28, no. 2, pp. 226–233, 2013.

[171] "Single Particle Calculation tool - WUR." [Online]. Available: https://www.wur.nl/en/show/Single-Particle-Calculation-tool.htm. [Accessed: 16-Feb-2017].

[172] "Agilent's comprehensive solutions for the analysis of nanoparticles by ICP-MS." Agilent Technologies, Inc. 2015

[173] S. D. Tanner, V. I. Baranov, and D. R. Bandura, "Reaction cells and collision cells for ICP-MS: A tutorial review," *Spectrochim. Acta - Part B At. Spectrosc.*, vol. 57, no. 9, pp. 1361–1452, 2002.

[174] C. J. Barinaga and D. W. Koppenaal, "Mass Plasma," vol. 8, pp. 71–76, 1994.

[175] I. Feldmann, N. Jakubowski, C. Thomas, and D. Stuewer, "Application of a hexapole collision and reaction cell in ICP-MS Part II: Analytical figures of merit and first applications," *Fresenius. J. Anal. Chem.*, vol. 365, pp. 422–428, 1999.

[176] M. Segura, Y. Madrid, and C. Camara, "Elimination of calcium and argon interferences in iron determination by ICP-MS using desferrioxamine chelating agent immobilized in sol-gel and cold plasma conditions, " *J. Anal. At. Spectrom.*, vol. 18, no. 9, p. 1103, 2003.

[177] S. Lee, X. Bi, R. B. Reed, J. F. Ranville, P. Herckes, and P. Westerhoff, "Nanoparticle size detection limits by single particle ICP-MS for 40 elements," *Environ. Sci. Technol.*, vol. 48, pp. 10291–10300, 2014.

[178] C. Stephan, "ICP - Mass Spectrometry Analysis of Iron Nanoparticles in Organic Solvents Used in the Semiconductor Industry Using Single Particle ICP-MS in Reaction Mode," PerkinElmer, Inc. 2015.

[179] S. Wilbur, M. Yamanaka, and S. Sannac, "Characterization of nanoparticles in aqueous samples by ICP-MS," Agilent Technologies, Inc. 2015.

[180] F. Aureli, M. D'Amato, B. De Berardis, A. Raggi, A. C. Turco, and F. Cubadda, "Investigating agglomeration and dissolution of silica nanoparticles in aqueous suspensions by dynamic reaction cell inductively coupled plasma-mass spectrometry in time resolved mode," *J. Anal. At. Spectrom.*, vol. 27, p. 1540, 2012.

[181] M. Hadioui, C. Peyrot, and K. J. Wilkinson, "Improvements to Single Particle ICPMS by the Online Coupling of Ion Exchange Resins," *Anal. Chem.*, vol. 86, no. 10, pp. 4668–4674, 2014.

[182] B. Nowack *et al.*, "Progress towards the validation of modeled environmental concentrations of engineered nanomaterials by analytical measurements," *Environ.*

Sci. Nano, vol. 2, pp. 421–428, 2015.

[183] K. M. Krueger, A. M. Al-Somali, J. C. Falkner, and V. L. Colvin, "Characterization of nanocrystalline CdSe by size exclusion chromatography.," *Anal. Chem.*, vol. 77, no. 11, pp. 3511–5, 2005.

[184] A. M. Al-Somali, K. M. Krueger, J. C. Falkner, and V. L. Colvin, "Recycling size exclusion chromatography for the analysis and separation of nanocrystalline gold.," *Anal. Chem.*, vol. 76, no. 19, pp. 5903–10, 2004.

[185] S. L. Kerr and B. Sharp, "Nano-particle labelling of nucleic acids for enhanced detection by inductively-coupled plasma mass spectrometry (ICP-MS)," *Chem. Commun.*, no. 43, p. 4537, 2007.

[186] K. Tiede *et al.*, "Application of hydrodynamic chromatography-ICP-MS to investigate the fate of silver nanoparticles in activated sludge," *J. Anal. At. Spectrom.*, vol. 25, no. 7, p. 1149, 2010.

[187] A. R. Poda *et al.*, "Characterization of silver nanoparticles using flow-field flow fractionation interfaced to inductively coupled plasma mass spectrometry," *J. Chromatogr. A*, vol. 1218, pp. 4219–4225, 2011.

[188] K. L. Plathe *et al.*, "Using FlFFF and aTEM to determine trace metal–nanoparticle associations in riverbed sediment," *Environ. Chem.*, vol. 7, no. 1, p. 82, 2010.

[189] B. Schmidt *et al.*, "Quantitative Characterization of Gold Nanoparticles by Field-Flow Fractionation Coupled Online with Light Scattering Detection and Inductively Coupled Plasma Mass Spectrometry," *Anal. Chem.*, vol. 83, no. 7, pp. 2461–2468, 2011.

[190] E. Bolea *et al.*, "Detection and characterization of silver nanoparticles and dissolved species of silver in culture medium and cells by AsFlFFF-UV-Vis-ICPMS: application to nanotoxicity tests.," *Analyst*, vol. 139, pp. 914–22, 2014.

[191] K. Loeschner, C. F. Harrington, J.-L. Kearney, D. J. Langton, and E. H. Larsen, "Feasibility of asymmetric flow field-flow fractionation coupled to ICP-MS for the characterization of wear metal particles and metalloproteins in biofluids from hip replacement patients," *Anal. Bioanal. Chem.*, pp. 4541–4554, 2015.

[192] J. Jiménez-Lamana *et al.*, "An insight into silver nanoparticles bioavailability in rats," *Metallomics*, vol. 6, no. 12, pp. 2242–2249, 2014.

[193] C. Contado and A. Pagnoni, "TiO2 in commercial sunscreen lotion: flow field-flow fractionation and ICP-AES together for size analysis.," *Anal. Chem.*, vol. 80, no. 19, pp. 7594–608, 2008.

[194] V. Nischwitz and H. Goenaga-Infante, "Improved sample preparation and quality control for the characterisation of titanium dioxide nanoparticles in sunscreens using flow field flow fractionation on-line with inductively coupled plasma mass spectrometry," *J. Anal. At. Spectrom.*, vol. 27, no. 7, p. 1084, 2012.

[195] J. Heroult, V. Nischwitz, D. Bartczak, and H. Goenaga-Infante, "The potential of asymmetric flow field-flow fractionation hyphenated to multiple detectors for the quantification and size estimation of silica nanoparticles in a food matrix," *Anal. Bioanal. Chem.*, vol. 406, no. 16, pp. 3919–3927, 2014.

[196] H. Hagendorfer, R. Kaegi, M. Parlinska, B. Sinnet, C. Ludwig, and A. Ulrich, "Characterization of Silver Nanoparticle Products Using Asymmetric Flow Field Flow Fractionation with a Multidetector Approach – a Comparison to Transmission Electron Microscopy and Batch Dynamic Light Scattering," *Anal. Chem.*, vol. 84,

no. 6, pp. 2678–2685, 2012.

[197] D. C. António *et al.*, "Assessing silver nanoparticles behaviour in artificial seawater by mean of AF4 and spICP-MS," *Mar. Environ. Res.*, vol. 111, pp. 162–169, 2015.

[198] S. Wagner *et al.*, "First steps towards a generic sample preparation scheme for inorganic engineered nanoparticles in a complex matrix for detection, characterization, and quantification by asymmetric flow-field flow fractionation coupled to multi-angle light scattering and ICP-MS," *J. Anal. At. Spectrom.*, vol. 0, pp. 1–11, 2015.

[199] A. Navarro-Ortega *et al.*, "Managing the effects of multiple stressors on aquatic ecosystems under water scarcity. The GLOBAQUA project," *Sci. Total Environ.*, vol. 503–504, pp. 3–9, 2015.

[200] J. Vidmar, R. Milačič, V. Golja, S. Novak, and J. Ščančar, "Optimization of the procedure for efficient dispersion of titanium dioxide nanoparticles in aqueous samples," *Anal. Methods*, vol. 8, no. 5, pp. 1194–1201, 2016.

[201] P. Wick *et al.*, "Barrier capacity of human placenta for nanosized materials," *Environ. Health Perspect.*, vol. 118, no. 3, pp. 432–436, 2010.

[202] S. Grafmueller *et al.*, "Transfer studies of polystyrene nanoparticles in the ex vivo human placenta perfusion model: key sources of artifacts," *Sci. Technol. Adv. Mater.*, vol. 16, p. 44602, 2015.

[203] S. Grafmüller, P. Manser, H. F. Krug, P. Wick, and U. von Mandach, "Determination of the transport rate of xenobiotics and nanomaterials across the placenta using the ex vivo human placental perfusion model.," *J. Vis. Exp.*, pp. 1–7, 2013.

[204] J. Ščančar, T. Zuliani, T. Turk, and R. Milačič, "Organotin compounds and selected metals in the marine environment of Northern Adriatic Sea," *Environ. Monit. Assess.*, vol. 127, pp. 271–282, 2007.

[205] I. López-Heras, Y. Madrid, and C. Cámara, "Prospects and difficulties in TiO2 nanoparticles analysis in cosmetic and food products using asymmetrical flow field-flow fractionation hyphenated to inductively coupled plasma mass spectrometry," *Talanta*, vol. 124, pp. 71–78, 2014.

[206] S. H. Behrens and D. G. Grier, "The charge of glass and silica surfaces The charge of glass and silica surfaces," vol. 6716, pp. 6716–6721, 2001.

[207] T. Preočanin, A. Selmani, P. Lindqvist-Reis, F. Heberling, N. Kallay, and J. Lützenkirchen, "Surface charge at Teflon/aqueous solution of potassium chloride interfaces," *Colloids Surfaces A Physicochem. Eng. Asp.*, vol. 412, pp. 120–128, 2012.

[208] V. Golja *et al.*, "Characterisation of food contact non-stick coatings containing TiO $_2$ nanoparticles and study of their possible release into food," *Food Addit. Contam. Part A*, vol. 0, no. 0, pp. 1–13, 2017.

[209] M. H. Nia *et al.*, "Stabilizing and dispersing methods of TiO2 nanoparticles in biological studies," vol. 6, no. 2, 2015.

[210] B. J. R. Thio, D. Zhou, and A. a. Keller, "Influence of natural organic matter on the aggregation and deposition of titanium dioxide nanoparticles," *J. Hazard. Mater.*, vol. 189, no. 1–2, pp. 556–563, 2011.

[211] N. H. Tkachenko, Z. M. Yaremko, and C. Bellmann, "Effect of 1-1-charged ions on aggregative stability and electrical surface properties of aqueous suspensions of

titanium dioxide," *Colloids Surfaces A Physicochem. Eng. Asp.*, vol. 279, pp. 10–19, 2006.

[212] C. Dempsey, I. Lee, K. R. Cowan, and J. Suh, "Coating barium titanate nanoparticles with polyethylenimine improves cellular uptake and allows for coupled imaging and gene delivery," *Colloids Surfaces B Biointerfaces*, vol. 112, pp. 108–112, 2013.

[213] J. Dong *et al.*, "Effect of Triton X-100 on the stability of aqueous dispersions of copper phthalocyanine pigment nanoparticles," *J. Colloid Interface Sci.*, vol. 362, no. 1, pp. 33–41, 2011.

[214] Z. M. Yaremko, N. H. Tkachenko, C. Bellmann, and A. Pich, "Redispergation of TiO2 particles in aqueous solutions," *J. Colloid Interface Sci.*, vol. 296, pp. 565–571, 2006.

[215] A. A. Keller *et al.*, "Stability and Aggregation of Metal Oxide Nanoparticles in Natural Aqueous Matrices," *Environ. Sci. Technol.*, vol. 44, no. 6, pp. 1962–1967, 2010.

[216] C. Tso, C. Zhung, Y. Shih, Y.-M. Tseng, S. Wu, and R. Doong, "Stability of metal oxide nanoparticles in aqueous solutions.," *Water Sci. Technol.*, vol. 61, no. 1, pp. 127–33, 2010.

[217] I. Chowdhury, S. L. Walker, and S. E. Mylon, "Aggregate morphology of nano-TiO 2 : role of primary particle size, solution chemistry, and organic matter," *Environ. Sci. Process. Impacts*, vol. 15, no. 1, pp. 275–282, 2013.

[218] J. D. Hem, "Study and Interpretation of the Chemical Characteristics of Natural Water," Washington, 1970.

[219] J. Vidmar, R. Milačič, and J. Ščančar, "Sizing and simultaneous quantification of nanoscale titanium dioxide and a dissolved titanium form by single particle inductively coupled plasma mass spectrometry," *Microchem. J.*, vol. 132, pp. 391–400, 2017.

[220] Y. Liu, S. A. Majetich, R. D. Tilton, D. S. Sholl, and G. V. Lowry, "TCE Dechlorination Rates, Pathways, and Efficiency of Nanoscale Iron Particles with Different Properties," *Environ. Sci. Technol.*, vol. 39, no. 5, pp 1338–1345, 2005.

[221] K. Peeters, G. Lespes, T. Zuliani, J. Ščančar, and R. Milačič, "The fate of iron nanoparticles in environmental waters treated with nanoscale zero-valent iron, FeONPs and Fe3O4NPs," *Water Res.*, vol. 94, pp. 315–327, 2016.

[222] L. Chekli *et al.*, "Analytical characterisation of nanoscale zero-valent iron: A methodological review," *Anal. Chim. Acta*, vol. 903, pp. 13–35, 2016.

[223] A. Tiraferri, K. L. Chen, R. Sethi, and M. Elimelech, "Reduced aggregation and sedimentation of zero-valent iron nanoparticles in the presence of guar gum," *J. Colloid Interface Sci.*, vol. 324, no. 1–2, pp. 71–79, 2008.

[224] D. Panias, M. Taxiarchou, I. Paspaliaris, and A. Kontopoulos, "Mechanisms of dissolution of iron oxides in aqueous oxalic acid solutions," *Hydrometallurgy*, vol. 42, no. 2, pp. 257–265, 1996.

[225] T. Phenrat, N. Saleh, K. Sirk, R. D. Tilton, and G. V. Lowry, "Aggregation and Sedimentation of Aqueous Nanoscale Zerovalent Iron Dispersions," vol. 41, no. 1, pp. 284–290, 2006.

[226] H. K. Boparai, M. Joseph, and D. M. O'Carroll, "Cadmium (Cd2+) removal by nano zerovalent iron: Surface analysis, effects of solution chemistry and surface

complexation modeling," *Environ. Sci. Pollut. Res.*, vol. 20, pp. 6210–6221, 2013.

[227] H. K. Boparai, M. Joseph, and D. M. O'Carroll, "Kinetics and thermodynamics of cadmium ion removal by adsorption onto nano zerovalent iron particles," *J. Hazard. Mater.*, vol. 186, no. 1, pp. 458–465, 2011.

[228] B. Gilbert, R. K. Ono, K. A. Ching, and C. S. Kim, "The effects of nanoparticle aggregation processes on aggregate structure and metal uptake," *J. Colloid Interface Sci.*, vol. 339, no. 2, pp. 285–295, 2009.

[229] X.-F. Zhang, J.-H. Park, Y.-J. Choi, M.-H. Kang, S. Gurunathan, and J.-H. Kim, "Silver nanoparticles cause complications in pregnant mice.," *Int. J. Nanomedicine*, vol. 10, no. 1, pp. 7057–71, 2015.

[230] E. Söderstjerna, F. Johansson, B. Klefbohm, and U. Englund Johansson, "Gold- and Silver Nanoparticles Affect the Growth Characteristics of Human Embryonic Neural Precursor Cells," *PLoS One*, vol. 8, no. 3, pp. 1–13, 2013.

[231] F. Liu *et al.*, "Effects of silver nanoparticles on human and rat embryonic neural stem cells," *Front. Neurosci.*, vol. 9, pp. 1–9, 2015.

[232] J. Liu, D. A. Sonshine, S. Shervani, and R. H. Hurt, "Controlled Release of Biologically Active Silver from Nanosilver Surfaces," *ACS Nano*, vol. 4, no. 11, pp. 6903–6913, 2010.

[233] M. P. Waalkes, A. M. Poisner, G. W. Wood, and C. D. Klaassen, "Metallothionein-like proteins in human placenta and fetal membranes.," *Toxicol. Appl. Pharmacol.*, vol. 74, no. 2, pp. 179–184, 1984.

[234] N. Hadrup and H. R. Lam, "Oral toxicity of silver ions, silver nanoparticles and colloidal silver - A review," *Regul. Toxicol. Pharmacol.*, vol. 68, no. 1, pp. 1–7, 2014.

[235] Y. Lee *et al.*, "Short communication A Transfer of Silver Nanoparticles from Pregnant Rat to Offspring," vol. 28, no. 3, pp. 139–141, 2012.

[236] K. Loeschner *et al.*, "Distribution of silver in rats following 28 days of repeated oral exposure to silver nanoparticles or silver acetate," *Part. Fibre Toxicol.*, vol. 8, pp. 1–14, 2011.

[237] J. F. Gomes *et al.*, "New insights into the formation mechanism of Ag, Au and AgAu nanoparticles in aqueous alkaline media: alkoxides from alcohols, aldehydes and ketones as universal reducing agents," *Phys. Chem. Chem. Phys.*, vol. 17, no. 33, pp. 21683–21693, 2015.

Bibliography

Publications Related to the Thesis

Journal Articles

Vidmar, J., Milačič, R., Golja, V., Novak, S., & Ščančar, J. (2016). Optimization of the procedure for efficient dispersion of titanium dioxide nanoparticles in aqueous samples. *Analytical methods*, 8(5), 1194-1201, doi: 10.1039/C5AY03305E.

Vidmar, J., Milačič, R., & Ščančar, J. (In press). Sizing and simultaneous quantification of nanoscale titanium dioxide and a dissolved titanium form by single particle inductively coupled plasma mass spectrometry. *Microchemical journal*, doi: 10.1016/j.microc.2017.02.030.

Vidmar, J., Oprčkal, P., Milačič, R., Mladenovič, A., & Ščančar, J. The behaviour of zero-valent iron nanoparticles and their interactions with Cd^{2+} in wastewaters investigated by single particle ICP-MS. *Analytica Chimica Acta,* submitted

Vidmar, J., Loeschner, K., Correia, M., Larsen, E.H., Manser, P., Wichser, A., Boodhia, K., Al-Ahmady, Z.S., Ruiz, J., Astruc, D., & Buerki-Thurnherr, T. Single-particle ICP-MS characterization of silver nanoparticles translocation in the *ex vivo* human placental perfusion model to predict potential fetal exposure. *Particle and Fibre Toxicology,* manuscript prepared.

Vidmar, J., Buerki-Thurnherr, T., & Loeschner, K. Use of alkaline or enzymatic sample pre-treatment prior to characterization of silver nanoparticles in human tissue by single particle ICP-MS. *Analytical and Bioanalytical Chemistry,* manuscript prepared.

Conference Contribution

Vidmar, J., Milačič, R., Ščančar, J. (2014). Določanje nanodelcev TiO2 z metodo "single particle" ICP-MS", In: *Slovenski kemijski dnevi 2014*, Maribor, Zdravko Kravanja, ed., Miloš Bogataj, ed., Zorka Novak-Pintarič, ed., Maribor, Fakulteta za kemijo in kemijsko tehnologijo,

Vidmar, J., Milačič, R., Ščančar, J. (2015). Quantification and sizing of nanoscale titanium dioxide by single particle inductively coupled plasma mass spectrometry, In: *European Winter Conference on Plasma Spectrochemistry 2015*, Münster, Germany.

Vidmar, J. (2015). Sizing and simultaneous quantification of nanoscale titanium dioxide and dissolved titanium form by SP-ICP-MS. In: *Webinar,* 27. October 2015, http://www.chem.agilent.com/edm/2015/07/atomic_eseminars_emea/PublishingImages/TiO2_NPs_Analysis_CR.html.

Vidmar, J., Milačič, R., Ščančar, J. (2015). Single particle ICP - MS: a powerful tool for sizing and quantification of TiO2NPs in environmental water samples, In: Book of abstracts, NANOAPP - 2. International Scientific Conference on Nanomaterials & Applications, Maribor, Slovenia, Aleksandra Lobnik, ed., Andreja Gutmaher, ed.,

Maribor, IOS - Inštitut za okoljevarstvo in senzorje. http://nanoapp.ios.si/wp-content/uploads/2015/06/NANOAPP_2015_Book-of-Abstracts.pdf.

Vidmar, J., Milačič, R., Ščančar, J. (2015). Determination of size distribution of nanosize titanium dioxide and its quantification in the presence of dissolved titanium by single particle inductively coupled plasma mass spectrometry. In: *9th Young researchers' day*, Ljubljana: program and abstract book, Nežka Kavčič, ed., et al, Ljubljana, Institut Jožef Stefan, 2015, str. 8.

Vidmar, J., Milačič, R., Ščančar, J. (2015). Sizing and simultaneous quantification of nanoscale titanium dioxide and dissolved titanium form by SP-ICP-MS. In: Dynamics of Biogeochemical Systems: processes and modeling: conference program and abstracts, Nives Ogrinc, ed., Doris Potočnik, ed., Jadran Faganeli, ed., Ljubljana, National Institute of Biology, Jožef Stefan Institute.

Vidmar, J., Milačič, R., Ščančar, J. (2015). Sizing of nanoscale titanium dioxide and its quantification in the presence of dissolved titanium by single particle inductively coupled plasma mass spectrometry, In: Zbornik: part 2, 7th Jožef Stefan International Postgraduate School Students' Conference, Ljubljana, Andraž Rešetič, ed., et al, Ljubljana.

Vidmar, J., Oprčkal, P., Mladenovič, A., Milačič, R., Ščančar, J. (2016). The fate of zero valent iron nanoparticles after their use in wastewater remediation by single particle ICP-MS, In: Zbornik : 1. del : part 1, Majda Pavlin, ed., et al, Ljubljana, Mednarodna podiplomska šola Jožefa Stefana, 2016, str. 113-121, http://ipssc.mps.si/2016/Proceedings8_IPSSC_2016_Part1.pdf.

Vidmar, J., Loeschner, K., Ščančar, J., Milačič, R. (2016). Studying the degree of AgNPs accumulation in the placental tissue by single particle ICP-MS, In: 10th Young researchers' day, Ljubljana: program and abstract book, Sonja Prpar Mihevc, ed., Mateja Prunk, ed., Jože Pungerčar, ed., Ljubljana, Institut Jožef Stefan.

Other Publications

Journal Articles

Oprčkal, P., Mladenovič, A., Vidmar, J., Mauko Pranjić, A., Milačič, R., & Ščančar, J. (In press). Critical evaluation of the use of different nanoscale zero-valent iron particles for the treatment of effluent water from a small biological wastewater treatment plant. *Chemical Engineering Journal*.

Golja, V., Dražić, G., Lorenzetti, M., Vidmar, J., Ščančar, J., Zalaznik, M., Kalin, M., & Novak, S. (2016) Characterisation of food contact non-stick coatings containing TiO2 nanoparticles and study of their possible release into food. *Food additives & contaminants. Part A., Chemistry, analysis, control, exposure & risk assessment*, 34, 421-433. doi: 10.1080/19440049.2016.1269954.

Vidmar, J., Martinčič, A., Milačič, R., & Ščančar, J. (2015). Speciation of cisplatin in environmental water samples by Hydrophilic interaction liquid chromatography coupled to inductively coupled plasma mass spectrometry. *Talanta*, 138, 1-7, doi: 10.1016/j.talanta.2015.02.008.

Vidmar, J., Zuliani, T., Novak, P., Drinčić, A., Ščančar, J., & Milačič, R. (2016). Elements in water, suspended particulate matter and sediments of the Sava River. *Journal of soils and sediments*, 11, doi: 10.1007/s11368-016-1512-4.

Novak, S., Lorenzetti, M., Drame, A., Vidmar, J., Ščančar, J., & Filipič, M. (2016). Diversity of TiO[sub]2 nanopowders' characteristics relevant to toxicity testing. *Journal of nanoparticle research*, 18, 130-1-130-13, doi: 10.1007/s11051-016-3437-7.

Milačič, R., Zuliani, T., Vidmar, J., & Ščančar, J. (2016). Analytical procedures for speciation of chromium, aluminum, and tin in environmental and biological samples. In: Michalke, B. (ed.). *Metallomics: analytical techniques and speciation methods*, Weinheim: Wiley-VCH, 237-275.

Milačič, R., Zuliani, T., Vidmar, J., & Ščančar, J. (2016). Monolithic chromatography in speciation analysis of metal-containing biomolecules: a review. *Journal of analytical atomic spectrometry*, 31(9), 1766-1779, doi: 10.1039/C6JA00121A.

Martinčič, A., Milačič, R., Vidmar, J., Turel, I., Keppler, B. K., & Ščančar, J. (2014). New method for the speciation of Ru-based chemotherapeutics in human serum by conjoint liquid chromatography on affinity and anion-exchange monolithic disks. *Journal of chromatography. A*, 1371, 168-176, doi: 10.1016/j.chroma.2014.10.054.

Lisjak, D., Plohl, O., Vidmar, J., Majaron, B., & Ponikvar-Svet, M. (2016). Dissolution mechanism of upconverting AYF[sub]4:Yb,Tm (A = Na or K) nanoparticles in aqueous media. *Langmuir*, 32, 8222-8229, doi: 10.1021/acs.langmuir.6b02675.

Kolarević, S., Milačič, R., Zuliani, T., Vidmar, J., et al. (2016). Evaluation of genotoxic pressure along the Sava river. *PloS one*, 11(9), 0162450-1-0162450-23, doi: 10.1371/journal.pone.0162450.

Milošev, I., Levašič, V., Vidmar, J., Kovač, S., & Trebše, R. (2016). pH and metal concentration of synovial fluid of osteoarthritic joints and joints with metal replacements. *Journal of biomedical materials research. Part B, Applied biomaterials*, 9, doi: 10.1002/jbm.b.33793.

Conference Contribution

Vidmar, J., Milačič, R., Ščančar, J. (2015). Determination of cisplatin and its hydrolysed products in environmental waters by hydrophilic interaction liquid chromatography hyphenated to inductively coupled plasma mass spectrometry. In: *EWCPS 2015, European Winter Conference on Plasma Spectrochemistry 2015*, Münster, Germany.

Biography

Education
- 2008: Matura exam
- 2008: enrolled at the Faculty of Chemistry and Chemical Technology, University of Ljubljana, program Chemistry
- 2009 and 2010: received recognition for the best student of the 1st and 2nd year of Chemistry program
- 2013: Graduated at the Faculty of Chemistry and Chemical Technology, University of Ljubljana, program Chemistry
- 2013: Enrolment in Jožef Stefan International Postgraduate School, program Ecotechnology

Studying abroad
- 2012-2013 (4 months): IAESTE internship at Sika technology AG, Zurich, Switzerland at the department Analytics of Construction Chemicals and Mortars
- 2015 (3 months): Performed research for doctoral thesis at the Technical University of Denmark, National food institute under the supervision of Dr. Katrin Loeschner

Employment
- 2012-2013: Internship and student work at the Department of Environmental Sciences, Jožef Stefan Institute
- 2013-2017:Young Researcher at Jožef Stefan Institute, Department of Environmental Sciences

Project work
Research projects:
- Program P1-0143 (Milena Horvat): Cycling of substances in the environment, mass balances, modelling of environmental processes and risk assessment
- LIFE12 ENV/SI/000443: LIFE RusaLCA (Janez Ščančar): Nanoremediation of water from small waste water treatment plants and reuse of water and solid remains for local needs (01/07/2013-31/12/2016)
- L7-6747 (Janez Ščančar): In-situ remediation of polluted soil from contaminated area from Zinkworks Celje
- No. 603629-ENV-2013-6.2.1: 7th FW GLOBAQUA (Radmila Milačič): Managing the effects of multiple stressors on aquatic ecosystems under water scarcity
- NanoSolutions FP7 (Erik Larsen): Developing the nano safety classifier